Transition Metal Impurities in Semiconductors: Induced Magnetism and Band Gap Engineering

A Thesis Submitted to the
College of Graduate Studies and Research
in Partial Fulfillment of the Requirements
for the degree of Doctor of Philosophy
in the Department of Physics and Engineering Physics
University of Saskatchewan
Saskatoon

By
Robert J. Green

Permission to Use

In presenting this thesis in partial fulfilment of the requirements for a Postgraduate degree from the University of Saskatchewan, I agree that the Libraries of this University may make it freely available for inspection. I further agree that permission for copying of this thesis in any manner, in whole or in part, for scholarly purposes may be granted by the professor or professors who supervised my thesis work or, in their absence, by the Head of the Department or the Dean of the College in which my thesis work was done. It is understood that any copying or publication or use of this thesis or parts thereof for financial gain shall not be allowed without my written permission. It is also understood that due recognition shall be given to me and to the University of Saskatchewan in any scholarly use which may be made of any material in my thesis.

Requests for permission to copy or to make other use of material in this thesis in whole or part should be addressed to:

Head of the Department of Physics and Engineering Physics
163 Physics Building
116 Science Place
University of Saskatchewan
Saskatoon, Saskatchewan
Canada
S7N 5E2

Abstract

The main subject of this thesis is the study of electronic and magnetic properties of materials containing $3d$ transition metal atoms. Our motivation stems mainly from the modern fields of spintronic computing and solar energy conversion. The two primary goals of this work are to determine (i) why certain transition metal impurities in certain semiconductors can induce magnetic properties suitable for spintronic computing applications, and (ii) how transition metal impurities can be used to modify the electronic band gaps of semiconductors and insulators in ways useful for harnessing solar energy and for other applications.

To accomplish these goals, we have applied both experimental and theoretical tools. We studied high quality materials prepared by advanced synthesis techniques using x-ray spectroscopy methods at synchrotron light sources. The results of these experiments were interpreted using a variety of theoretical techniques, primarily using computational software developed as part of this thesis and discussed herein.

Regarding the study of introducing transition metal impurities into semiconductors to induce magnetic properties, we first developed and demonstrated a method to determine the location of impurity atoms within the host semiconductor lattice. This allowed to us explain the presence and absence of ferromagnetism in samples prepared under only slightly different synthesis conditions, which helped to address some long–standing issues in the spintronics field. We then studied an advanced and promising material—indium (III) oxide with iron impurities—to determine how magnetic ordering was maintained up to room temperatures. Our techniques unveiled that a portion of the iron atoms were coupled to oxygen vacancies in the material to create conditions which propelled the observed magnetism. This finding confirmed some earlier theoretical predictions by others in the field.

For the study of electronic band gap modifications in semiconductors and insulators via the incorporation of transition metal atoms, we investigated a wide range of materials synthesized using different techniques. Again, we used experimental techniques to determine the location of impurity atoms within the materials, and used this to understand how band gaps were modified upon the introduction of the impurities. For Ti implantation into SiO_2, Ni substitution into ZnO, and a new material, MnNCN, we have determined the electronic band gaps and used our techniques to explain how the values for the gaps arise.

Finally, an additional outcome of this thesis work is a software program capable of simulating x-

ray spectra using various advanced quantum models. We rewrote and built upon powerful existing programs and applied the result to the above studies. Our software was further applied in a collaborative effort with other researchers at the Canadian Light Source to study the differences in two experimental techniques for measuring x-ray absorption: partial and inverse partial fluorescence yields. By using the proper absorption and scattering formalisms to simulate each technique, we were able to explain the differences between the experimental spectra obtained from each. We explain fluorescence yield deviations using an analysis based on the spin configuration of different states, suggesting that the technique can be further extended as a quantitative spin state probe. These results could have significant implications for the field of soft x-ray absorption spectroscopy.

Acknowledgements

Synchrotron-based science and condensed matter physics in general are largely collaborative fields, where the efforts of many individuals are responsible for most developments. Such is the case for the work in this thesis, as contributions from others ranging from experimental to theoretical to motivational have all been pivotal for the accomplishments herein. Below I acknowledge some of these important contributions.

My supervisor, Professor Alex Moewes, has proven to be everything a grad student could need or want in a supervisor. As my initial interests which centered on instrumentation gradually veered first toward experimental materials science, and then took on a strong theoretical condensed matter component, he was a constant source of motivation, allowing me to follow my interests while still helping to direct them down fruitful paths toward useful results. The support he provides his students—whether through academic discussions, financial contributions, exposure to the research community, or career path advice—always seems targeted toward one thing: wanting the best for his students and wanting to see them succeed.

The research projects described in this thesis have resulted in several peer-reviewed publications. In all cases the published manuscripts were the result of the combined efforts of multiple co-authors. I am indebted to these co-authors for their direct contributions to the projects, the fruitful discussions we shared, and their assistance with manuscript preparation. The lists of co-authors can be found at the ends of the various sections in Chapters 5 to 7.

The contributions of fellow students in Professor Moewes' research group are justly encapsulated by a well-known quote from Albert Einstein—*The free, unhampered exchange of ideas* [...] *is necessary for the sound development of science.* Within the research group, a mosaic of different skills and interests has developed during my period of study: some students are skilled in the rigours of quantum theory, others are very talented with experimental equipment; some are adept with band structures and density functional theory, while others focus on local cluster model interpretations of experiment. This blend of attributes has been exceedingly helpful—there has always been someone who would offer an answer to any research related question, and if it was not clear-cut they would always be willing to discuss it to great depths. The exchange of ideas within this group has contributed tremendously to my understanding of condensed matter and consequently to this thesis.

A great deal of my experimental work took place at the SGM beamline at the Canadian Light

Source, where I also served as a beamline assistant for a portion of my Ph. D. studies. Through this great opportunity I learned much about the operation and maintenance of beamlines and had great discussions about maximizing the quality of data and new types of experiments. In this regard I am grateful to the beamline scientist, Dr. Tom Regier, and the rest of the beamline staff.

A significant part of the computational theory and software development in this work was made possible through discussions with some notable experts in the field. Specifically, Dr. Frank de Groot and Dr. Maurits Haverkort were vital to both my understanding of existing calculational codes and the application of advanced computational techniques.

I am very fortunate to have the parents that I do, and almost daily I am reminded of how fortunate I was to be raised in the manner I was and in the environment I was. Somehow they managed to instill in me a strong motivation to succeed and an steadfast desire to determine inner workings of most things I come across. The work I did on the farm growing up might seem far removed from the work I do now, but the character development and work ethic that resulted from the former are undoubtedly crucial to my success at the latter.

Any success I enjoy in life is usually attributable in large part to my wife, Brittney. This thesis is no exception, as she has continually provided motivation whenever needed. She has also been very understanding of the time commitments required for this work, always encouraging me to work whenever I needed to, and never hesitant to support my research trips abroad.

Finally, the funding necessary for completing these studies has come from a variety of sources, and toward each I am very grateful. Direct support for my studies was provided by the Natural Sciences and Engineering Research Council of Canada (NSERC) and the Canada Research Chair program. Further, the research presented here performed at the Canadian Light Source was supported by NSERC, the National Research Council of Canada, the Canadian Institute of Health Research, the Province of Saskatchewan, Western Economic Diversification Canada, and the University of Saskatchewan. The research performed at the Advanced Light Source in Berkeley is supported by the Director, Office of Science, Office of Basic Energy Sciences, of the U. S. Department of Energy under contract number DE-AC02-05CH11231.

Dedicated to my wife Brittney, who is a constant source of support and encouragement.

Contents

List of Tables

List of Figures

List of Abbreviations

AEY	Auger Electron Yield
ALS	Advanced Light Source
BL8	Beamline 8.0.1 (at ALS)
CB	Conduction Band
CI	Configuration Interaction
CLS	Canadian Light Source
CT	Charge Transfer
DFT	Density Functional Theory
DMS	Dilute Magnetic Semiconductor
DOS	Density Of States
EELS	Electron Energy Loss Spectroscopy
EXAFS	Extended X-ray Absorption Fine Structure
FWHM	Full Width at Half Maximum
FY	Fluorescence Yield
HWHM	Half Width at Half Maximum
IPFY	Inverse Partial Fluorescence Yield
JT	Jahn–Teller
LOF	List of Figures
LOT	List of Tables
MBE	Molecular Beam Epitaxy
MCFT	Multiplet Crystal Field Theory
MLFT	Multiplet Ligand Field Theory
NEXAFS	Near Edge X-ray Absorption Fine Structure
NXES	Non-resonant X-ray Emission Spectroscopy
PEY	Partial Electron Yield
PFY	Partial Fluorescence Yield
RIXS	Resonant Inelastic X-ray Scattering
RTFM	Room Temperature Ferromagnetism
SEM	Scanning Electron Microscopy
SGM	Spherical Grating Monochromator (beamline at CLS)
SIAM	Single Impurity Anderson Model
SRIM	Stopping Range of Ions in Matter
TEY	Total Electron Yield
TFY	Total Fluorescence Yield
TSD	Tanabe–Sugano Diagram
VB	Valence Band
XAS	X-ray Absorption Spectroscopy
XEOL	X-ray Excited Optical Luminescence
XES	X-ray Emission Spectroscopy
XPS	X-ray Photoelectron Spectroscopy
XRD	X-ray Diffraction

Chapter 1

Introduction

It has today occurred to me that an amplifier using semiconductors rather than vacuum is in principle possible.

—William Shockley (1939) [1]

Arguably one of the greatest impacts that science has had on society—in any era—has been through the application of semiconductor physics. After the theoretical understanding of energy bands and band gaps was developed in the 1920s and 1930s, the first semiconducting amplifier (or, *transistor*) was developed at Bell Labs in 1947 and set off a technological revolution. Applications involving semiconductors can now be found in devices everywhere,[1] including computers, telephones, solar panels, global positioning systems, etc. It is no surprise, then, that one of the most active areas of materials science research today—and the main theme of this thesis—involves how to develop new and improved materials for use in electronic applications.

As successful as the semiconductor industry has been, and as powerful as computers are today, there is still a persistent motivation for improvement. More difficult computational problems always lay just out of the reach of current technology, in areas ranging from computational condensed matter physics to weather forecasting to transportation scheduling. Of course, computing technology has improved at a more than acceptable rate thus far, with the performance of computers doubling roughly every two years. This exponential trend is popularized as *Moore's Law*, which stems from observation made by Gordon Moore (a co-founder of Intel) in 1965 that improvements in technology had allowed the number of components in integrated circuits to double about every two years for nearly a decade up to that point. Moore then predicted that this trend should continue into the foreseeable future. Remarkably, this trend has continued to hold for over forty years since then, as illustrated in Figure 1.1a, where we show the number of transistors in commercial central processing

[1] An oft-quoted observation regarding the expanse of the semiconductor industry is that there are more transistors produced each year than there are ants in existence [2].

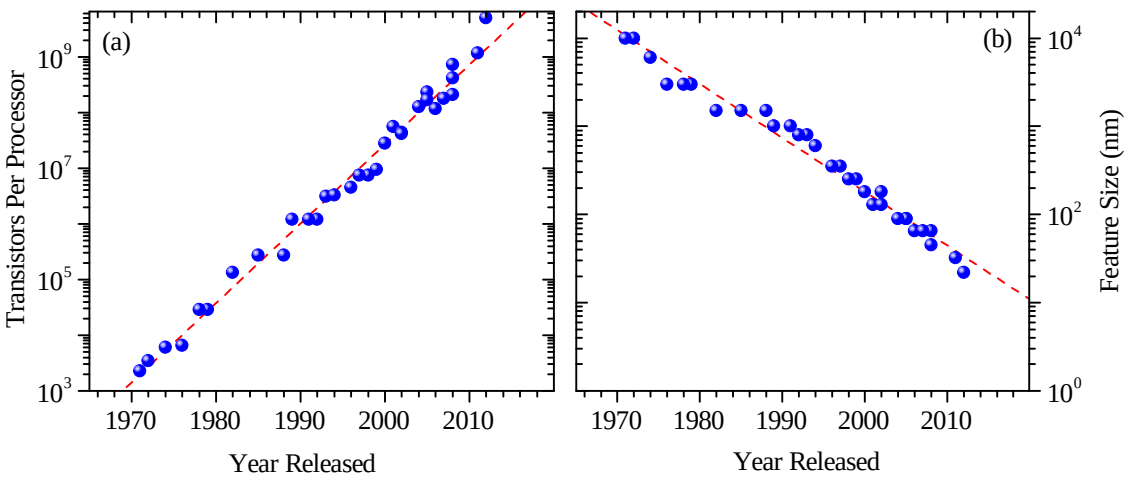

Figure 1.1: Moore's Law trend for semiconductors. (a) The exponential increase in transistors per chip over the past four decades for some common Intel consumer processors [3]. (b) The exponential decrease in feature size (transistor gate length) for the same processors.

units (CPUs) over the past four decades. Indeed, the exponential trend predicted by Moore's Law is evident.

The unwavering and rapid progress exemplified by Moore's Law is an astounding feat with a great impact. But it is somewhat troublesome, then, that the trend described by Moore's Law is heading toward great difficulties and might not last another decade. The reason for this impending cessation of progress is that the conventional approach of improving computers—simply making circuit components smaller so they can be placed at higher densities on chips—obviously has a limit. Simply put, we cannot make transistors smaller than the constituent atoms they are made up of. In Figure 1.1b we show the trend in semiconductor manufacturing process technologies, which correlate closely to the gate lengths of the fabricated transistors. Again we see an exponential trend, but note that the sizes are currently approaching ~10 nm. This is in the range of tens of atoms long, and effects such as quantum mechanical tunnelling make it very difficult to build effective transistors at such small sizes. Thus, a new approach needs to be taken if computing capabilities are to continue their exceptional progress.

1.1 Spintronics and Dilute Magnetic Semiconductors

One possible alternative approach to improving electronics beyond what can be achieved by miniaturization is to incorporate the detection and manipulation of electron spin. This approach has been termed spin electronics, or *spintronics* [4, 5]. Many possible ways of incorporating spin are

being investigated, and many would provide significant performance increases over conventional electronics. Even the simplest of examples where a computer operates much like a typical electronic one, but is built such that each bit has four states (combinations of high/low voltage with up/down spin) would offer an exponential speed-up over the binary machines of today.

One of the most promising avenues for implementing spintronics requires the use of ferromagnetic semiconductors. Such materials could be easily incorporated into current semiconductor electronics approaches, and provide the necessary addition of spin sensitivity through various means. However, ferromagnetic semiconductors are rare, especially those with Curie temperatures at or above room temperature (which is desired for practical applications). Accordingly, enormous amounts of research effort over the past decade have been directed at developing ferromagnetic semiconductors, with mixed results.

The typical approach that has been taken to synthesize a ferromagnetic semiconductor is to modify a conventional semiconductor (ZnO, TiO_2, GaAs, etc.) by introducing a small amount of magnetic transition metal atoms in an effort to induce ferromagnetic properties while retaining the semiconducting behaviour. More details will be given in Chapter 5, but this field has proven to be somewhat controversial. Similar materials prepared by different groups have been reported to have vastly different behaviour (i.e. magnetic vs. non-magnetic), and thus there is still no general consensus on the properties of many materials.

This is where the first of the three main accomplishments of this thesis enters. Our goal was to study several of the promising semiconductors containing transition metal impurities to not only determine their feasibility for spintronics, but to try to answer the questions raised by inconsistencies in earlier studies. To accomplish these goals, we employed a series of synchrotron-based experimental techniques and built software programs to analyze our results. Again, further details are given in Chapter 5, but in short, we were able to use resonant x-ray scattering as an unconventional characterization technique to show extreme sensitivity of the physical impurity positions to the synthesis parameters. We then linked these physical positions to changes in the induced magnetic properties, which helped to explain variability in earlier results. Further, we have studied a very exciting new material within this class—Fe-substituted In_2O_3—and provided a comprehensive explanation of its magnetic behaviour. Our results should be quite beneficial to the spintronics community.

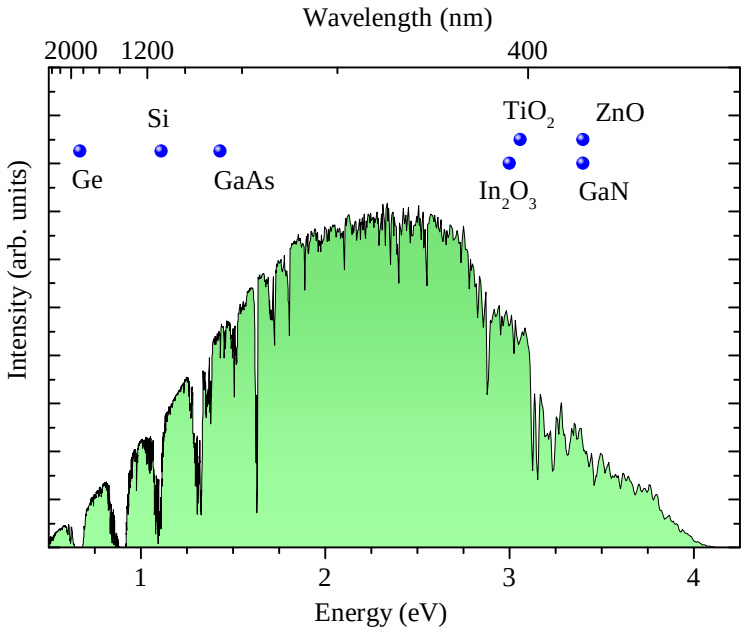

Figure 1.2: The solar spectrum. Also shown for comparison on the same scale are the band gaps of a few relevant semiconductors. Solar data obtained from Ref. [6].

1.2 Band Gap Engineering

The ubiquitous nature of transistors today highlights another issue facing present technology: there is a large demand for energy (to supply to these transistors, as well as meet the rest of our consumption needs) and the majority of energy is currently provided through non-renewable, environmentally destructive means. A great effort is currently being put forward to develop ways to better harness solar energy, either directly through photovoltaic solar cells, or indirectly by using photocatalysts which can produce H_2 as an energy source from water under irradiation from sunlight. Because of the specific shape of the solar spectrum as shown in Figure 1.2, both of these techniques require semiconductors with very specific electronic band gaps for optimal performance. Additionally, other fields of technology—optoelectronics being a prime example—also require materials designed with very specific electronic band gaps.

Designing materials with specific band gaps belongs to the field termed *Band Gap Engineering*. As part of this thesis, we have studied some materials with specific goals of band gap modification. By incorporating titanium into SiO_2 and nickel into ZnO, we have found and explained very useful mechanisms for band gap reduction. Also, by studying transition metal compounds with different anions (nitrogen and carbon rather than oxygen), we have also demonstrated ways of tuning band

gaps. We will discuss these studies, and their potential impact in the field, in Chapter 6.

1.3 Development of New Techniques

Throughout the course of carrying out the aforementioned research, we have developed computational software for performing spectral simulations. Parts of this software will be discussed in Chapter 4. Additionally, an exciting application of this software is a project undertaken in collaboration with researchers at the Canadian Light Source. Using a recently developed experimental technique capable of measuring pure x-ray absorption, we were able to very carefully examine a more commonly used technique called fluorescence yield absorption. By performing simultaneous experiments using the two techniques on aqueous iron complexes, the differences between the two approaches were clearly observed. Further, by employing the calculation software developed for this thesis, we were able to show why the techniques led to different results, and how knowing this fact can allow researchers to extract more information about the electron spin configuration in materials from the experimental techniques. Because these results are again mainly applicable to materials with transition metals, they could be applied in the future to study the spintronic materials discussed above. More details of these results are found in Chapter 7.

1.4 Organization

This thesis can be roughly separated into two parts. First, we lay out the necessary background physics of transition metals (Chapter 2), the experimental techniques used for this work (Chapter 3), and the theory we use to interpret the experiments (Chapter 4). Within this part, much will be derived from the literature, but some portions will be work done as part of this thesis and this will be distinguished when required. Primarily this will involve descriptions of the computational approaches and software we have developed. The second part of the thesis involves our studies on exciting new materials and using exciting new techniques. First, we discuss our results of studying spintronic materials in Chapter 5. Next, in Chapter 6, we present our results on studies of band gap engineering using transition metal impurities. Finally, we present the results we have obtained by studying transition metal complexes with new experimental and theoretical approaches in Chapter 7. The overarching theme will be uncovering the unique properties of materials containing transition metal atoms, and the primary motivation will be the development of new materials for technology applications.

Chapter 2

Transition Metal Properties

In short, an examination of the magnetic properties and colors of the long periods gives us a striking illustration of how a wound in the otherwise symmetrical inner structure of the atom is first created and then healed.

—Niels Bohr [7]

The materials studied to accomplish the goals of this thesis rely on very specific behaviours of transition metals and their compounds. In this chapter we will provide some necessary background information on these behaviours. First, we will define which elements we precisely mean when we discuss transition metals. Next we will describe the physics behind some important properties of both isolated transition metal atoms, and transition metal atoms in solids.

Serious attempts at arranging the elements into different groups which behave similarly began in the late 18^{th} and early 19^{th} centuries with scientists such as Antoine-Laurent de Lavoisier and Johann Wolfgang Dobereiner. After a large number of elements were recognized over the course of the 19^{th} century, in 1869 Dmitri Mendeleev arranged the elements in groups similarly to how they are often viewed today [8]. Figure 2.1a shows the common layout to which periodic table has now evolved.

This thesis focuses mainly on the large, central block of the periodic table known as the *d-block*, or transition block. It is these elements that Bohr was referring to in the quote above; indeed their special properties lead to interesting phenomena like magnetism and are responsible for the colours of many materials. More specifically, our studies involve materials containing selected elements from the top row of this block (from scandium to zinc) which are known as the *3d transition metals*. Below we will see that the elements in this row have very interesting characteristics which are of great use in a variety of applications.

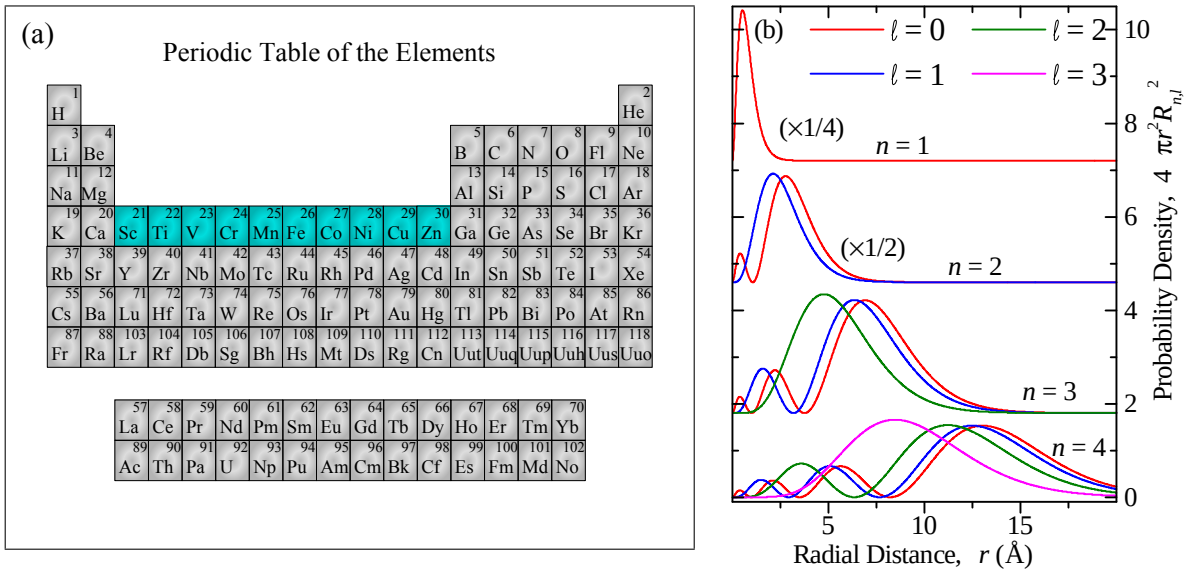

Figure 2.1: Atomic properties of 3*d* transition metals. (a) The periodic table, showing the central 3*d* transition metal series (elements 21 to 30) in light blue. (b) Radial electron wavefunction probability densities for the first few levels of the hydrogen atom.

2.1 Radial Wavefunctions and Localized 3*d* Electrons

The 3*d* transition metals are so named because the 3*d* electron shell is typically the open (unfilled) valence shell of these atoms when they are isolated or in materials.[1] For example, in manganese monoxide (MnO), the Mn atoms have a valence configuration $3d^5$, meaning the 3*d* shell is half full (note that the two 4*s* electrons present in isolated Mn are formally given up to the oxygen atoms). The origin of many interesting phenomena observed in transition metal compounds is this unfilled 3*d* shell and the radial wavefunctions of electrons in this shell.

Recall that quantum mechanics explains the presence of different electron shells and orbitals like the 3*d* orbitals of interest here. The typical solution of the Schrödinger equation for a hydrogen-like atom (the only case where analytic solutions are available) leads to electron wavefunctions which are separated into an angular part and a radial part. The behaviours of these wavefunctions are governed by the quantum numbers which arise as part of the solution. In particular, the shapes of the radial wavefunctions are governed by both the principal (n) and azimuthal (ℓ) quantum numbers.

In Figure 2.1b we plot the square of the radial electronic wavefunctions for several energy levels

[1] Note that this definition leaves out zinc which has a full 3*d* shell in all known compounds. For this reason zinc behaves quite unlike the rest of the 3*d* block and the following discussion does not strictly apply to it, though it is formally defined as a transition metal by the International Union of Pure and Applied Chemistry.

of a hydrogen atom. The full details for obtaining these functions from the Schrödinger equation can be found elsewhere [9, 10], but for brevity we will only point out a few key observations here. First, note the presence of *nodes* in the radial wavefunctions for many cases. The number of radial nodes (apart from the trivial node at $r = 0$) is given by $n - \ell - 1$, where $\ell = 0, 1, 2, ...$ correspond to the s, p, d,... designations typically used. Here we observe the first important feature of the $3d$ electron shell: the radial wavefunctions do not have nodes (n is 3 and ℓ is 2, so $n - \ell - 1 = 0$). The physical consequence of this lack of radial nodes is that it allows $3d$ electrons to remain tighter to the atomic nucleus. In other words, this feature encourages a localization of the $3d$ electrons. Note that we have plotted wavefunctions for a hydrogen atom, but this concept remains valid for many-electron atoms as well, where the analytical solutions are not available.

A second key feature of $3d$ transition metals can be observed by plotting several of the outermost electron wavefunctions together, as shown in Figure 2.2a for an isolated Ni atom.[2] Here we see that while the $3d$ shell is the filling valence shell, it is much more contracted than the $4s$ shell, which helps to explain why $4s$ electrons are usually lost first upon oxidation. Additionally, we see that the extrema of the $3s$ and $3p$ wavefunctions extend about as far out radially as that of the $3d$, which is denoted by the dotted vertical line in the Figure. While these *core* electron shells have a higher binding energy and thus are strongly energetically bound to the nucleus, their extended presence can act to repel the valence electrons of neighbouring atoms (e.g., oxygen $2p$ electrons in monoxides), thus weakening the bonding between the valence $3d$ electrons and neighbouring atoms [11]. Again, this result encourages a localization of the $3d$ electrons.

The angular parts of the $3d$ electron wavefunctions are shown in Figure 2.2b. There are 5 orbitals, which, by the Pauli exclusion principle, can each accommodate a spin up and spin down electron, accounting for the 10 possible $3d$ electrons. Note that the lower two orbitals in the Figure have lobes which are directed along the Cartesian (x, y, z) axes whereas the lobes for the upper three are directed in between the axes. This observation will become important as we begin to discuss crystal field and bonding effects in solids, mainly in Chapter 4.

[2] As mentioned, analytical solutions are not available in this case. Here we use Cowan's code [9], which calculates the wavefunctions numerically.

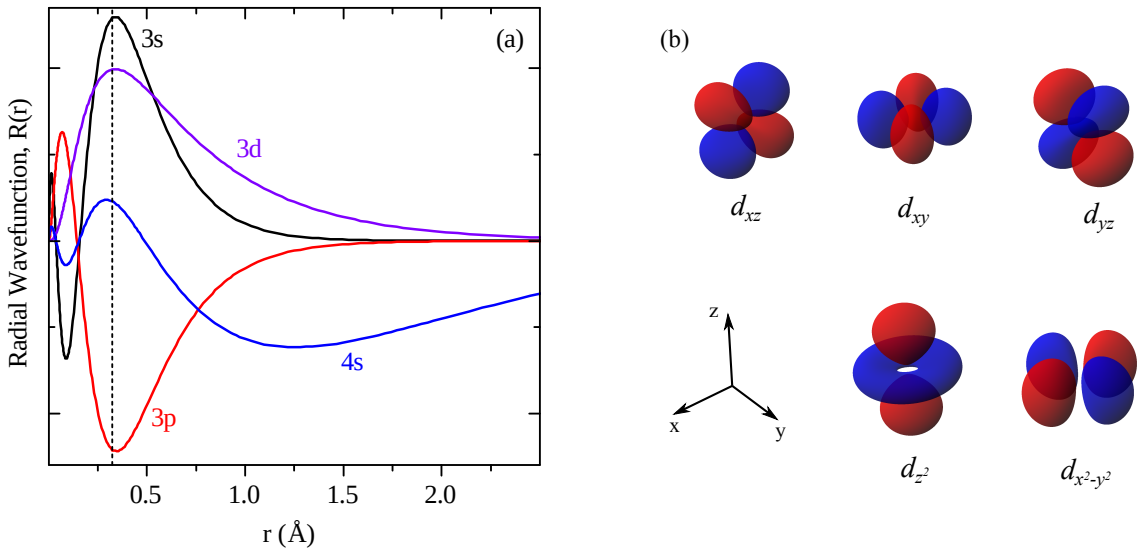

Figure 2.2: Radial and angular wavefunctions. (a) Some of the radial wavefunctions of a Ni atom. (b) The angular wavefunctions of the 3*d* orbitals.

2.2 Electron Correlation and Multiplet Physics

The observations made above regarding radial wavefunctions all point toward one common result: 3*d* electrons tend to remain localized near atoms, and accordingly participate relatively weakly in chemical bonding. There is a very interesting consequence of this behaviour: being localized near the atom means that the different 3*d* electrons strongly interact with each other, leading to what is called *electron correlation*. Individual Coulomb and exchange interactions between each pair of localized electrons cause a collective behaviour to emerge. When one of these electrons is perturbed, the electron correlation means all of the others are affected as well.

In reality, the 3*d* electrons in a solid are not as localized as in an isolated atom. By the very definition of a solid, there will obviously always be some interaction with neighbouring atoms. However, a good starting point for understanding the properties of a correlated transition metal compound is indeed atomic physics. Thus, we will begin with an atomic-like picture before explaining what is different in real materials.

For an isolated transition metal atom with a partially filled 3*d* shell, the correlation effects lead to a multitude of non-degenerate eigenstates. If we consider an atom with n electrons in the 3*d*

shell (and all lower shells filled), we see that there are

$$\binom{10}{n} = \frac{10!}{(10-n)!n!} \tag{2.1}$$

different ways to arrange the n electrons within the orbitals. Thus, for an isolated atom (and only considering the arrangements of the $3d$ electrons), there are this many different eigenstates, although many can be degenerate.

In Figure 2.3 we plot these eigenstates, or *multiplets*, calculated using Cowan's atomic Hartree Fock program [9] for isolated atoms with +2 oxidation states (i.e., $3d^n4s^0$ configurations) ranging from Sc to Cu. Indeed, we see that the number of states grows from $3d^1$ up to $3d^5$, before decreasing again up to $3d^9$. Note that the horizontal widths of the lines corresponds to the number of degenerate states at a particular energy level. If the spherical atomic symmetry were broken, by crystal field effects in a solid for example, then some of these degeneracies would be lifted and a greater number of separate energy levels would be present.

From Figure 2.3, we see that the number of multiplets and their energies are very sensitive to the number of d electrons. In Chapter 3, we will see that they are also very sensitive to the local environment of the atom in a solid and to the atomic number. Thus, probing these states can provide a wealth of information about the material. This can be accomplished with a variety of techniques, including optical absorption, electron spin resonance, x-ray absorption, x-ray scattering, and many others.[3] For rare earth solids, where all of the previous discussion applies to the valence $4f$ electrons, one actually finds that this atomic picture describes the energy levels in solids very well. Experimental measurements of these multiplet eigenstates have been reproduced very successfully using purely atomic calculations [12,13]. This is due to the fact that $4f$ electrons show even stronger localization than $3d$ electrons and are thus perturbed very little by symmetry effects in a solid. However, for transition metal compounds, we find that the atomic point of view is not adequate, and we must consider more details about the bonding in the solid to get a good understanding of the multiplet energies. This is actually advantageous, because it means we can learn about the material properties, and the interactions between the transition metal and other atoms in the lattice, by studying the multiplets. Below we will discuss these interactions with the rest of the solid.

[3] Note that some of these techniques probe excited-state multiplets (e.g. core-hole perturbed states in XAS), but similar information is gained nonetheless.

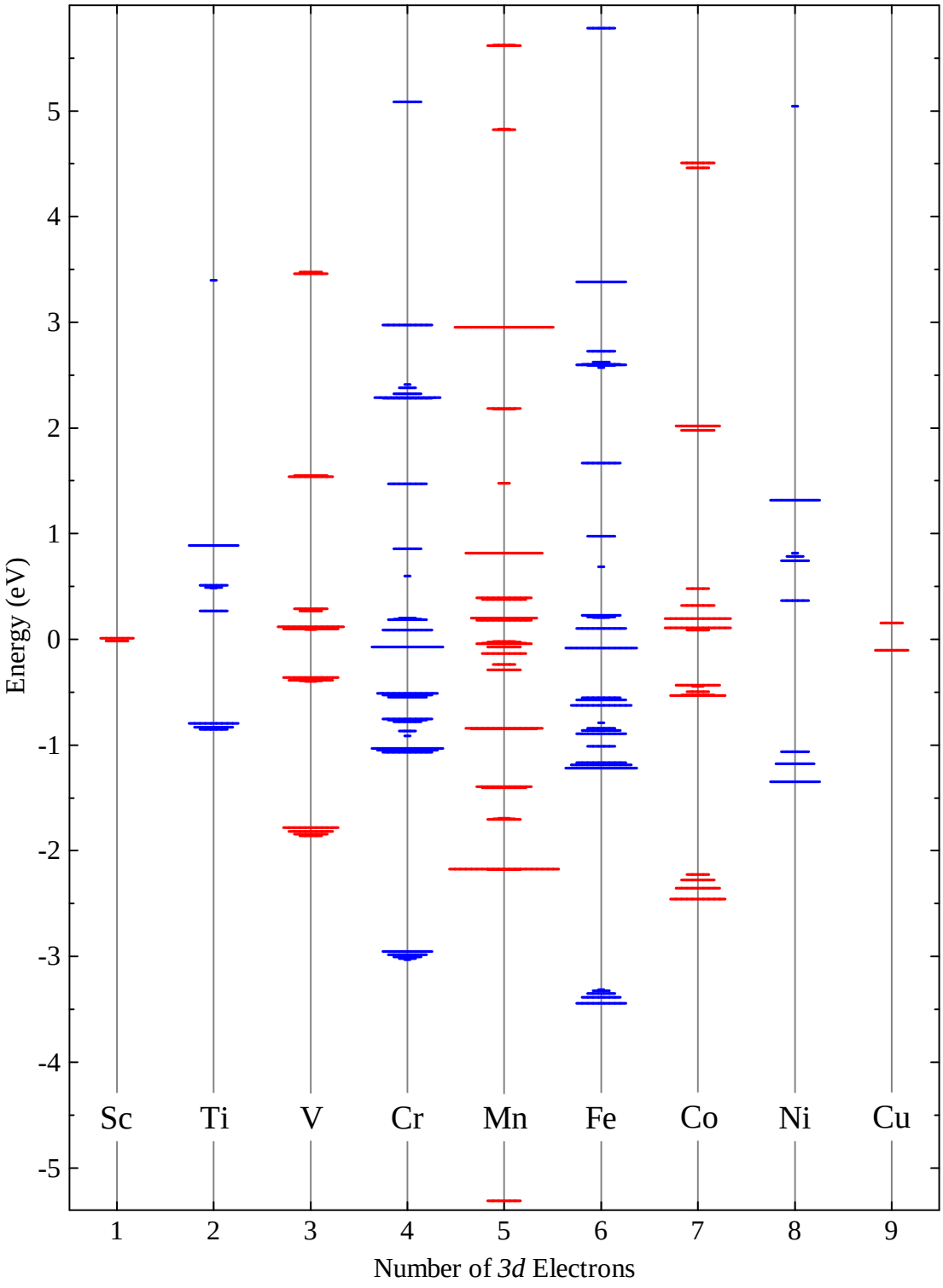

Figure 2.3: Calculated energies of atomic multiplets across the 3*d* series. The horizontal width of the bars corresponds to the number of degenerate states. The calculations were performed using Cowan's atomic Hartree Fock program and include spin-orbit coupling.

2.3 Electronic Structure and Band Gaps

Many transition metal oxides and related compounds are insulators, and this insulating nature proved difficult to explain in the early days of band theory. While it was recognized in 1937 that band theory could not account for this insulating behaviour [14, 15], it was actually in 1949 that Mott developed a general explanation for this issue [16]. The essence of Mott's approach was to consider more closely the energy costs of transporting an electron through a lattice. If the hopping of an electron from one site to another costs energy due to Coulomb repulsion, the transport requires higher energy input and the material will be insulating. For example, in a material that has transition metals with n formal $3d$ electrons, the energy cost of moving an electron from one metal site to another is given by

$$U = E\left(d^{n-1}\right) + E\left(d^{n+1}\right) - 2E\left(d^{n}\right) \tag{2.2}$$

where E denotes the energy of the configuration and U is often around 5 – 10 eV in correlated transition metal compounds.

These Coulomb repulsion concepts were expanded on by both Mott [17,18] and Hubbard [19,20] over the next two decades, and in the 1980s, one more crucial development took place. While the Mott-Hubbard approach considered the energy costs of hopping between metal sites in a lattice, Zaanen, Sawatzky, and Allen (ZSA) showed that for a great deal of materials it is also important to consider the charge transfer energies associated with ligand electrons hopping to metal sites. Similar to the definition of U above, we can define the charge transfer energy associated with ligand to metal hopping as

$$\Delta = E\left(d^{n+1}\underline{L}\right) - E\left(d^{n}\right) \tag{2.3}$$

where $\underline{L}$ denotes a hole in the anion (ligand) valence band. The lower of the energies for these two phenomena—the Mott-Hubbard U gained when an electron hops between metals sites and the charge transfer Δ gained when an electron hops from a ligand band to a metal site—determines which fluctuation defines the band gap of the material.

These ideas are illustrated in Figure 2.4 from a schematic density of states (DOS) point of view. For materials such as transition metal oxides, the DOS near the Fermi level consists primarily of metal $3d$ states and ligand (e.g., oxygen) $2p$ states. Recalling that the ligand $2p$ band is generally full, there is a strong presence of these $2p$ states in the valence band (VB) region. The metal $3d$

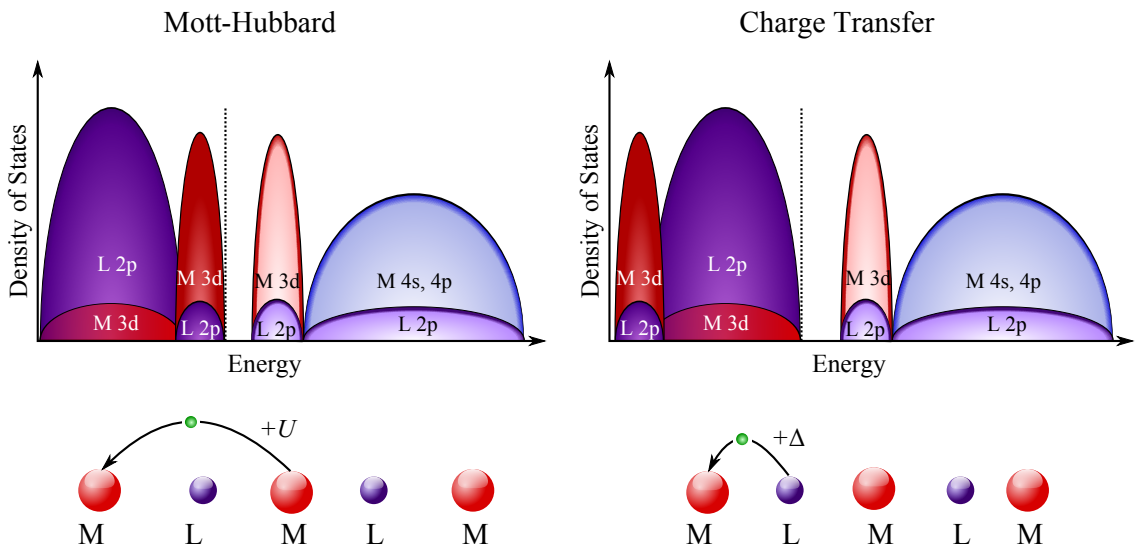

Figure 2.4: Mott-Hubbard (MH) and charge transfer (CT) band gaps. For MH gaps, the charge fluctuations are between metal sites and the energy cost is U. For CT gaps, the charge fluctuations are from ligand to metal sites, and the energy cost is Δ. The approximate Fermi level is denoted by the dashed line. This figure is an elaborated version of one from Ref. [21] using concepts discussed in Ref. [22].

band will generally be partially full, meaning there are significant contributions to both the VB occupied states and the conduction band (CB) unoccupied states. These full and empty $3d$ bands are pushed apart by the Mott-Hubbard U effect described above.

Within the solid the two types of atoms (metal and ligand) bond together, meaning the individual characters of the states will mix somewhat through hybridization. This is shown in the Figure, where we always have a weaker band coincident with a stronger band. The stronger portion represents the states that the band is primarily derived from (i.e. they would be roughly there without hybridization), while the weaker band shows the other character that is mixed in because of the hybridization.

For the case of a Mott-Hubbard insulator, shown in the left of Figure 2.4, the top of the VB is composed primarily of $3d$ states, with some ligand $2p$ character mixed in. Since the bottom of the CB is also dominated by $3d$ states (there are formally no empty $2p$ states and the other bands are higher in energy), the band gap is determined by fluctuations between these $3d$ states at the metal sites, as shown in the illustration below the DOS. Here the band gap is therefore related to the size of the Mott-Hubbard U.

For the case of a charge-transfer (CT) insulator, as shown in the right of the Figure, the U is large enough to push the occupied $3d$ states deep in the VB, meaning the top of the VB has

primarily ligand $2p$ character. The bottom of the CB is still $3d$ states, so now the gap is defined by charge fluctuations from the ligand $2p$ states to the metal $3d$ states, as shown in the illustration below the DOS. Thus, for a general correlated transition metal insulator, the magnitude of the band gap is defined by the lesser of the charge transfer Δ or the Mott-Hubbard U. This result was summarized in the ZSA phase diagram in 1985 [23].

There is one more important thing to note from Figure 2.4. We see that regardless of the class of insulator, because of hybridization we always have a certain amount of ligand $2p$ character at the top of the VB and the bottom of the CB. This means that if we can probe these $2p$ states directly, we can determine the magnitude of the band gap via the separation between them. We can in fact probe the VB and CB states using ligand K edge X-ray Emission Spectroscopy (XES), and X-ray Absorption Spectroscopy (XAS), respectively. We will discuss this approach—including potential problems with it—in the following chapter.

2.4 Remarks

This has not been a comprehensive discourse on the properties of transition metals and their compounds. Instead we have only focused on the important details relevant to the scope of this work and the research projects that will be discussed later. Further details on the atomic physics discussed in this chapter can be found in some popular texts [9,24,25]. For more details on the physics of transition metals in solids, the reader is referred to Refs. [15,26–28].

Chapter 3

Experimental Probes of Condensed Matter

> *It doesn't matter how beautiful your theory is, it doesn't matter how smart you are. If it doesn't agree with experiment, it's wrong.*
>
> —Richard Feynman

Much of the great progress made in physics over the past two centuries was driven by experiment. With some notable exceptions,[1] important theoretical revolutions are usually triggered by unexpected or strange experimental observations. Additionally, theoretical predictions are rigorously tested by experiment whenever possible. In keeping with this experimentally-driven approach, most of the work in this thesis is centered around first performing experiments, and then turning to theory for insight based on the experimental findings. To understand why complex, interesting materials behave the way they do, our best approach is usually to physically perturb the material in some way and observe how it reacts. Through this approach we can often deduce the mechanisms by which physical principles drive the interesting properties of the material. For the projects contained in this thesis, the properties we are interested in are related primarily to the electronic structure, and synchrotron radiation is an invaluable tool for experiments in this area.

The discovery of synchrotron radiation in 1947 [29,30], and the subsequent development of dedicated synchrotron storage rings has allowed tremendous advances in condensed matter physics and material science. Being intense sources of photons with energies ranging from the infra-red to those of "hard" x-rays (tens of keV), a vast number of experiments can be performed at synchrotrons. Here we describe a few experimental techniques usually performed at synchrotrons which are particularly applicable to the study of materials containing $3d$ transition metals. Many of the techniques are described in depth elsewhere (references will be given below), so after general introductions we will largely focus only on the important aspects related to the studies contained in this work.

[1] An example of a theory-driven advance in physics is the prediction of antimatter. Dirac's relativistic treatment of quantum mechanics suggested the existence of positrons in 1928, and they were experimentally discovered four years later.

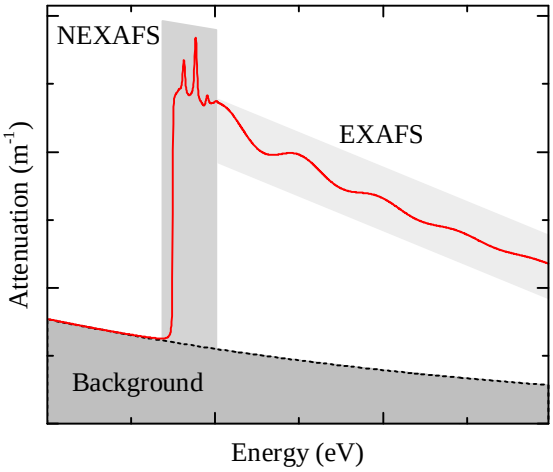

Figure 3.1: A representative XAS spectrum. The three main regions are labelled. The studies in this thesis focus on the NEXAFS region.

3.1 X-Ray Absorption Spectroscopy

X-ray Absorption Spectroscopy (XAS) is one of the oldest and most mature of the techniques to be discussed here. In fact, almost immediately after the discovery of x-rays by Wilhelm Röntgen in 1895, experiments yielded observations of x-ray emission from irradiated materials that was characteristic of the chemical elements contained within those materials [31,32]. Soon, systematic studies of absorption and emission of x-rays were undertaken [32,33], and the discovery and naming of K and L lines was reported in 1911 [32,34]. If we jump forward to 1954, we have the first application of synchrotron radiation using soft x-rays for an absorption measurement [32,35]. Finally, in the 1980s improvements in both instrumentation and theory led to a surge in soft x-ray studies on transition metal L and ligand K edges. For further interesting details of the early history behind XAS, the reader is referred to Ref. [32].

Typical XAS experiments involve scanning the energy of incident photons across a particular absorption edge and monitoring the energy-dependent absorption of the photons. For energies tuned near an absorption edge, numerous processes may take place when a photon is absorbed by a material, depending on how the photon energy relates to the edge. In Figure 3.1, we outline some of these processes using a fictitious absorption edge. Below the edge of interest, the absorption is due to what are typically called background processes; these might include absorption of lower energy edges, (in)elastic scattering, etc. Near and immediately above the threshold the absorption leads to excitation of core electrons into bound states, in the region often called the Near Edge X-ray Absorption Fine Structure (NEXAFS) [36]. Depending on the edge and material studied, these bound states may be dominated by multiplet effects (see Section 3.1.1 below), or they may be

Dipole Selection Rules	
Rigorous	$\Delta J = 0, \pm 1$
	$\Delta M_J = 0, \pm 1$
	$\pi_f = -\pi_i$
LS Coupling	$\Delta L = 0, \pm 1$
	$\Delta S = 0$
	$\Delta \ell = \pm 1$

Table 3.1: Electric dipole transition selection rules. Lowercase (uppercase) symbols refer to single (multiple) electron quantum numbers. The symbol π refers to the parity of the state. Since the selection rules hold strictly only when they involve good quantum numbers, in the presence of appreciable spin-orbit interactions, the J rule should be used rather than those for L and S. Also, when J (L) is zero, we have the additional restriction that ΔJ (ΔL) cannot be zero.

closely representative of a projected component of the unoccupied DOS (see Section 3.1.2). Further above the edge, the core electron is given sufficient energy to reach continuum states, and we see a general exponential decay of the absorption. Superimposed onto this region are oscillations termed Extended X-ray Absorption Fine Structure (EXAFS), which are due to scattering of the excited electron off of neighbouring atoms. For this work, it is the NEXAFS region we are most interested in. The types of excitations observed within this region are quite different for the transition metal L edges versus the ligand K edges that we will study, so we will give a brief introduction into each below.

3.1.1 XAS of Transition Metal $L_{2,3}$ Edges

In $L_{2,3}$ XAS, $2p$ core electrons are excited into unoccupied orbitals. By dipole selection rules (see Table 3.1; dipole rules apply because soft x-rays have relatively long wavelengths compared to orbital radii), we have $\Delta \ell = \pm 1$, so the p electrons have to be excited into s or d orbitals.[2] In practice it is found that the excitations into the $3d$ orbitals dominate the spectra [37], so we only need to consider the $2p \rightarrow 3d$ excitations to understand the majority of spectra.[3]

Recall that one of the main points stressed in the previous chapter is that the $3d$ electrons of

[2] For the rigorous rules, this $p \rightarrow s, d$ result is enforced by the parity selection rule.

[3] Actually, step-like edges are sometimes visible in our spectra which are due to excitations into delocalized conduction band states, but these are weak and relatively featureless, and thus do not affect our analysis of $2p \rightarrow 3d$ excitations.

transition metal atoms tend to remain somewhat localized in many compounds. This localization has great implications for the type of information that can be obtained from XAS. Because of the localization, there is a strong overlap of the $2p$ core wavefunction containing an unpaired electron and the $3d$ valence wavefunction. This strong overlap, combined with the strong Coulomb and exchange interactions between the $3d$ electrons themselves, leads to the spectra being dominated by multiplet effects [38].

An invaluable consequence of a spectrum dominated by multiplet effects is that the general shape of such a spectrum depends strongly on the d electron count. We show this in Figure 3.2a, where we plot simulated XAS spectra[4] for elements ranging from Ca with no ground state d electrons, up to Cu with a $3d^9$ initial state configuration. The spectra here are plotted with configuration-averaged energies centered at 0 eV for easy comparison (i.e. the binding energies of different elements are not taken into account). Indeed, we see drastically different spectral shapes for the different numbers of d electrons. We can confirm that this is truly a consequence of the number of d electrons and not the change in atomic number by considering the spectra in panel (b) of the Figure. Here we plot simulated spectra for Mn, Fe, and Co, but with varying oxidation states so that the number of electrons remains constant. As expected, the general shapes of the spectra are very similar. We only see a spreading out of the multiplet features as we increase the atomic number, due to the stronger repulsion effects induced by the stronger nuclear charge.

Figure 3.2c demonstrates yet another key feature of $L_{2,3}$ XAS. Here we show the large changes in XAS spectra induced by changes in the local environment around the transition metal site. In particular, we plot Co^{2+} spectra for an isolated atom as well as an atom located in octahedral and tetrahedral crystal fields. The different fields lead to different energy levels of the various multiplets, yielding spectra with markedly different shapes. Thus, we can often deduce the coordination of an atom from the XAS alone. Further details regarding crystal fields and more advanced bonding considerations are given in Chapter 4.

Returning to 3.2b, we see another important feature of XAS. The two edges—the L_3 edge below about 5 eV and the L_2 edge above that point—move farther apart as the atomic number increases. This is also evident in panel (a) of the Figure. This splitting between the L_3 and L_2 edges is caused by the $2p$ spin-orbit interaction, which gets stronger for later transition elements because it relates directly to the nuclear charge and inversely to the orbital radii [9]. In Figure 3.3, we show the

[4]Here we use the crystal field model (see Chapter 4) with an O_h field of strength 1.0 eV, to end up with spectra resembling those that one would find in oxides.

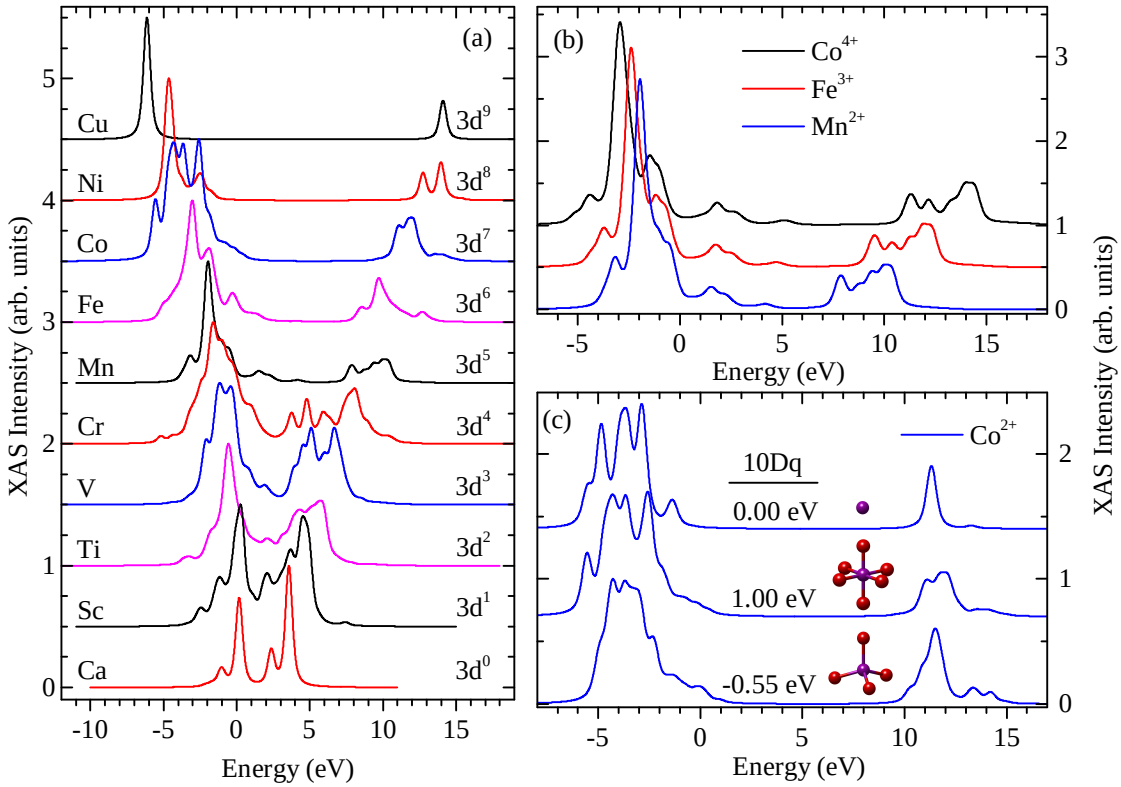

Figure 3.2: Key features of $L_{2,3}$ X-ray Absorption Spectroscopy, demonstrated using crystal field multiplet calculations. (a) Spectral shapes for divalent, octahedrally-coordinated atoms depend strongly on d electron count. (b) Effects of spin-orbit coupling, which gets stronger as Z increases. (c) The spectral shapes are very sensitive to crystal fields imposed by neighbouring ligands. The empirical crystal field splitting parameter is given for each curve. For all calculations shown in this figure, spin orbit coupling has been included, the empirical crystal field parameter $10Dq = 1.0$ eV unless otherwise given, and intra-atomic Slater integrals are scaled to 80% of Hartree-Fock values. See Chapter 4 for a description of the crystal field model.

individual binding energies of the two edges for the $3d$ transition metal series [30]. We see that the binding energy increases as the nuclear charge increases, which leads to very different edge energies for different elements. Additionally, the difference between the binding energies for the two edges does indeed increase going across the series, as indicated by the separation between the lines. This is shown more clearly by the blue curve (plotted against the right vertical axis) where the splitting energy ranges from below 5 eV for Sc up to nearly 20 eV for Cu. This spin-orbit splitting is quite important when interpreting spectral shapes. For the heavier elements of the series, like Ni and Cu, the L_2 and L_3 edges are well separated, so there is not much interference between the two. However, for light elements like Sc or Ti, the edges are very close together and one finds that the relative XAS intensity of the two edges is strongly affected by interference between them [39].

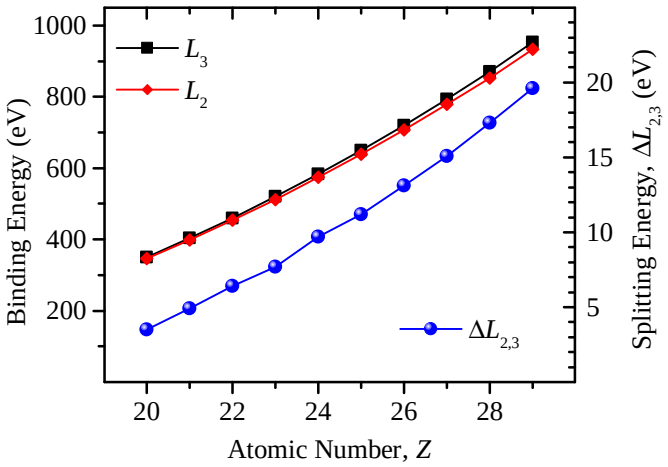

Figure 3.3: L_2 and L_3 edge binding energies. The left vertical axis gives the binding energy, while the right axis gives the spin-orbit splitting between the edges, denoted by the blue curve (circles). The data is from the X-Ray Data Booklet [30].

It is clear from the previous discussion that XAS is a very powerful technique for studying condensed matter. To recap, we have three very important observations that are valuable tools for $L_{2,3}$ XAS:

- The spectral shape is strongly defined by the d electron count.
- The approximate binding energy and $L_{2,3}$ splitting depend strongly on the atomic number.
- The spectral shape depends on crystal fields produced by neighbouring atoms.

From these three observations, we can quickly see some of the very strong points of this type of XAS:

- It is element selective (via the binding energy).
- It is valence selective (via the spectral shape).
- It is sensitive to the local bonding environment of the atom under study (via the spectral shape).

These interpretations of $L_{2,3}$ XAS given above were largely developed in the 1980s. Early Electron Energy Loss Spectra (EELS) highlighted the power of L edge absorption spectroscopy[5] on pure metals [40], and subsequent studies showed $L_{2,3}$ XAS is a powerful electronic structure probe of correlated systems as well [41]. Though XAS measures core-hole excited final states, it

[5]EELS using high energy incident electrons and forward scattering leads to dipole excitation absorption spectra similar to XAS.

was demonstrated that it is indeed sensitive to the ground state electronic structure as well [42], and even the spin configuration of the ground state [43]. In short, a large amount of information can be extracted using $L_{2,3}$ XAS.

3.1.2 XAS of Ligand K Edges

In compounds where transition metals bond with ligands (N, O, F, etc.), much can be learned by studying the XAS of the ligands as well. For these elements, the K edge is of particular interest, and provides information quite different than the transition metal L edges [22]. Here, one observes excitations from the $1s$ core level into states of primarily p character. The fundamental difference from the L edge spectra described above is that here the valence electrons (mainly ligand $2p$) are delocalized and form wide bands. Thus, during the XAS process the strong multiplet coupling is not present and the spectra can be interpreted from a single particle point of view. As a result, our K edge NEXAFS spectra provide a very good approximation of the ligand $2p$ unoccupied DOS.

In Section 2.3, we remarked how hybridization in transition metal compounds means that the states near the bottom of the conduction band have a certain amount of ligand $2p$ character. Thus, since our K edge XAS probes the $2p$ character in the unoccupied states, we can determine the (core-hole shifted) bottom of the conduction band from our spectra. Combining this with K edge emission spectra (see Section 3.3 below), we can determine the bulk band gap of such materials. However, we must be careful to remember that we are not probing exactly the unoccupied DOS. Since we necessarily remove a $1s$ core electron during the XAS process, the states we actually probe are states in the presence of the core-hole. Fortunately, it is found that for many systems, like transition metal oxides, this core hole effect does not alter the DOS strongly and we can still reliably determine the conduction band minimum energy [44]. However, in some cases there are very strong effects that need to be accounted for, as we will show in Section 6.3 where we study transition metal carbodiimides.

The presence of hybridization means that our K edge ligand XAS can also provide information about the unoccupied $3d$ states of the transition metal atoms. We demonstrate this in Figure 3.4, where we show the O K edge XAS of rutile TiO_2. The lower energy region, which we shade in light red for clarity, has previously been identified as composed of states of mixed oxygen $2p$ and titanium $3d$ character [22, 45]. The splitting into two peaks is consistent with the Ti $3d$ states splitting into e_g and t_{2g} bands, and a density functional theory (DFT) calculation of the unoccupied DOS agrees well with experiment [45]. The higher energy region shaded in blue is found to be composed of

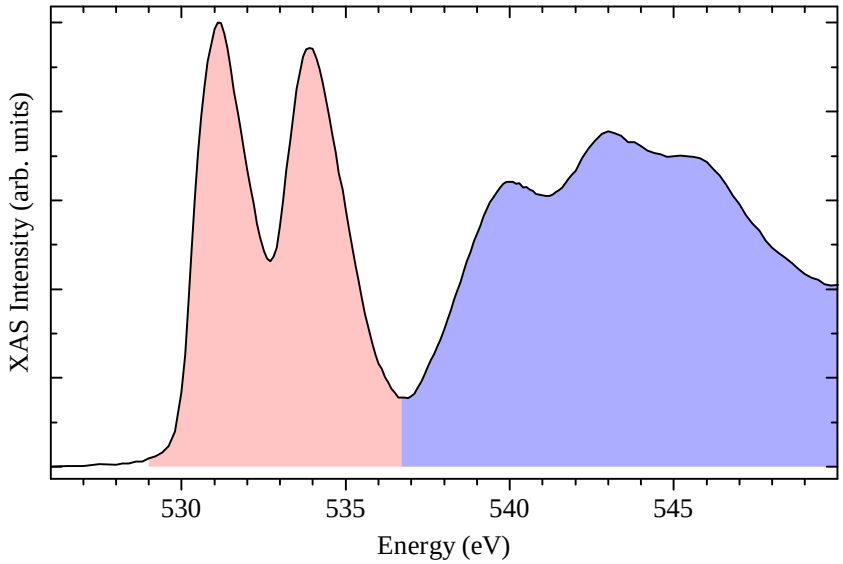

Figure 3.4: Experimental oxygen K edge XAS of rutile TiO_2. The red region is dominated by Ti $3d$ character, split into the characteristic e_g and t_{2g} bands. The blue (higher energy) region is composed of hybridized O $2p$ and Ti $4sp$ states, as well as p character from direct O–O interactions.

oxygen $2p$ states mixed with titanium $4s$ and $4p$ states, as well as antibonding states arising from direct oxygen–oxygen interactions [45].

The designations of states described for this Figure can be compared with the state arrangements laid out in Figure 2.4. Thus, it is clear how K edge XAS provides us with a measurement of the conduction band in many cases. Additionally, we are provided with a measurement of the metal $3d$ unoccupied states, without the strong $2p$–$3d$ multiplet interactions that arise in transition metal $L_{2,3}$ XAS.

3.1.3 Detection Techniques

In principle, it is very simple to measure how strongly a sample absorbs x-rays. All one needs is a source and detector. By placing the sample between these two devices, the signal on the detector will drop, and the attenuation of the x-rays can be quantified by how much the signal drops. The process, depicted on the left side of Figure 3.5, is described by the Beer-Lambert law, expressed mathematically by

$$I(\omega) = I_0(\omega)\, e^{-\mu(\omega)d} \tag{3.1}$$

where ω is the energy of the x-rays, I is the detected intensity, I_0 is the source intensity, d is the thickness of the sample, and μ is the absorption coefficient (also called the attenuation coefficient)

of the sample. It is μ that we are trying to determine by measuring I and I_0, so we can simply rearrange the equation to get

$$\mu(\omega) = -\frac{1}{d} \ln\left(\frac{I(\omega)}{I_0(\omega)}\right) \tag{3.2}$$

Plotting $\mu(\omega)$ would then display the XAS spectrum in the typical manner, for example as shown above in Figure 3.4.

A significant issue arises with the above transmission technique in many cases. If $\mu(\omega)\, d \gg 1$, then the photons cannot penetrate through the sample and one detects zero signal. Even if the attenuation is not quite large enough to stop the photons for all energies over the spectrum, it can still lead to artificial suppression of strong absorption peaks and, therefore, to incorrect data. We show an example of this in Figure 3.6, where we have measured transmission yield XAS of a 500 nm thick Ti foil. In panel (a) we show the normalized transmission signal (I/I_0), while in panel (b) we show the extracted absorption coefficient. We compare this to an XAS spectrum of Ti prepared in-situ measured using the total electron yield technique (TEY, see below for a description of the technique) [46]. Indeed, the peaks of the transmission signal are significantly distorted because the foil was too thick for the technique. Here the distortion is clearly visible, but in some cases the saturation is less severe and can go unnoticed, consequently affecting analysis if care is not taken.

In the soft x-ray range (which we are concerned with here), μ is typically on the order of ~100 nm^{-1}, meaning samples only 100 nm thick will already attenuate the incident photon beam by a factor of e. Typically we do not work with free standing samples thinner than micron sizes (and even thin films are usually deposited on thick substrates), so the transmission technique is not possible and we must resort to *yield* techniques.[6]

Yield techniques take advantage of what occurs after an x-ray is absorbed. After a core level XAS event, the system is in a highly excited state which decays very quickly by giving off energy in the form of electrons or photons. In practice it is found that the total number of electrons given off by a sample varies quite consistently with the number of core holes created. Thus, simply by detecting these *Auger* electrons as the incident x-ray energy is scanned, one can obtain an XAS spectrum. Note that it is possible to detect these electrons directly as they are emitted from the sample surface, but it is often more convenient to simply measure the magnitude of the positive current draining from the sample to an electrical ground as the electrons are replenished. In either

[6] Even in the case of free standing films which are thin enough for transmission XAS, other issues like thickness variations or pin-holes can also distort the spectra and need to be considered.

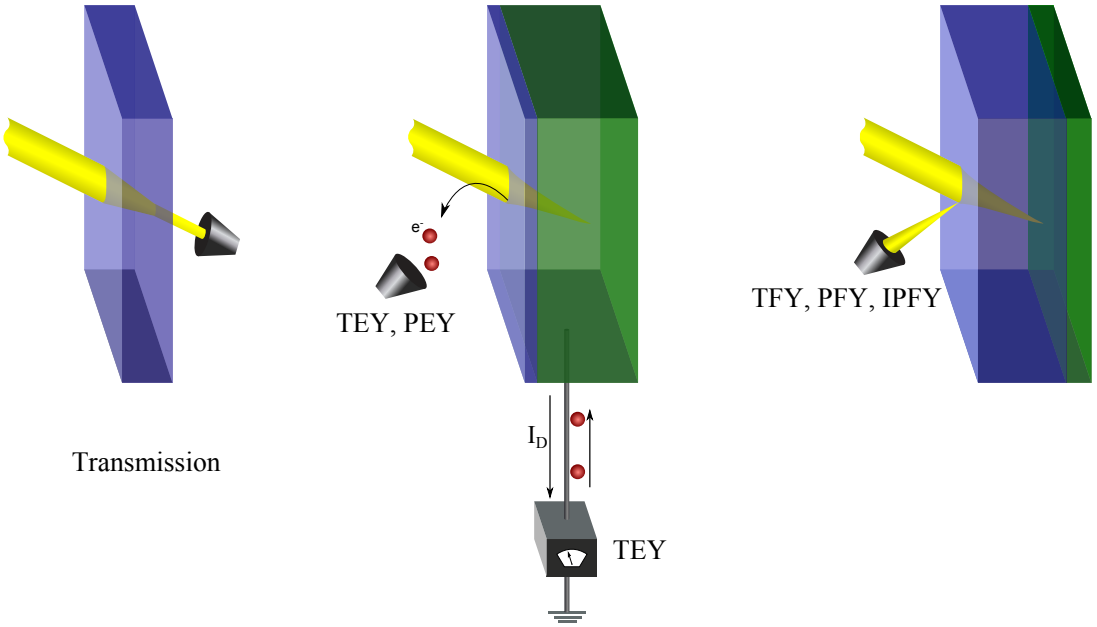

Figure 3.5: Some common techniques for XAS detection. On the left, transmission detection is depicted, where the absorption is measured by detecting the fraction of photons that pass through the sample. Electron yields are shown in the center, where either surface-emitted electrons are detected or a replenishing current of electrons is detected. On the right, fluorescence yields are depicted, where emitted photons are detected as an indirect way of measuring the absorption of incident photons. For all figures, the blue regions qualitatively represent the probing depths of the techniques.

case, when electrons of all energies are detected without discrimination, this technique is known as *Total Electron Yield*, or TEY. For the detection of the emitted electrons, one can also use an energy selective detector to only count electrons of certain energies. This technique is then called *Partial Electron Yield* (PEY), or alternatively *Auger Electron Yield* (AEY). For all electron yield techniques, the probing depth is quite small (several nm [54]) because the mean free paths for electrons are quite short. One can achieve some variations in probing depth by using partial yields of various energy ranges, but the depths will nonetheless remain quite small. Electron yield techniques are illustrated in the center of Figure 3.5.

When the excited XAS states decay it is also possible for photons to be given off, and one can detect these photons as a way to measure XAS. If all photons given off are detected, the technique is called *Total Fluorescence Yield* (TFY), whereas if only a certain energy range of photons are detected, it is called *Partial Fluorescence Yield* (PFY). Again, in practice it is found that often these signals are good approximations to absorption, and an advantage of this technique is that

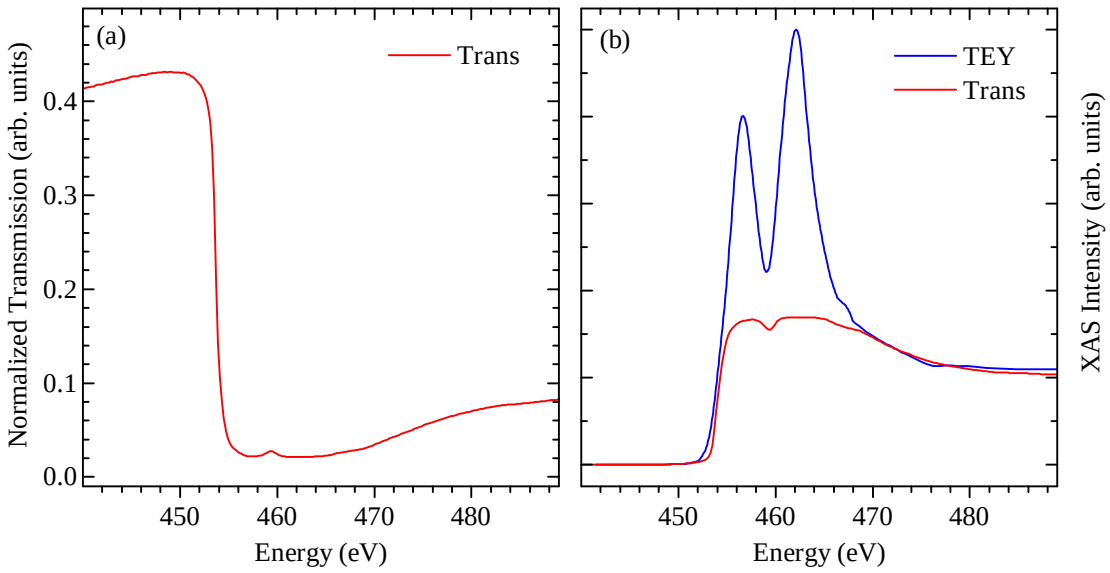

Figure 3.6: Transmission XAS saturation for a Ti foil. (a) The normalized transmission signal. (b) The extracted absorption spectrum, compared to a spectrum obtained using total electron yield (TEY) detection with minimal saturation. TEY spectrum of in-situ prepared Ti generously provided by T. Mazza *et al.* [46].

photon penetration depths are of the order of ~100 nm for soft x-rays, leading to probing depths larger than for electron yields and thus reduced surface sensitivity. However, PFY and TFY are very susceptible to certain types of distortions. Because these distortions are important to the research presented in Chapter 7, and because an understanding of resonant scattering (presented in the next section below) is important to understand some of these distortions, we have dedicated Section 3.4 to an introduction of the issues of fluorescence yield XAS.

Very recently, a new yield technique has been developed as a result of work done at the Canadian Light Source. Termed *Inverse Partial Fluorescence Yield*, or IPFY, this technique also measures fluorescence photons, but here the specific photons from a non-resonant, lower energy edge are detected. As the resonant edge begins to absorb more incident photons, the non-resonant background fluorescence decreases, and one can detect an inverted XAS spectrum [47, 48]. One essentially uses secondary atoms as a set of x-ray transmission detectors dispersed throughout the sample, and after inverting the signal, the spectrum is directly proportional to the true XAS shape. IPFY is not always applicable since it relies on having a lower energy edge available, but when it can be used it provides the most reliable spectra out of all the yield techniques. Some of our data in Chapter 6 are IPFY spectra and in Chapter 7 we discuss some of our work studying this new technique.

3.2 Resonant Inelastic X-Ray Scattering

Resonant Inelastic X-Ray Scattering, or *RIXS* [49, 50], is a technique which is closely linked to XAS. Like XAS, for RIXS experiments one uses monochromatic x-rays to resonantly excite core electrons into unoccupied states, but now we detect—in an energy resolved manner—the inelastically scattered x-rays given off after a subsequent decay in the material. For example, $L_{2,3}$ RIXS involves the excitation of a $2p$ core electron into a $3d$ orbital, followed immediately by the decay of a $3d$ electron (possibly the same one) to fill the $2p$ hole. The system may be left in an excited state after the scattering event, leading to a lower energy emitted photon than incident photon.

The RIXS process is a coherent, single step process, meaning the electronic system is scattered from an initial (usually ground) state to a final state, through a set of resonantly enhanced, virtual intermediate states. A loose analogy can be drawn to the double-slit experiment, illustrated in Figure 3.7a. Recall that here the light intensity measured at the detector must be calculated by summing the probability *amplitudes* of light passing through either of the slits to reach the detector.[7] Because the amplitudes of either path are complex (i.e. they have a phase factor), the detected intensity is not necessarily equal to the sum of intensities that would be found by performing the experiment with one slit open at a time. The coherent sum of the amplitudes can lead to constructive and destructive interference.

In Figure 3.7b, we show a schematic of the RIXS process to compare with that of the double-slit experiment. Here, each final state can be reached from the initial (ground) state by scattering through many possible intermediate states. These intermediate states can be compared to the slits of the double-slit experiment, so here for each final state we have to sum the amplitudes of all the scattering paths through the intermediate states. Again, the complex scattering amplitudes can constructively and destructively interfere.

For $L_{2,3}$ RIXS, which we are interested in here, the intermediate states are precisely the $L_{2,3}$ XAS final states. Thus, in Figure 3.7b, we show in green an example XAS spectrum, while one particular RIXS spectrum is shown in red. Note that we qualitatively show that the RIXS spectrum has sharper features than XAS. This is a consequence of different lifetimes of the excitations. The XAS final states are highly excited (recall the binding energies of a few hundred eV given in Figure 3.3) and are very short lived. By the uncertainty principle, this means they become broadened in energy. For many RIXS processes such as the *dd* excitations described below, the lifetimes are much

[7] For a simple yet very informative discussion of double slit experiment, see Feynman's description in Ref. [51].

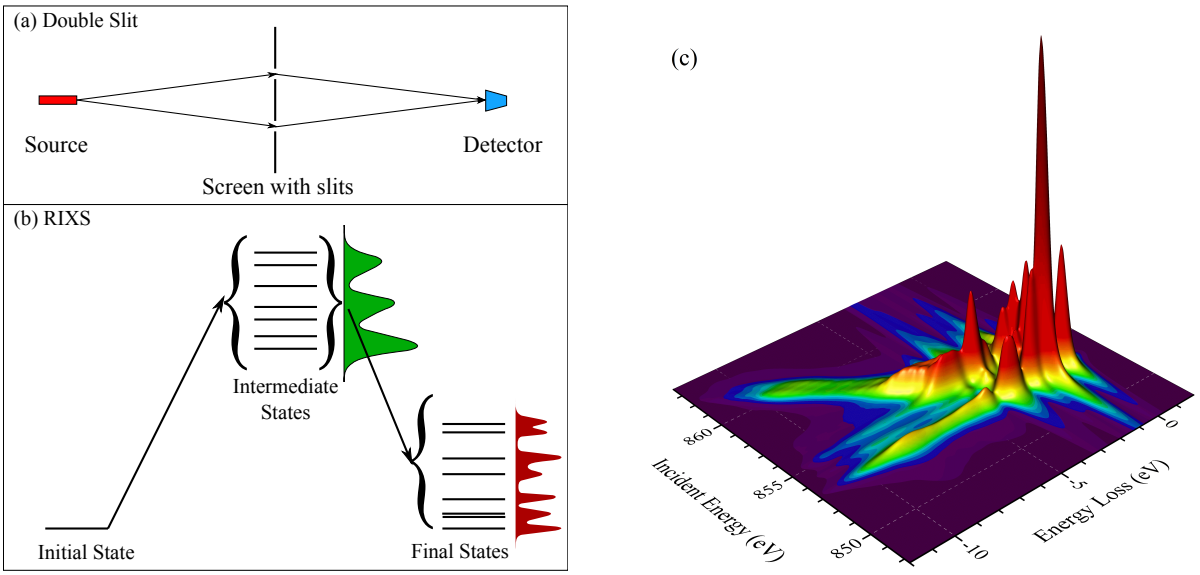

Figure 3.7: RIXS properties. (a) A double-slit experiment, for comparison of interference effects. (b) The three steps of the RIXS process. (c) Demonstration of dependence on incident (resonance) energy using an impurity model calculation for NiO.

longer and the lifetime broadening is much reduced.

The resonant nature of RIXS means that we can tune the incident photon energy to specific values, and obtain an entirely different RIXS spectrum for each incident energy. In Figure 3.7b for example, we might set our incident photon energy to the middle intermediate (green) state peak, and thus obtain a RIXS spectrum where the scattering paths through the intermediate states near the middle green peak are enhanced. A demonstration of this incident energy dependence is shown in Figure 3.7c. Here we show a series of RIXS spectra for NiO as the incident energy is scanned across the Ni L_3 absorption edge. This is actually an Anderson Impurity Model calculation (see Chapter 4), but is almost identical to what has been observed in experiment [52]. Each slice in this plot parallel to the energy loss axis is a single RIXS spectrum. The individual RIXS spectra vary strongly for different incident energies. Thus, one can see that a lot of information is potentially available with RIXS (although in actual experiments it is very time consuming to obtain a full "map" such as this).

In Figure 3.8, we schematically show some of the most common types of excitations measured with RIXS. Recall that observing an excitation in RIXS means that the system has been left in an excited state after the scattering event, so the energy of the scattered photon is less than that of the incident photon. Thus, in the Figure we plot the excitations on an energy loss scale, common

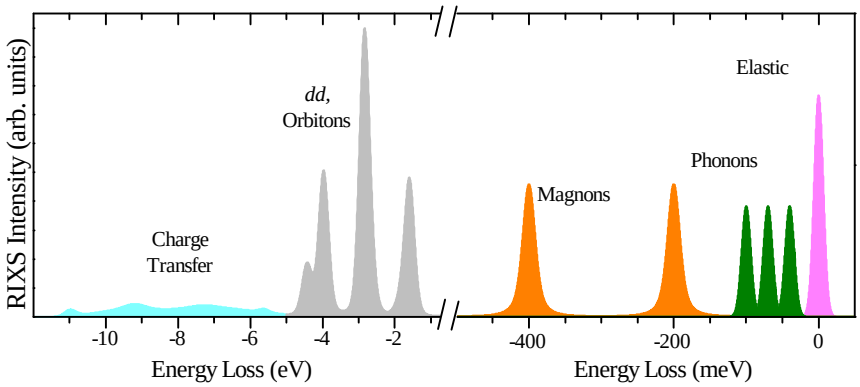

Figure 3.8: Some excitations which contribute to the RIXS spectrum.

for RIXS spectra. It is evident that many kinds of excitations can be measured over a wide range of energy scales. Phonons are lattice vibrations, magnons are collective spin excitations, and orbitons are collective orbital excitations, but we will not study these excitations in this work. Here, it is the *dd* and charge transfer (CT) excitations that we are interested in.

The *dd* excitations are simply final states in which the $3d$ electrons have been rearranged compared to the ground state, leading to a higher energy multiplet configuration (recall the multiplet energy levels shown in Figure 2.3). Thus, these excitations are highly sensitive to the energy levels of the $3d$ orbitals, and consequently the local environment of the ion. One of the pioneering experimental works for soft x-ray, $L_{2,3}$ RIXS was by Butorin and co-workers, who measured RIXS spectra of MnO [53]. They were able to resolve *dd* excitations in their spectra, which were in general agreement with approximate atomic calculations. Today, cutting edge beamlines are able to measure *dd* excitations at very high resolutions, demanding a much more accurate theoretical analysis.

Charge transfer excitations are final states in which a ligand valence band electron has hopped onto the transition metal site in one of the $3d$ orbitals. These excitations are typically at higher energies than the *dd* (as shown in Figure 3.8), and are also inherently broader since they involve transitions from the broad ligand band. Our studies in later chapters take advantage of these excitations to study the energies of band gaps in charge transfer semiconductors and insulators.

A comparison of *dd* versus CT excitations can be made using Figure 3.7c. For this case, the most visible *dd* excitations are positioned in the range from about 0 to -5 eV energy loss,[8] while the CT excitations are roughly from -5 to -10 eV. The *dd* excitations remain at a constant energy loss for changing incident energy; only the relative intensities of the excitations change. Charge

[8] Actually, NiO has *dd* excitations at energy losses near 10 eV as well (see the eigenstates plotted in Figure 4.4b, for example), but these are broadened and generally not visible.

transfer excitations show a slightly different behaviour. For 853 eV incident energy, there is a wide band of CT excitations. This resonant energy corresponds to the ionic L_3 XAS maximum, so we are accessing the CT excitations through hybridization, which causes some CT character to be mixed into that L_3 peak. However, at higher incident energy, we see the CT excitations are sharper and actually disperse for changing incident energy. As the incident energy increases from 855 to 862 eV, the CT excitations disperse from -5 to -10 eV. This region of incident energies excites directly into the CT band of the XAS, causing the dispersive behaviour. Thus, by tuning to different energies we can distinguish between the different excitations in the RIXS spectra if needed.

3.2.1 Detection Techniques

For RIXS experiments, we must detect the scattered photons in an energy resolved manner. As depicted in Figure 3.8, we need relatively high energy resolution, with less than 1 eV required for *dd* and CT excitations and less than 100 meV for magnons and other low energy excitations. This level of energy resolution in the soft x-ray range is currently only provided by grating spectrometers (solid state detectors are available, but have resolutions of around 100 eV and are usually used for PFY XAS). Because photon scattering cross sections are quite small (electron yields dominate for the soft x-ray $L_{2,3}$ edges), and grating diffraction efficiencies are small, RIXS experiments are more time consuming than XAS, and absolutely require the photon intensities provided by synchrotrons. The diffracted x-rays are collected by an area sensitive detector, and the resulting image looks, for example, like that in Figure 3.9. The individual bands in this image correspond to the peaks in our RIXS spectra. To extract the RIXS spectrum, we must first correct the curvature of the bands, which arises due to the diffraction geometry. Once the image is corrected, we can sum the individual rows of pixels for each column to end up with the 2D RIXS spectrum. Finally, using a combination of the diffraction formulas and reference spectra, the energy axis is calibrated to an eV scale. As part of the work for this thesis, a new approach was implemented to account for varying curvature across the detected image, and for more precise (subpixel) image correction. We discuss these contributions in Appendix A.

3.3 Nonresonant X-ray Emission

By tuning the incident photon energy well above the edge of interest, but still measuring the photons emitted by the sample in an energy-resolved manner like RIXS, one enters the regime of

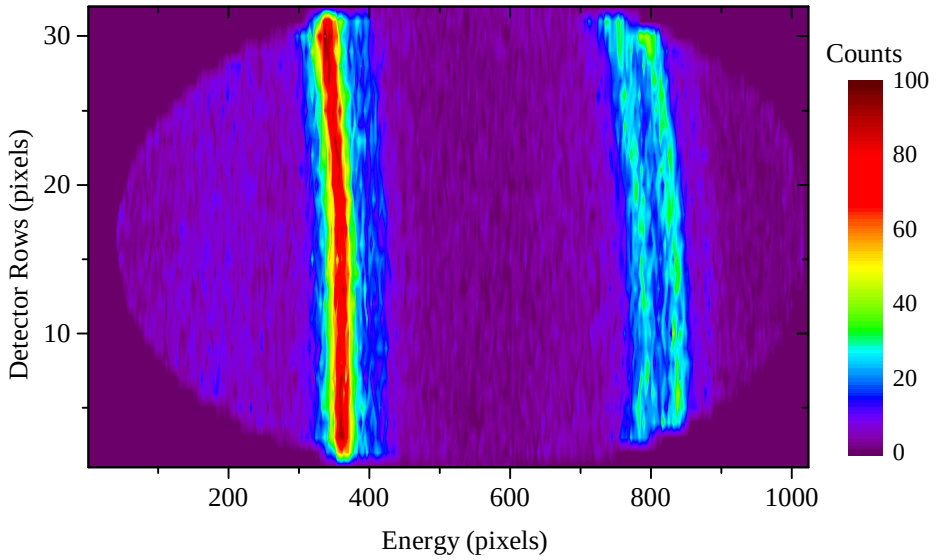

Figure 3.9: Example RIXS detector image. To extract the actual RIXS spectrum, the image must be corrected for curvature and the individual rows summed together. Also, the energy axis must be calibrated from pixels to eV.

Non-resonant X-ray Emission Spectroscopy (NXES) [54] (alternatively called just XES). For NXES, the resonance effects are removed, and one simply measures decays of valence band electrons to fill the excited core hole. Thus, in many cases NXES spectra provide an approximation to the occupied DOS, projected according to the edge studied. For this work, NXES measurements are limited to the K edges of the ligands, where the spectra are indeed very close approximations to the VB DOS.

Similar to the arguments laid out earlier for K edge XAS, we see from Figure 2.4 on page 13 that due to hybridization, the $2p$ occupied DOS provided by ligand K edge NXES gives us a measurement of the overall valence band maximum energy. Thus, we can see that combining XAS and XES of the ligand K edge gives us an approximation of the bulk experimental band gap. An example of this approach applied to ZnO is shown in Figure 3.10. Here the second derivatives of the spectra are used to determine the band edges [44]. This technique gives a gap of 3.4 eV for ZnO (see Section 6.2), in agreement with the known gap [55]. The final state of XES does not involve a core hole, so the possible issues mentioned for XAS earlier as not as applicable here. While there is a VB hole in the final state, this creates a very minor perturbation which affects the spectrum very little.

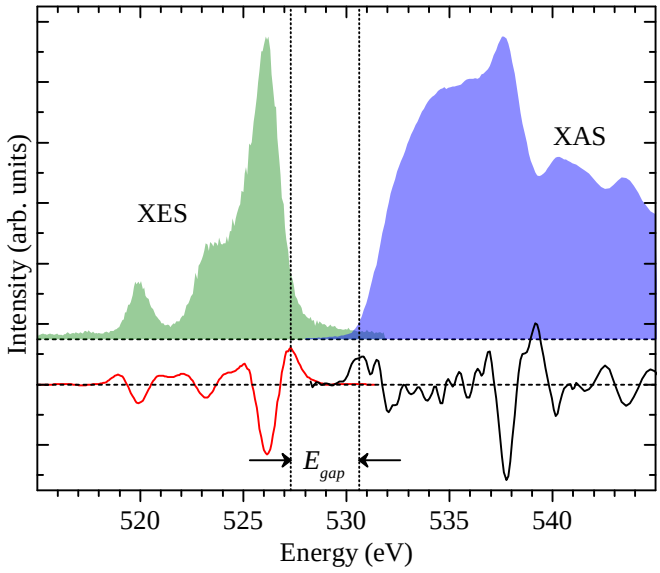

Figure 3.10: Band gap determination from ligand K edge spectroscopy. The oxygen K edge XAS and XES spectra for ZnO are shown, along with their second derivatives to demonstrate the band gap extraction. The dotted vertical lines mark the valence band maximum (left) and conduction band minimum (right), while the band gap is defined as the energy between them.

3.4 Fluorescence Yield X-ray Absorption

We now return to the subject of fluorescence yield XAS (either TFY or PFY), which was introduced in Section 3.1.3 above. We noted that fluorescence yield (FY) techniques are often susceptible to distortions. This can be demonstrated by considering the general expression for PFY XAS intensity of a thick sample, written as [47, 56, 57]

$$\frac{I_{PFY}\left(\omega,\omega'\right)}{I_0\left(\omega\right)} \propto \frac{\epsilon_x\left(\omega,\omega'\right)\mu_x\left(\omega\right)}{\mu\left(\omega\right)+\mu\left(\omega'\right)\frac{\sin\alpha}{\sin\beta}} \tag{3.3}$$

where ω (ω') is the ingoing (outgoing) photon energy, x is the edge of interest, ϵ_x is the fluorescence efficiency factor of the edge, μ_x is the absorption coefficient of the edge, μ is the total absorption coefficient, and α (β) is the angle of the incident (outgoing) photon direction with respect to the sample surface. A comparison of μ_x versus μ can be made in Figure 3.1—the entire spectrum is related to μ, while the non-background portion of the figure corresponds to μ_x.

For an edge that absorbs very strongly compared to the background absorption, we have $\mu_x \approx \mu$. This occurs when the atoms with the absorption edge x are highly concentrated and have inherently strong absorption. If we note that the second term in the denominator of Equation 3.3 is approximately constant and smaller (since it involves absorption at energies lower than the edge),

and the fluorescence efficiency in the numerator is approximately constant, we see that our intensity becomes

$$\frac{I_{PFY}(\omega, \omega')}{I_0(\omega)} \approx \frac{\mu_x(\omega)}{\mu(\omega)} \approx 1 \tag{3.4}$$

and we therefore no longer measure a varying XAS. This is where the term *saturation* comes from, and edges with strong absorption will produce FY spectra which appear compressed, rendering the data mostly unusable.

Self absorption[9] occurs when the emitted photons (which are to be detected by the fluorescence yield detector) are reabsorbed by the sample before they can escape. This phenomenon is always present, but in certain cases, the emitted energy depends strongly on the incident energy, and μ varies over the range of emitted energies. This means the outgoing photons are reabsorbed more strongly at different parts of the XAS spectrum, again leading to a distorted spectrum. Note that this type of distortion is less understood than saturation, and very difficult to quantify or correct for.

Finally, there are possible distortions inherently built into the fluorescence decay process in general, even for dilute or weakly absorbing systems. When we measure the fluorescence given directly from the edge we are exciting, it means we are actually measuring the emission energy integrated (total) RIXS signal as our way of detecting XAS. It turns out that when multiplet effects are important, the overall decay rates of the RIXS process depend strongly on the XAS excitation energy [57]. In Chapter 4 we will develop the theory necessary to understand this more fully, and in Chapter 7 we describe a study we performed regarding this concept. We found that indeed PFY XAS is often very different from pure XAS, but also that it can be a very useful tool on its own with some exciting prospects for spin-sensitive measurements.

3.5 Experimental Facilities

The experimental spectra presented in this work were all measured using either of two facilities: the Spherical Grating Monochromator (SGM) beamline at the Canadian Light Source (CLS), or Beamline 8.0.1 (BL8) at the Advanced Light Source (ALS). Here we provide the pertinent details of these facilities.

[9] *Self absorption* and *saturation* are often used interchangeably and to refer to similar effects. Here, we use the definitions given in Ref. [57] which clearly distinguish between the two phenomena.

3.5.1 The SGM beamline at the Canadian Light Source

The SGM beamline [58] at the CLS is primarily used for XAS and X-ray Photoelectron Spectroscopy (XPS) in the soft x-ray range covering energies from 250 – 2000 eV. However, the beamline does have capabilities for other techniques as well, such as X-ray Excited Optical Luminescence (XEOL). Here we describe the XAS facilities, since they were used for much of the data contained in this thesis.

The SGM provides linear polarized light with high energy resolution ($E/\Delta E$ of over 5000 at most energies), and has several detectors useful for XAS. First is the standard TEY detector, which simply measures the current flowing from the sample to electrical ground while ejected electrons are replenished after absorbing x-rays. Second, the beamline is capable of TFY detection using either photodiodes or microchannel plates, which simply detect the majority of x-rays given off by a material (regardless of their energy) after it absorbs incident x-rays. Finally, the SGM employs some rather unique and uncommon detectors which are quite useful. These are PFY detectors which can detect emitted x-rays with a moderate energy resolution (ΔE of 100 eV FWHM) but high efficiency. These detectors allow for the selection of particular fluorescence lines when performing an XAS experiment, which can be very beneficial, as discussed in Chapter 7. Additionally, they allow for the implementation of the inverse partial fluorescence yield (IPFY) technique, pioneered at the SGM several years ago [47,48]. All of these capabilities make the SGM a very powerful (and highly demanded) beamline.

3.5.2 Beamline 8 at the Advanced Light Source

Beamline 8.0.1 at the ALS has facilities for XAS as well, but is primarily used for its well-established x-ray fluorescence spectrometer [59]. Like the SGM, BL8 provides high resolution, linearly polarized light. The endstation has a Rowland-circle type grating spectrometer, oriented such that the scattering is fixed at 90° to the incident beam, with the linear polarization in the scattering plane. The various gratings operate over an energy range from ~100 eV to over 1000 eV, covering the $L_{2,3}$ edges of all the $3d$ transition metals. As described earlier, an area-sensitive imaging detector is used to detect the photons dispersed by the diffraction gratings. While BL8 is no longer at the leading edge in terms of RIXS resolution, it is nonetheless very highly demanded because it is very reliable and efficient.

Chapter 4

Theoretical Interpretations of Experiments

> *The underlying physical laws necessary for the mathematical theory of a large part of physics and the whole of chemistry are thus completely known, and the difficulty is only that the exact application of these laws leads to equations much too complicated to be soluble.*
>
> —Paul Dirac, 1929 [60]

The experimental techniques described in the previous chapter can provide a wealth of information about materials under study, but it is not always obvious how to extract this information from the spectra. One course of action that is sometimes successful is to compare the spectra obtained to those of other, well-understood materials. By uncovering similarities (or differences) in the spectra, it is often possible to learn much about the electronic structure of a new material by considering how it relates to another material. However, in many cases no suitable reference materials are available, or unexplainable features are observed, and a purely theoretical interpretation of the results is necessary. Here we describe some powerful quantum mechanical approaches for analyzing $L_{2,3}$ transition metal XAS and RIXS spectra.

4.1 Approximations

Even in the earliest days of the development of quantum mechanics it was understood that, while the theory was very elegant and powerful, there would be significant difficulties applying it in full form to many physical applications, such as the electronic structure of condensed matter. This is evident in the famous excerpt above from Dirac's work. The reason for this difficulty is that physical systems contain many particles, and a full application of theory to understand such systems would need to consider all possible interactions between pairs of particles. Even when using modern computational facilities and studying highly symmetric structures, it is prohibitive to include all interactions explicitly.

To circumvent this issue of intractability, we must determine which natural phenomena contribute most to our experimental findings, and find ways to best understand their behaviour in an approximate way. As an example, for ligand K edge spectra, it is known that one probes something very similar to the element- and p symmetry-projected DOS, so a theoretical description based on band theory using techniques such as density functional theory (DFT) works very well (see Ref. [45] for an early example). However, for our main focus here, L edge transition metal spectra, it was found in the 1980s that the spectra are dominated by local effects, so a full description of the atomic eigenstates is a good starting point, and longer range interactions can be included when possible and as necessary.

The data we will be interested in simulating result from core level spectroscopy processes. Thus, we will need to construct wavefunctions for ground and excited states, and calculate spectra arising from transitions between these states. Specific details for obtaining the wavefunctions using different models will be discussed later in Section 4.3, but first we will discuss the details regarding the simulation of spectra once the wavefunctions are known.

4.2 Simulating X-Ray Spectra

For all of the spectroscopic techniques discussed in this work, we have monochromatic incident photons which interact with the core level electrons of a material, causing a transition from an initial state $|i\rangle$ to a final state $|f\rangle$. For XAS this is a single dipole transition, while RIXS is a second order process and we have a pair of sequential dipole transitions. Recall that the long wavelengths of soft x-rays limit us to dipole transitions; other related techniques (which are not the focus here) can involve higher multipole transitions.[1]

We can represent the probability of the absorption of a photon using Fermi's Golden Rule #2. For the absorption cross-section of dipole excitations into an infinitely long-lived final state, we have [15, 61]

$$\sigma(\omega) = 4\pi^2 \alpha\omega \left|\langle f|\boldsymbol{\epsilon}\cdot\mathbf{r}|i\rangle\right|^2 \delta\left(E_i + \omega - E_f\right) \tag{4.1}$$

where ω is the energy of the incident photons, α is the fine structure constant, $|i\rangle$ ($|f\rangle$) is the initial (final) state with energy E_i (E_f), $\boldsymbol{\epsilon}$ is the polarization vector of the light, and $\mathbf{r}$ is the position operator. For our core-level excitations we have relatively short-lived states, so the delta function

[1] Hard x-ray XAS, as well as x-ray and electron scattering with significant momentum transfer to the sample, can produce higher multipole transitions.

is replaced by a Lorenztian profile [62, 63]. Also, we are generally only concerned with spectral shapes, rather than absolute cross sections, so we can rewrite Equation 4.1 as an approximate proportionality relation. Thus, accounting also for a set of possible final states, we have for the XAS intensity

$$I(\omega) \propto \sum_f |\langle f|\boldsymbol{\epsilon}\cdot\mathbf{r}|i\rangle|^2 \times \frac{\Gamma_f/\pi}{(E_i+\omega-E_f)^2+\Gamma_f^2} \tag{4.2}$$

where Γ_f is the HWHM of the lifetime-induced Lorentzian profile for final state $|f\rangle$. This expression is what is typically applied for calculating XAS spectra within the local cluster approach [54, 57]. Note that another popular option involves using correlation functions [62, 64, 65], which lead to the same spectra but are not discussed here.

We will take one last step before arriving at the expression we have implemented in the programs used for this work. We explicitly separate the polarization and geometry dependence from the individual dipole excitation components. This has the advantage of allowing us to quickly simulate spectra for various geometries after calculating only one set of transition probabilities, which is the time consuming step.

Noting that $\boldsymbol{\epsilon}\cdot\mathbf{r} = \sum_\alpha \epsilon^\alpha r_\alpha$, where $\alpha = -1, 0, 1$ in a spherical basis or $\alpha = x, y, z$ for Cartesian coordinates, we can rewrite Equation 4.2 to represent the XAS intensity for transitions starting from state $|i\rangle$ as

$$I_i^{XAS}(\omega, \boldsymbol{\epsilon}) \propto \sum_\alpha |\epsilon^\alpha|^2 \cdot \mathcal{F}_{i,\alpha}(\omega) \tag{4.3}$$

where we have dipole transition component intensities

$$\mathcal{F}_{i,\alpha}(\omega) = \sum_f |\langle f|r_\alpha|i\rangle|^2 \times \frac{\Gamma_f/\pi}{(E_i+\omega-E_f)^2+\Gamma_f^2} \tag{4.4}$$

For both Cartesian and spherical bases, we derive the polarization vector components of the incident light (ϵ^α), adapted from the work of Ferriani [66] and Stöhr [15], in Appendix B.

Expressions for RIXS can be formulated in a similar manner. RIXS is a second order process, however, and is described by the Kramers-Heisenberg formula (also known as Fermi's Golden Rule #1). A thorough derivation with nice explanations is given by Sakurai [63], while Tulkki and Åberg were among the first to apply the formula to RIXS calculations [67, 68]. If we focus on only the resonant portion of the Kramers-Heisenberg formula, expressed in the typical form used for

RIXS [49,54], we have

$$I_i^{RIXS}\left(\omega,\omega',\boldsymbol{\epsilon},\boldsymbol{\epsilon}'\right) \propto \sum_f \left| \sum_n \sqrt{\frac{\Gamma_n}{\pi}} \frac{\langle f|\boldsymbol{\epsilon}'^* \cdot \mathbf{r}|n\rangle\langle n|\boldsymbol{\epsilon} \cdot \mathbf{r}|i\rangle}{E_i+\omega-E_n+i\Gamma_n} \right|^2 \times \frac{\Gamma_f/\pi}{\left(E_i+\omega-\omega'-E_f\right)^2+\Gamma_f^2} \tag{4.5}$$

Here variables are defined as they were for XAS, and the primed variables correspond to the outgoing photon and the decay transitions. Typically we do not detect the scattered photons with polarization dependence, so individual intensities for different orthogonal polarization vectors are summed together. Again we modify this expression slightly, similar to the formulation presented by Ament and co-authors [50], expressing the RIXS intensity starting from a particular initial state $|i\rangle$ as

$$I_i^{RIXS}\left(\omega,\omega',\boldsymbol{\epsilon},\boldsymbol{\epsilon}'\right) \propto \sum_f \left| \sum_{\alpha,\alpha'} \epsilon^\alpha \left(\epsilon'^{\alpha'}\right)^* \mathcal{F}_{\alpha\alpha'}^{if}\left(\omega\right) \right|^2 \times \frac{\Gamma_f/\pi}{\left(E_i+\omega-\omega'-E_f\right)^2+\Gamma_f^2} \tag{4.6}$$

The component scattering amplitudes from initial state $|i\rangle$ to final state $|f\rangle$ are then defined as

$$\mathcal{F}_{\alpha\alpha'}^{if}\left(\omega\right) = \sum_n \sqrt{\frac{\Gamma_n}{\pi}} \frac{\langle f|r_{\alpha'}^\dagger|n\rangle\langle n|r_\alpha|i\rangle}{E_i+\omega-E_n+i\Gamma_n} \tag{4.7}$$

Note that there are nine different scattering amplitudes from each initial state to each final state (although some may be zero), which are permutations of values for the α, α' indices. For XAS we had 3 different contributions (one for each value of α). The significant advantages of clearly separating these material dependent amplitudes from the geometry dependent polarization factors will become more evident in Section 4.4 where we discuss the computational approaches we use to obtain the wavefunctions and calculate the spectra. Briefly, by using the Lanczos algorithm as discussed in that section, we can take a problem which involves a very large basis (i.e. matrices of order 10^5) and obtain the 3 XAS component intensities or 9 RIXS component amplitudes that are transformed into a much smaller basis (order 10^2 or so). Thus, we can very quickly combine these component spectra using different geometry dependent polarization factors to simulate different experimental conditions, whereas we would need to start with the large original basis and perform the diagonalizations again to simulate different geometries if we did not take this approach.

4.2.1 Temperature Dependence

A close look at Figure 2.3 on page 11 will reveal that often one can have excited state multiplets very close in energy to the ground state. If the energies of these multiplets are within a few factors

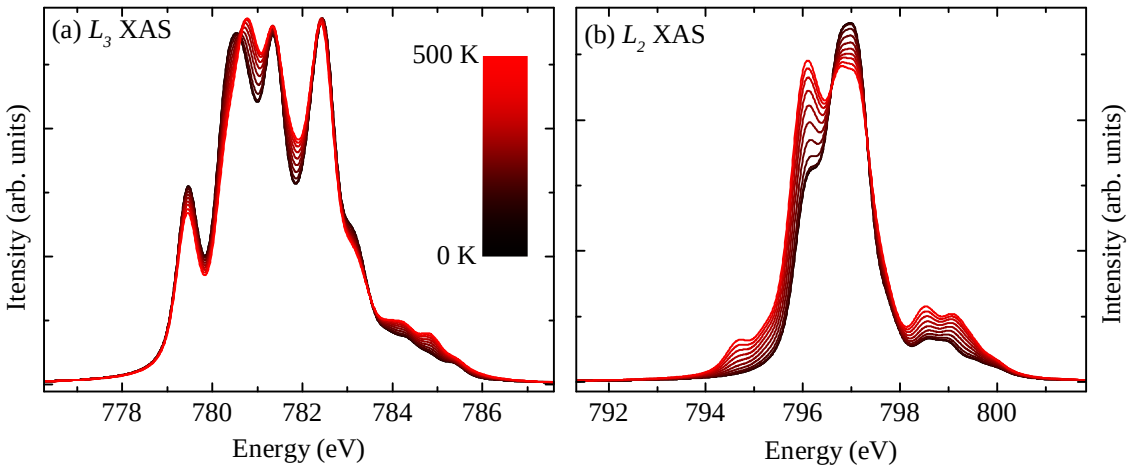

Figure 4.1: Example of the temperature dependence of XAS for Co^{2+} in O_h symmetry. The spectra are from a crystal field XAS calculation with $10Dq = 1.0$ eV, spin-orbit interactions included, and Slater integrals set to 80% of Hartree-Fock values. (a) XAS in the L_3 region. (b) XAS in the L_2 region. See section 4.3.2 for details about the crystal field model.

of k_BT from the ground state—where k_B is the Boltzmann constant and T is temperature—then they will be populated due to thermal excitations according to Boltzmann statistics. Thus, our experiments (often carried out at room temperature, where k_BT is ~26 meV) are actually probing excitations from this set of populated initial states into final states. It is often very important to take this detail into account when simulating spectra, as has been shown for CoO [69]. In order to do this, we simply need to carry out calculations from each relevant initial state, weighting the overall intensity by the Boltzmann factor. For temperature dependent XAS, we have

$$I_{XAS}\left(\omega, \boldsymbol{\epsilon}, T\right) = \sum_i \frac{1}{Z} \exp\left(-\frac{E_i - E_g}{k_B T}\right) I_i^{XAS}\left(\omega, \boldsymbol{\epsilon}\right) \tag{4.8}$$

where $Z = \sum_i \exp\left(-\frac{E_i - E_g}{k_B T}\right)$ is the partition function, E_g is the ground state energy, and all other symbols are defined as before. For the paradigmatic case of Co^{2+} in O_h symmetry, an example of the temperature dependence is shown in Figure 4.1. It should be noted that this characteristic temperature dependence of XAS can be quite useful. For example, in systems with mixed spin states or low energy spin transitions, one can perform XAS at varying temperatures to reveal information about the individual configurations.

Similar arguments hold for the temperature dependence of RIXS. Again, we must sum complete RIXS spectra originating from each relevant initial state, scaling their intensities appropriately

according to the Boltzmann weighting. The temperature dependent RIXS is then

$$I_{RIXS}\left(\omega,\omega',\boldsymbol{\epsilon},\boldsymbol{\epsilon}',T\right)=\sum_i\frac{1}{Z}\exp\left(-\frac{E_i-E_g}{k_BT}\right)I_i^{RIXS}\left(\omega,\omega',\boldsymbol{\epsilon},\boldsymbol{\epsilon}'\right) \tag{4.9}$$

Equations 4.8 and 4.9 are the expressions used for the calculation of XAS and RIXS spectra throughout this work.

4.3 Model Hamiltonians

Above we introduced the quantum mechanical descriptions of the excitations induced by the x-ray probes we use in this work. Often one can gain valuable insight into the material properties by analyzing the spectra using a model Hamiltonian approach. With this terminology, we mean that we construct a Hamiltonian which encapsulates as much of the important physics of the material as possible (the full many body problem for a solid is at present intractable, and likely will remain so in the foreseeable future). Armed with appropriate model Hamiltonians for the initial and final states, one can solve Schrödinger's equation,

$$H\Psi=E\Psi \tag{4.10}$$

to determine the initial and final state wavefunctions, $|i\rangle$ and $|f\rangle$. We can then use the expressions from the previous section to simulate spectra.

Using the approach above, one can study variations in the spectra depending on the inputs to the Hamiltonians, and from comparison to the experimental spectra, we can learn about the electronic structure of the material under study. The information which can be learned then depends on the model that we use to study the system. Below we introduce various possible models of increasing complexity.

4.3.1 Atomic Model

As mentioned in Chapter 2, even for an isolated atom, there exists no analytical solution to the Schrödinger equation if more than one electron is present. However, accurate self-consistent iterative approaches have been developed [9], and with modern computers solutions can be obtained very

quickly for single atoms. For an atomic model, our Hamiltonian takes the form[2] (see, e.g., [9, 24]):

$$H_{atom} = H_k + H_{n-e} + H_{e-e} + H_{so} \tag{4.11}$$

$$= -\frac{\hbar^2}{2m}\sum_i \nabla_i^2 - \sum_i \frac{Ze^2}{r_i} + \sum_{i<j}\sum \frac{e^2}{r_{ij}} + \sum_i \xi_i\left(r_i\right)\left(\mathbf{l}_i \cdot \mathbf{s}_i\right) \tag{4.12}$$

where the four terms represent the electron kinetic energy, the electron-nucleus interaction, the electron-electron interaction, and the electron spin-orbit interaction. Note the summation indices are over electrons, and r_i is the distance between the origin (nucleus) and electron i, while r_{ij} is the distance between two electrons i and j. The operators $\mathbf{l}_i$ and $\mathbf{s}_i$ are the orbital and spin angular momentum operators and ξ_i is a proportionality factor. For this atomic model, Cowan has developed a widely used and very successful set of programs [9] that can calculate eigenstates and dipole spectra, among (many) other things.

The electron-electron interactions lead to the formation of what are often called Slater integrals [9]. These integrals are given as energy parameters defining the intra-atomic Coulomb and exchange interactions between electrons, and are the primary empirical parameters used in the atomic model. Configuration interaction effects result in the values of these parameters being reduced to 80–90% of the calculated Hartree-Fock values for free ions. In solids, the interactions are somewhat screened, and calculations using a further reduction of the energies are needed to obtain agreement with experimental spectra [54].

As might be expected, the atomic model has a somewhat limited usefulness for studying real condensed matter systems. In solids, the valence electrons of atoms do not behave as they do for isolated atoms—delocalization and hybridization to varying degrees can strongly alter the electronic properties. However, in some cases one can use the atomic model to identify a *lack* of bonding interactions. A prime example of this is with the $4f$ electrons of rare earths. As with the $3d$ electrons of transition metals, the $4f$ electrons do not have radial nodes, and exhibit an even stronger localization than the $3d$. Some bonding does still occur in materials containing rare earths, but it has been shown that x-ray spectra of rare earth compounds are very well described by atomic models [12, 13], verifying the extremely localized nature of the $4f$ electrons.

[2]Note we neglect inter- and intra-nucleus interactions here, since they do not factor into the electronic structure we are interested in.

4.3.2 Crystal Field Model

The rare earths and several other specific cases aside, we need to move past the atomic model to learn much about materials containing $3d$ transition metals. A unique approach was taken in this field by Hans Bethe in 1929 [70], when he simplified the problem of an atom in a solid by modelling the neighbouring atoms as point charges. Then the electrons on the atom of interest are only subject to an electrostatic potential which has a particular point group symmetry and field strength. This field leads to a splitting of the energy levels of the central atom. This treatment is termed the *crystal field model*. Traditionally, the crystal field model found success in the analysis of magnetic susceptibilities [71] and optical spectra [24]. For optical studies, by considering the effects of crystal fields on the energy levels of the atomic multiplets, researchers had success understanding the energies of dd excitations in their spectra. The only change moving from the atomic to crystal field model is to add a term to the Hamiltonian representing the crystal field potential [24,54]:

$$H_{CFM} = H_{atom} - eV(\mathbf{r}) \tag{4.13}$$

where e is the electronic charge and V is the potential.

In the 1980s the crystal field model was applied to the analysis of L edge XAS spectra [43,72,73] with great success (albeit using empirical fitting parameters rather than explicit charge density distributions). Whereas optical studies only focused on the energies of the multiplets, with XAS the researchers could simulate actual spectral shapes, and the agreement with experiment was very good for ionic compounds.

In Figure 4.2, we show the effect of crystal fields with various symmetries on the $3d$ orbital energies. Neglecting inter-electronic interactions for clarity (i.e. using the single particle approximation), we see that the $3d$ orbitals are degenerate for an atom in spherical symmetry. If this atom is then subjected to a six-fold coordination of ligands (O_h symmetry) the orbital energies split into two groups. As noted when discussing Figure 2.2b, two of the orbitals have angular lobes directed along the Cartesian axes (denoted the e_g orbitals for O_h symmetry), while the other three are directed between the axes (denoted the t_{2g} orbitals). Since six-fold O_h coordination has ligands arranged on the axes around the transition metal, the e_g electrons are more strongly affected by the crystal field. This means the e_g orbitals have higher energy than the t_{2g} orbitals. The energy splitting between these groups of orbitals is given the name $10Dq$.

For an actual crystal field model calculation, we do in fact include the electron-electron interactions (as shown above in the atomic Hamiltonian) which lead to the multiplet energy levels discussed

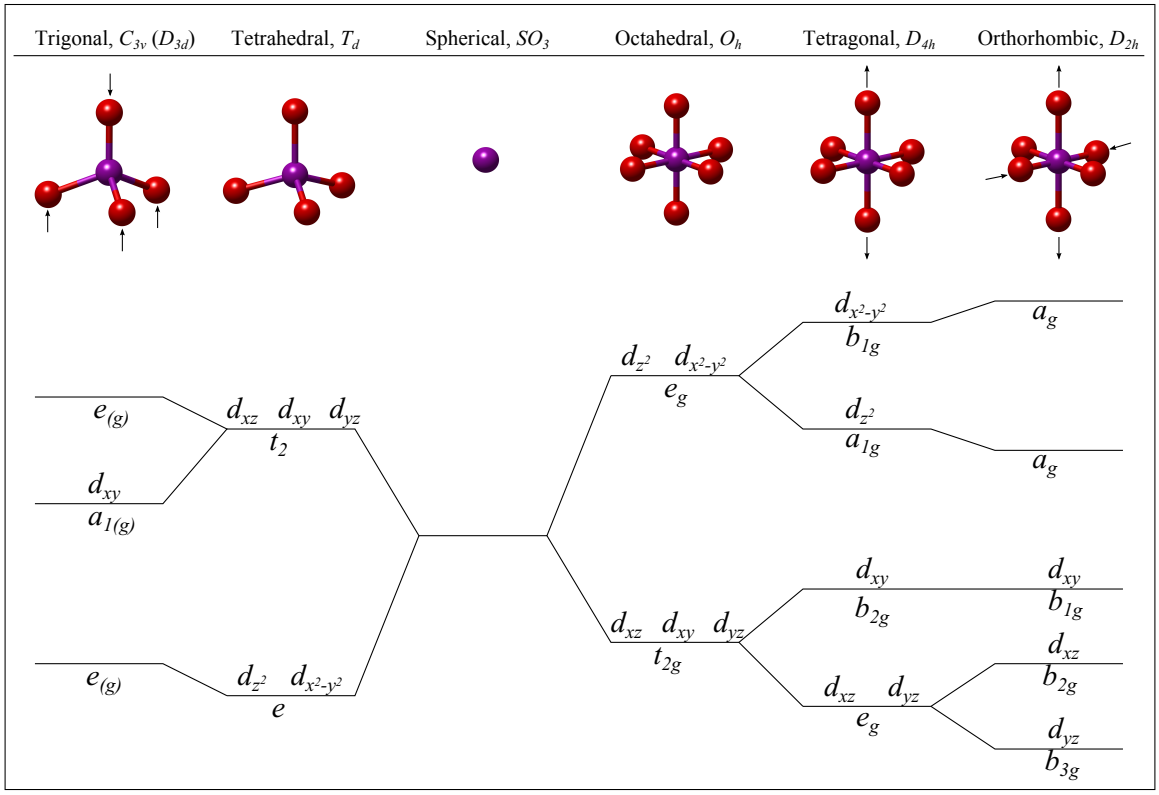

Figure 4.2: Crystal field symmetries relevant for this work. The specific arrangements of neighbouring atoms lead to the energetic splitting of the $3d$ orbitals into different groups.

in Chapter 2. The crystal field potential then shifts the energies of the various multiplet eigenstates depending on their population of e_g and t_{2g} orbitals. Thus, the various energy levels end up being very sensitive to the symmetry of the local bonding geometry.

Figure 4.2 shows the effects of the other bonding symmetries which are relevant to this work. Tetrahedral symmetry leads to splitting into the same e and t_2 groups as O_h symmetry does (the g subscripts are removed for T_d because inversion symmetry is no longer present), but now the splitting is reversed because the t_2 orbitals are closer to the ligands. Cubic 8-fold coordination (not shown) leads to a similar splitting as T_d, but larger in magnitude. Trigonal and orthorhombic symmetries lead not only to energy splittings, but they also cause a mixing of the individual orbitals. Where d orbital designations are not given in the Figure, it is because of this mixing.

It is evident for lower symmetries that the orbitals split into more energy levels, and therefore more parameters are needed to describe the effects. For O_h and T_d groups we have $10Dq$ as explained above. For D_{4h} we have $10Dq$, Ds, and Dt, and for D_{2h} we have these three plus Du and Dv. For trigonal symmetry, which is C_{3v} for a distorted tetrahedron and D_{3d} for a distorted octahedron, we have $10Dq$, $D\sigma$, and $D\tau$. Specific expressions for the one-electron energy levels in terms of these

parameters are given in Appendix C, and can also be found in the literature [24,54,74].

4.3.3 Ligand Field (Cluster) Model

The crystal field model works surprisingly well considering its simplicity. However, in materials with more substantial bonding interactions (e.g. materials with anions that have higher electronegativities or cations with higher oxidation states), one does not always get satisfactory results using the crystal field model. Additionally, certain experimental techniques lead to spectra which are more sensitive to hybridization (i.e. core level XPS or charge transfer RIXS) rather than crystal field multiplet information (i.e. core XAS). A natural improvement upon the crystal field model is to not only include the electrostatic effects of the ligands, but also incorporate the hybridization effects of bonding into the model. One possible way of doing this is to include in the model the central transition metal atom and the nearest neighbour ligand atoms, leading to what is called the cluster model, or ligand field model [24,54].

The interaction with the ligands is incorporated through what is known as configuration interaction mixing. We include specific types of configurations (arrangements of the electrons within the cluster) and mix them together with hopping matrices. For the materials and techniques in this thesis, the important configurations are the ionic configuration (where the transition metal atom has a $3d^n$ configuration and the $2p$ orbitals of the ligands are all full), and ligand to metal charge transfer configurations. We denote the ligand to metal charge transfer configurations as $3d^{n+m}\underline{L}^m$, where $\underline{L}^m$ denotes m holes on the ligand atoms. These configurations simulate the hopping of ligand electrons to the transition metal site, and thus the mixing approach simulates hybridization. Our total wavefunctions are then linear combinations of the different configurations [75,76], e.g.

$$|i\rangle = c_0|d^n\rangle + c_1|d^{n+1}\underline{L}\rangle + c_2|d^{n+2}\underline{L}^2\rangle + ... \tag{4.14}$$

where the weighting parameters c_i are determined by the relative energies of the configurations and the hopping integrals between them.

A schematic of the mixing configurations is shown in Figure 4.3 for the initial state of a system, as well as final states of some core level spectroscopic techniques. First, focusing on the initial state configurations, we see the ionic configuration is lowest in energy, with the $3d^{n+1}\underline{L}$ configuration being at an energy Δ above it.[3] Recall from Chapter 2 that Δ is termed the charge transfer energy,

[3]This does not always have to be the case. Some covalent materials that have cations with high oxidation states or ligands with low electron affinities can exhibit negative charge transfer energies.

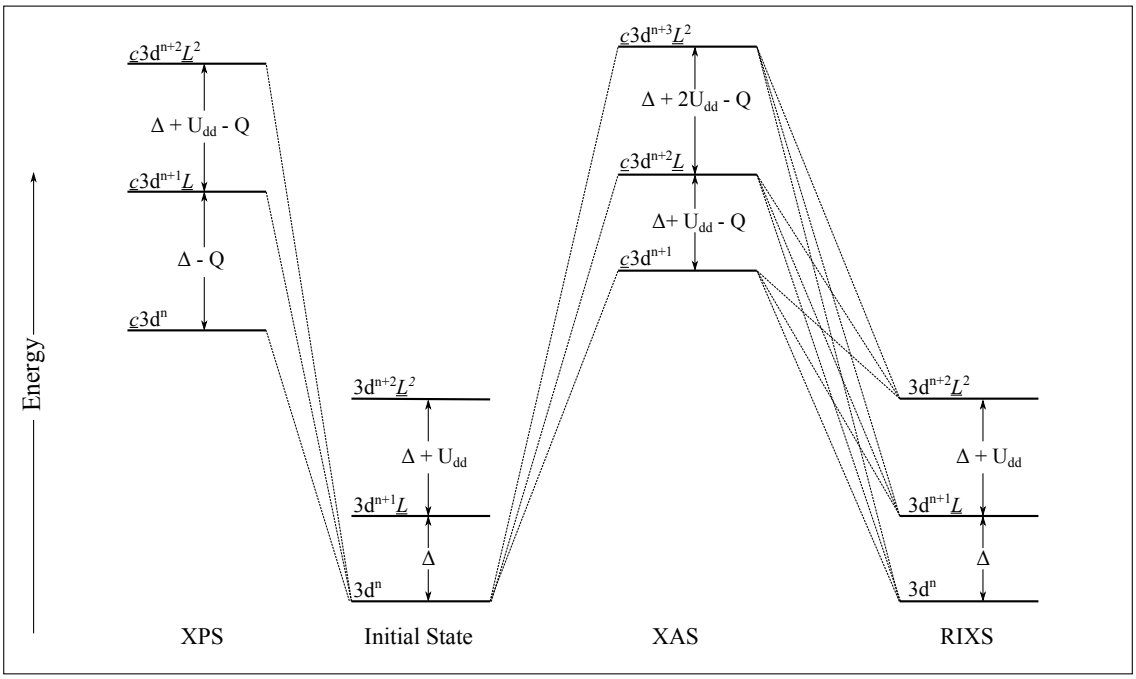

Figure 4.3: Configurations included in cluster model calculations. $\underline{c}$ denotes a hole in a core orbital, while $\underline{L}$ denotes a hole in a ligand orbital. The dotted lines represent the x-ray induced transitions to reach the final states of relevant spectroscopic techniques. The relative energies are given by the arithmetic expressions, with the parameters as defined in Table 4.1.

and is the energy required for a ligand electron to hop onto a transition metal site. The $3d^{n+2}\underline{L}^2$ configuration is another unit of Δ above the second configuration because it involves another charge transfer process, but also has a unit of Coulomb repulsion energy U_{dd} due to the interaction between the two extra $3d$ electrons present in this case.

Similar explanations apply for the final states of the various techniques. Each time a charge transfer process happens, we add a unit of Δ, and for every extra pair of electron-electron interactions, we add a value of on-site Coulomb repulsion, U_{dd}. Note there is a third parameter, the core hole potential Q, which is an interaction between the $2p$ core hole $\underline{c}$ created in a core level spectroscopy and any extra $3d$ electrons present due to charge transfer or other processes. Note for RIXS the configurations are the same as in the initial state, since we do not have a core hole present in the RIXS final states. The dipole transitions of the techniques are denoted by the dashed lines. Note that further hopping past the two ligand hole cases shown here can be included, but is not often necessary because the configurations are much higher in energy and have little effect (actually for XAS and RIXS we often get good results just going as far as single ligand hole configurations).

The steps for constructing our configuration interaction (CI) Hamiltonian are as follows. First,

we construct Hamiltonian matrices of the individual configurations. For the initial state, these would be

$$[H_0] = [3d^n] \tag{4.15}$$

$$[H_1] = \left[3d^{n+1}\underline{L}\right] \tag{4.16}$$

$$[H_2] = \left[3d^{n+2}\underline{L}^2\right] \tag{4.17}$$

where we will use [ ] to denote a matrix. Note that H_0 corresponds to the crystal field model Hamiltonian. Next, we calculate mixing (hopping) matrix elements between these configurations, i.e. V_{01} for hopping between H_0 and H_1, and V_{12} for hopping between H_1 and H_2. Our CI Hamiltonian can then be constructed as

$$H_{CI} = \begin{bmatrix} [H_0] & [V_{01}] & 0 \\ [V_{01}]^\dagger & [H_1] + \Delta\,[I] & [V_{12}] \\ 0 & [V_{12}]^\dagger & [H_2] + (\Delta + U_{dd})\,[I] \end{bmatrix} \tag{4.18}$$

where I is the identity matrix, used to shift the energies of the charge transfer configurations by the necessary amount. We proceed in a similar fashion for the final states of whichever spectroscopy is under consideration. Using the individual dipole transition matrices between the initial and final configurations, we construct a new transition matrix within our configuration interaction basis, given as

$$T_{CI} = \begin{bmatrix} [T_0] & 0 & 0 \\ 0 & [T_1] & 0 \\ 0 & 0 & [T_2] \end{bmatrix} \tag{4.19}$$

We now have our initial and final state Hamiltonian matrices and our transition matrix so we can proceed with calculating the spectra using the techniques described earlier. The full set of parameters for this model are summarized for clarity in Table 4.1.

Figure 4.4 shows the effects of hybridization in the cluster model for Ti^{3+} (a $3d^1$ system) and Ni^{2+} (a $3d^8$ system), including the ionic and single ligand hole configurations. Here we plot the energy levels of the multiplets for the two systems as a function of hybridization strength. Starting at the left side of either plot, the hopping integrals are set to zero, so no hybridization is present. The ionic configurations are centered at 0 eV and the charge transfer configurations are centered at $\Delta = 3.0$ eV for Ti^{3+} and 3.5 eV for Ni^{2+}. Note that the colour of the lines indicates the character of the state (the scale represents the square of the coefficient c_0 from Equation 4.14 above). Blue data

Parameter	Description
κ	A scaling factor for the intra-atomic Coulomb and exchange (Slater) integrals (present also in atomic and crystal field models).
$10Dq$	The ionic crystal field splitting (present also in the crystal field model). Note this is different than the value within the crystal field model, as those values are typically inflated to partially account for hybridization effects. Depending on the point group symmetry, we can also have other parameters (Ds, Dt, etc.).
Δ	The charge transfer energy, typically defined as the energy separation between the average energies of the individual configurations.
U_{dd}	The on-site Coulomb repulsion between $3d$ electrons.
Q	The core-hole potential acting on a $3d$ electron. Sometimes referred to as U_{cd}.
V_x	The overall scaling factor for the hopping integral (hybridization strength) for hopping between electrons of symmetry x (i.e. x might be e_g, t_{2g}, b_{1g}, etc.).

Table 4.1: Parameters for the cluster model.

are states that have entirely ionic ($3d^n$) character whereas red data are states with entirely charge transfer ($3d^{n+1}\underline{L}$) character. Thus, with the hybridization set to zero, the states are pure blue and red. As the hybridization strength is increased, however, two things happen. First, the energies of the states change as the hybridization leads to an energetic repulsion between the two types of states. Second, the colours of the states change, showing that our new configuration interaction states are composed of mixtures of the states of the original configurations. Note that this mixture means we can have excitations from initial states derived from ionic states into final states derived from charge transfer states. Finally, evident from the comparison of Ti and Ni, the number of ionic and charge transfer states for different clusters can vary strongly, depending on the $3d$ electron count of the ionic configuration.

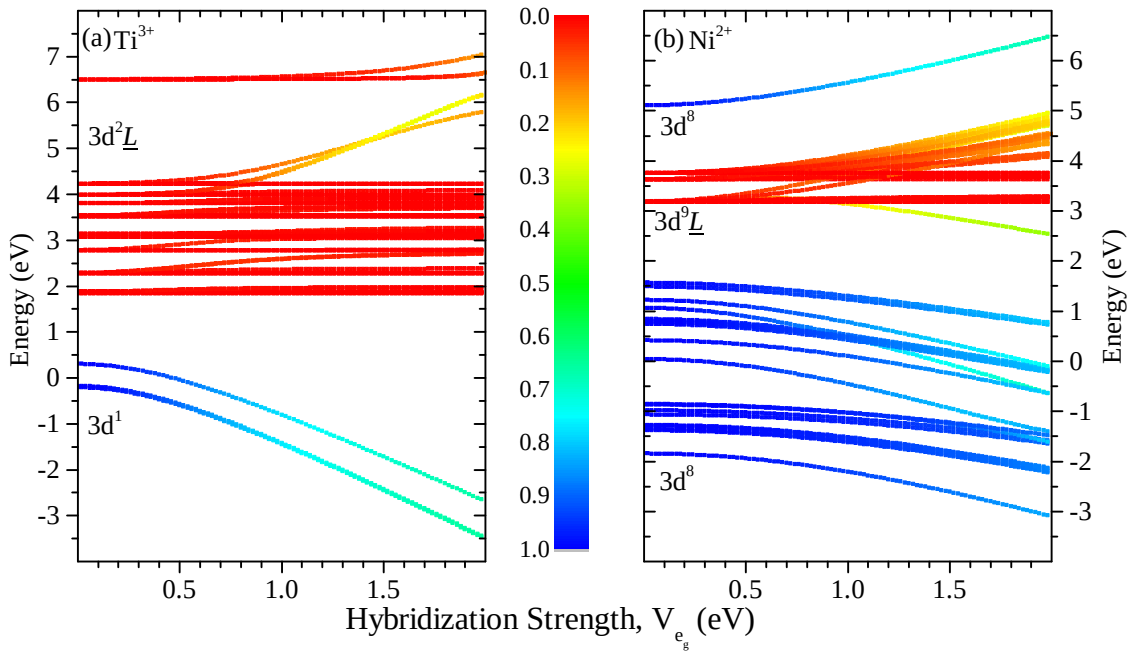

Figure 4.4: Example of hybridization in the cluster model. The energy eigenvalues are plotted for (a) a Ti^{3+} calculation and (b) a Ni^{2+} calculation. The colour of the states represents the amount of ionic ($|d^n\rangle$, blue) and charge transfer ($|d^{n+1}\underline{L}\rangle$, red) character. The hopping strength is given in terms of the e_g hopping integral, with the t_{2g} integral set to half the strength. In each case, the Slater integrals are scaled to 80% of Hartree-Fock values, spin-orbit interactions are included, and an ionic crystal field splitting of $10Dq = 0.5$ eV has been included.

4.3.4 Impurity Model

The cluster model improves upon the crystal field model as it allows us to explain charge transfer satellites in XAS spectra [54]. The cluster model is particularly useful for XPS, where charge transfer processes contribute strongly to the spectra, and some of the first applications of the model to core level spectroscopy were for XPS analysis [75]. However, in some cases the cluster model still is not quite adequate.

The main shortcoming of the cluster model is that it only considers hybridization with nearest neighbours, leading to charge transfer configurations centered at a single energy Δ. However, in a real solid, the ligand $2p$ electrons form a wide band. Thus, the fact that electrons with different energies within the band can hop to a transition metal site means that we should have a band of charge transfer configurations, rather than just the single charge transfer level in the cluster model. Including hybridization of a single transition metal atom with such a band is often called a Single Impurity Anderson Model (SIAM).

In practical implementations, the difference in moving from the cluster model to the SIAM, with respect to Figure 4.3, is that the single charge transfer configurations are replaced by multiple charge transfer configurations spread over a width related to the ligand band width and centered at Δ. Hopping integrals between the transition metal atom and each of these charge transfer configurations can then be scaled according to the shape of the ligand $2p$ DOS. Our CI matrix for this case (considering only single ligand hole configurations for simplicity) is then

$$H_{CI} = \begin{bmatrix} [H_0] & x_1 [V_{01}] & x_2 [V_{01}] & x_3 [V_{01}] \\ x_1 [V_{01}]^\dagger & [H_1] + (\Delta + \epsilon_1) [I] & 0 & 0 \\ x_2 [V_{01}]^\dagger & 0 & [H_1] + (\Delta + \epsilon_2) [I] & 0 \\ x_3 [V_{01}]^\dagger & 0 & 0 & [H_1] + (\Delta + \epsilon_3) [I] \end{bmatrix} \tag{4.20}$$

where here we have included hopping from a band discretized by three points as a simple example. Note that individual hopping integrals are scaled by x_i to account for the shape of the ligand DOS, and the individual energies of the charge transfer configurations are shifted by ϵ_i to spread them across the band. In practice we use hybridization with ~20 – 100 configurations to approximate the band shape as smoothly as possible, within computational limitations. Note that in the case of configurations with two ligand holes, each one of the n single ligand hole configurations mixes with n two ligand hole configurations, so the calculations can become very large.

Studies carried out over the past decade [52, 77–80] have found that the SIAM is necessary to properly understand charge transfer excitations in RIXS. We demonstrate this in Figure 4.5, where we compare RIXS calculations using the various models described in this chapter to an experimental NiO L_3 RIXS spectrum [52]. The parameters used for the calculations are given in Table 4.2. As discussed in the previous chapter, the RIXS spectrum here shows primarily *dd* excitations from 0 to −4 eV and primarily charge transfer excitations from −4 to −9 eV. First, we see the atomic model is capable of simulating *dd* excitations, but they do not agree with experiment because in NiO the *dd* energies are altered by the local symmetry of the Ni ions and are no longer atomic-like. The crystal field model accordingly agrees quite well with experiment, especially after an ad-hoc reduction of the Slater integrals to account for hybridization effects (the purple calculation has the reduced Slater integrals). However, no charge transfer excitations are present in the crystal field calculation, because only the ionic configuration is considered. The cluster model exhibits charge transfer excitations, and also has good agreement in the *dd* region without the ad-hoc Slater integral reduction. However, the charge transfer excitations are too localized and strong, because hopping from only one ligand energy level is used in this model. Finally, moving to the

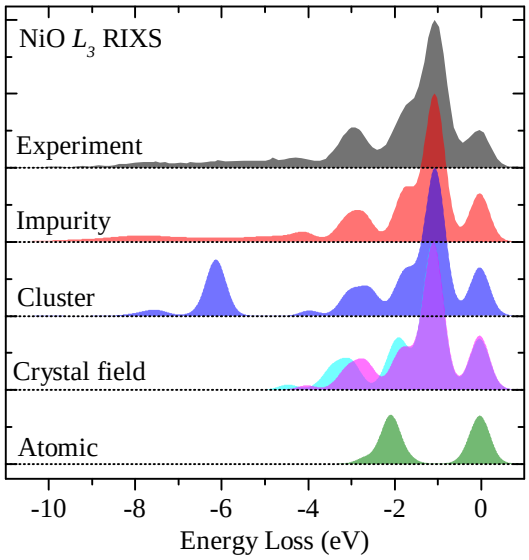

Figure 4.5: Comparison of experimental NiO L_3 RIXS with several different model calculations. Calculation parameters are given in Table 4.2.

Model	κ	$10Dq$	V_{e_g}	$V_{t_{2g}}$	Δ	U_{dd}	Q	W
Impurity	0.85	0.65	2.06	1.21	4.25	7.0	8.0	6.0
Cluster	0.85	0.65	2.06	1.21	3.00	7.0	8.0	–
Crystal Field (II)	0.65	1.05	–	–	–	–	–	–
Crystal Field (I)	0.80	1.05	–	–	–	–	–	–
Atomic	0.80	–	–	–	–	–	–	–

Table 4.2: Parameters for the NiO model calculations. κ are fractional scaling factors for Slater integrals with respect to Hartree-Fock values. W is the ligand valence band with in eV. All other parameters have units of eV and have been defined earlier. Where a parameter value is not given, it is because the respective model does not include that parameter.

SIAM (impurity) calculation, good agreement with experiment is obtained over the entire spectrum. Properly including the ligand band in the calculation leads to the wide band of CT excitations that is found in experiment. So we can conclude that for most correlated transition metal compounds, the crystal field model is adequate if we only want to study *dd* excitations, but the SIAM model is necessary to study CT excitations.

4.4 Computational Approaches

Section 4.2 introduced the expressions necessary to simulate x-ray spectra, and in Section 4.3 we described the Hamiltonians necessary for several different models. Given these two pieces of information, one then only needs to solve the Schrödinger equation to find the eigenstates (energies and wavefunctions) for the system and then insert these into the necessary expression for the spectra. More specifically, given an initial state Hamiltonian H_i, one finds the eigenvectors which are the wavefunctions $|i\rangle$ and the eigenvalues which are the energy levels E_i. The same can be done using the final state Hamiltonian H_f, and the appropriate formula can be used to simulate the spectrum.

However, in many cases when considering the more advanced model Hamiltonians, the basis sets can become quite large and it is not feasible to find the exact set of eigenstates. Thus we find that in addition to using approximate model Hamiltonians to study our systems, we need to compute approximate eigensolutions. On top of this, we often deal with matrices so large that it is not possible to store them in memory during a calculation; instead, portions of them must be generated as needed. During this thesis work, computer programs were written to perform simulations of spectra using very large impurity models, so below we will highlight some of the important features of such computations.

4.4.1 Sparse Representation

A quick look at the example impurity model Hamiltonian form given in Equation 4.20 provides an important detail about the model calculations discussed here. In general, the matrices we work with can be very sparse (i.e. a lot of the elements of the matrices are zero). If we were to increase the number of ligand band discretizations in Equation 4.20, the relative amount of zero blocks in the matrix would grow considerably. Thus, large amounts of memory can be saved by storing only the non-zero elements of the matrix. This means special routines need to be written to handle such matrices in packed storage, but the extra effort is worth it. Impurity model matrices that would otherwise require tens of GB to store in dense format can be stored with a few MB in sparse format.

An even closer look at Equation 4.20 shows us we can do even better than only storing non-zero entries. Many of the non-zero blocks are related, only being multiplied by a different scalar x_i or shifted by a different diagonal $\epsilon_i\,[I]$. Thus, we really only need to store the fundamental blocks H_0, H_1, and V_{01}, and the set of scalar values x_i, ϵ_i, and Δ. This complicates the algorithms by a significant amount, as we know need to know how to combine all of these fundamental quantities

to produce parts of the matrix when we need them in the algorithms, but it provides a tremendous saving of memory, enabling us to take on very complex problems.

4.4.2 Lanczos Algorithm

With such large matrices made possible by the sparse representation, we need powerful methods for obtaining their eigenvalues and eigenvectors. One such powerful method is known as the Lanczos algorithm [81–83], developed in 1950 by Cornelius Lanczos. Based on power methods for eigensolutions of matrices, after m iterations the Lanczos algorithm transforms an $n \times n$ matrix into a new, special basis, where the matrix becomes a tridiagonal matrix of order m. This is an enormously powerful method, as we can routinely take a matrix with $n \sim 10{,}000$ and transform it to a tridiagonal matrix with $m \sim 100$. The eigensolution of the tridiagonal matrix can then be computed very quickly. We end up with 100 eigenvalues and eigenvectors which approximate the 10,000 eigenstates of the original matrix.

During each iteration of the Lanczos algorithm, the only operation needed to be done with the Hamiltonian matrix itself is a matrix-vector multiplication. Thus, the only special routine we need for handling our sparse matrix format is one that can multiply that sparse matrix by a dense vector. This routine ends up being the bottleneck of the whole spectral calculation process, so a great deal of effort should be spent optimizing its performance.

Before describing the procedures we use for simulating spectra with the Lanczos algorithm, we will highlight one more key aspect of the algorithm. The tridiagonalization of a matrix H using the algorithm takes as input the matrix H and a starting vector, or seed vector, $|\phi_0\rangle$. For finding the ground state wavefunction of a Hamiltonian, it is often satisfactory to use a random vector as convergence to the ground state wavefunction will happen after very few iterations anyway (as we will show below in Figure 4.6). However, for final state XAS eigenvectors, or intermediate and final state RIXS vectors, we can speed things up considerably by using starting vectors that are more carefully chosen. We will provide the details of these starting vectors below.

XAS with Lanczos

As mentioned above, no matter which of the models is applied (atomic, crystal field, ligand field, impurity), an XAS calculation involves in general three matrices: H_i, T, and H_f. With this nomenclature, we can take advantage of the Lanczos technique to calculate XAS spectra as follows:

1. Construct a random vector $|\phi_0\rangle$ in the basis of H_i.

2. Use $|\phi_0\rangle$ as a starting vector for the Lanczos algorithm acting on H_i. This transforms H_i to a tridiagonal matrix in a smaller (Lanczos) basis:

$$H_{i,L} = Q_i^\dagger H_i Q_i$$

where Q_i are the Lanczos vectors for the initial state which transform the original H_i into this new basis.

3. Complete the diagonalization of $H_{i,L}$ using standard techniques for tridiagonal matrices to find the ground state $|i\rangle$.
4. Transform the transition matrix T into this new Lanczos basis as well, to get $T_{L_i} = Q_i T$
5. Use $T_{L_i}|i\rangle$ as a starting vector for the Lanczos tridiagonalization of H_f. This has the advantage of directing the Lanczos algorithm to find final states which have an appreciable overlap with $T_{L_i}|i\rangle$ and will thus be important for the XAS spectrum [65, 84].
6. Complete the diagonalization of $H_{f,L}$.
7. Transform the transition matrix into this new Lanczos basis, to get $T_{L_{if}} = Q_i T Q_f^\dagger$.
8. Compute the spectrum using Equation 4.3 and the Lanczos eigenstates.

The number of Lanczos iterations required for an accurate solution—and thus the size of the Lanczos basis constructed—varies for different situations. Typically $L_{2,3}$ XAS spectra for even very complex impurity models can be simulated using ~ 50 initial state iterations and 100 – 200 final state iterations. In Figure 4.6 we show an example calculation with several different numbers of Lanczos basis sizes. The calculation is an impurity model calculation for the $L_{2,3}$ XAS of Ni^{2+}, with parameters similar to what one might use for NiO. The actual sizes of the initial and final state bases are $n_i = 4045$ and $n_f = 2460$, respectively. First, in Figure 4.6a, we compare the full (exact) diagonalization spectrum to spectra using several different basis sizes for the initial state while using full diagonalization for the final state. We see that in this case, convergence is reached extremely quickly (note the spectrum with 16 iterations is plotted with a dashed line and overlaid with the exact solution). We can adequately represent the ground state wavefunction in a basis of size 16, while the original exact basis size is 4045. In Figure 4.6b, we now use the exact initial state wavefunction and gradually increase the number of Lanczos iterations for the final states. Here, we require more iterations because we are not simply after one wavefunction (as we were for the ground state), but instead we need a set of wavefunctions to approximate the final states for the XAS spectrum. Nonetheless, convergence is still reached quickly as we only need a basis of size 80

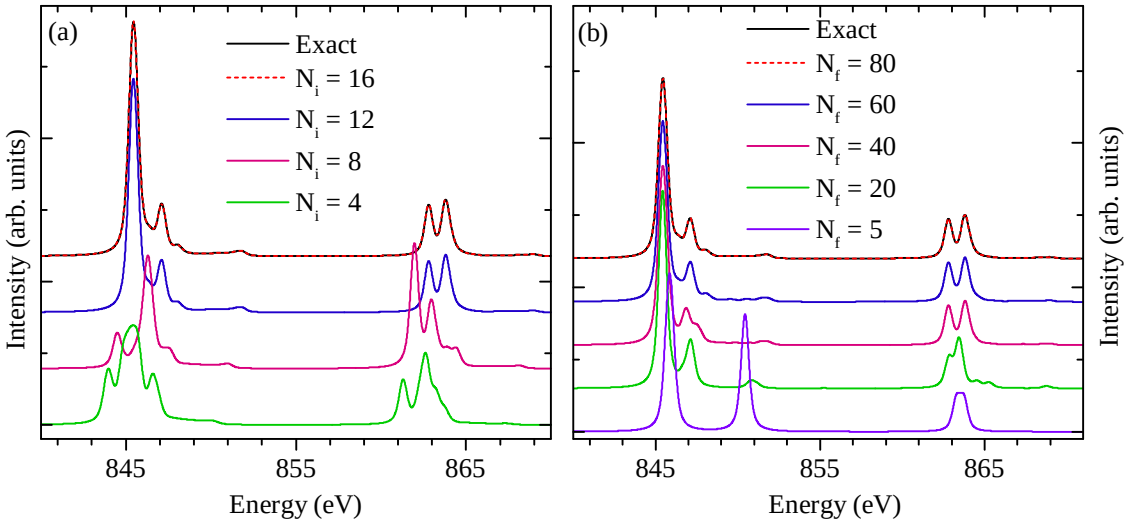

Figure 4.6: Lanczos iterations for XAS. (a) The number of initial state iterations (N_i) is increased with exact final states until convergence is reached. (b) The number of final state iterations (N_f) is increased with exact initial states until convergence is reached. The sizes of the actual full bases are $n_i = 4045$ and $n_f = 2460$.

to reproduce the exact spectrum with basis size 2460. Thus, it is clear the Lanczos algorithm is very powerful for spectral simulations using model Hamiltonians.

RIXS with Lanczos

Simulating RIXS spectra with the Lanczos Algorithm is similar to simulating XAS spectra, but there are some slight complications. Recall that the intermediate states of RIXS are the final states of XAS. Therefore, the first 8 steps for a RIXS simulation are identical to the 8 steps given above for XAS, except now steps 5 and 6 should refer to the intermediate state Hamiltonian H_n and $H_{n,L}$. It is after step 8 that the complication for RIXS comes in: we now have a set of intermediate states ($|n_i\rangle$, where i runs over the number of Lanczos iterations used for the intermediate states) which need to be considered for starting vectors for the Lanczos tridiagonalization of H_f. In other words, for each intermediate state $|n\rangle$, we have a starting vector $T^\dagger|n\rangle$, so our Lanczos algorithm needs to take as input a set of starting vectors to find the important RIXS final states.

Solving this problem of multiple starting vectors was a major accomplishment during the course of this thesis work,[4] and the result is we need to use a *block* or *band* Lanczos algorithm [83, 85] which is capable of operating on a set of starting vectors. The end result of such an algorithm is

[4]We are indebted to Dr. Maurits Haverkort for many helpful discussions on the topic of Lanczos calculations of RIXS spectra.

still a tridiagonal version of the Hamiltonian in a new, special basis, but now it converges to states having strong overlap with the set of starting vectors provided. So the rest of the steps for our RIXS simulation become:

9. Transform the decay transition matrix $T^\dagger$ according to the intermediate state Lanczos basis, $T^\dagger_{L_n} = Q_n T^\dagger$.

10. Use the set of starting vectors $T^\dagger_{L_n}|n_i\rangle$ and the band Lanczos technique to tridiagonalize the RIXS final state Hamiltonian H_f.

11. Complete the diagonalization of $H_{f,L}$ and transform $T^\dagger_{L_n}$ into this new basis to get $T^\dagger_{L_{nf}} = T^\dagger_{L_n} Q^\dagger_f$.

12. We now have all $|i\rangle$, $|n\rangle$ and $|f\rangle$ along with the corresponding eigenvalues and transition matrices, so we can simulate the RIXS using Equation 4.9.

Finally, note that in the cases where low energy initial state multiplets are present and temperature effects are important, the band Lanczos technique can be used to compute final state XAS or intermediate state RIXS eigenvectors which are important for the XAS originating from any of the relevant initial states.

4.5 Software Development

The main concepts for simulating transition metal L edge spectra as discussed in this chapter were developed by groups in the 1980s and early 1990s. Thole and collaborators [42,72] as well as Tanaka and collaborators [86] developed very powerful cluster model codes with full multiplet, crystal field, and hybridization interactions. The computational code used in this thesis is based on that of Thole *et al.*, which also is the underlying code for the popular CTM4XAS program [87]. However, during this thesis, the hybridization portion of the Thole code was rewritten and expanded, and a new interface program was developed with many useful capabilities. Below we briefly discuss the changes made to the hybridization program, and highlight some of the main aspects of the interface program.

4.5.1 Hybridization Program

The original hybridization program of Thole does in fact use the Lanczos algorithm to a certain extent. The initial states were calculated using full, exact diagonalization, while the Lanczos approach

was employed for the final states of XAS (RIXS calculations were not possible with the original code). By only using the Lanczos approach on the final states, the program was able to use an alternative approach to calculate the spectra intensities [65] that did not require transformations of the transition matrix and therefore did not require access to the Lanczos vectors (the Q vectors in the steps above). However, the full diagonalization of the initial states causes a significant slowdown for large problems, and causes large memory consumption. These issues were resolved with the version of the program rewritten completely as part of this thesis work. Some specific improvements of the new version include:

- Full Lanczos capabilities for all configurations of XAS and RIXS.
- Improved sparse representations of matrices as described above.
- Migration from FORTRAN77 to FORTRAN90 to enable dynamic memory allocation, among other things.
- Integration of the optimized BLAS and LAPACK [88] libraries for very fast matrix operations (including the diagonalizations for tridiagonal Lanczos matrices). This also allows parallel operation on multiple processors for many of the matrix operations.
- Generalized to allow any number of different configurations for CI mixing calculations.
- Generalized to allow any particular band shape for impurity model calculations.
- Calculation of RIXS scattering amplitudes so that various geometries can be simulated quickly after the time consuming diagonalization steps are done.

These various improvements to the hybridization program have enabled us to tackle very large impurity model problems. In Figure 4.7, we compare the time and memory usage of the new version of the program to the original version. As an example we use a Co^{2+} XAS impurity model calculation in O_h symmetry. To show the scaling as the problem size is increased, we gradually increase the number of single ligand hole configurations (i.e. band discretization points) used in the impurity model. Panel (a) of the Figure shows the amount of time taken for each program, while panel (b) shows the memory used. We see that we have gone from a cubic scaling in time and quadratic scaling in memory for the old code, to a linear scaling in both for the new code. For small problem sizes, the old code is actually slightly faster, because of the overhead involved in setting up the sparse matrices and performing the operations. But as the problem size increases, the new version of the code quickly begins to excel. Note that these tests were done using a single processor for each (out of necessity for the old code, and to enable direct comparison for the new code). Thus,

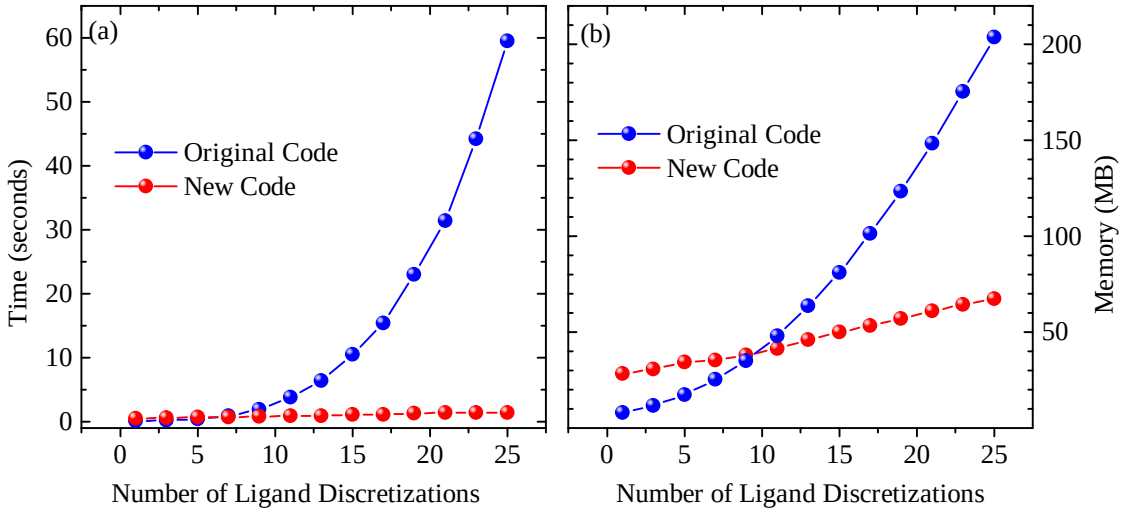

Figure 4.7: Performance of new hybridization program compared to original version. An impurity model calculation of a Co^{2+} ion in O_h symmetry is used as an example. Multiplets, crystal field splitting, spin orbit interactions, and hybridization are included, and the number of charge transfer configurations (ligand band discretizations) is scaled up to gradually increase the size of the problem. (a) The total time taken to complete the example problem. (b) The maximum memory used during the calculations.

the improvements of the new code would be magnified by taking advantage of multiple processors.

4.5.2 Interface Program

In addition to the hybridization program, which is used for cluster and impurity model calculations, we have developed an interface program capable of carrying out the atomic, crystal field, cluster, and impurity model calculations with many features and a user friendly graphical user interface. The program provides input files to the underlying computational programs and then receives back from them the dipole matrix elements or scattering amplitudes, and simulates XAS and RIXS spectra for any desired geometries. Additional Gaussian and Lorentzian broadening can be applied to spectra as well. Emphasis was put on a user friendly experience to speed up the analysis of spectra. A full description of the various features of the program interface would be too lengthy here, but below we provide some screenshots with brief descriptions.

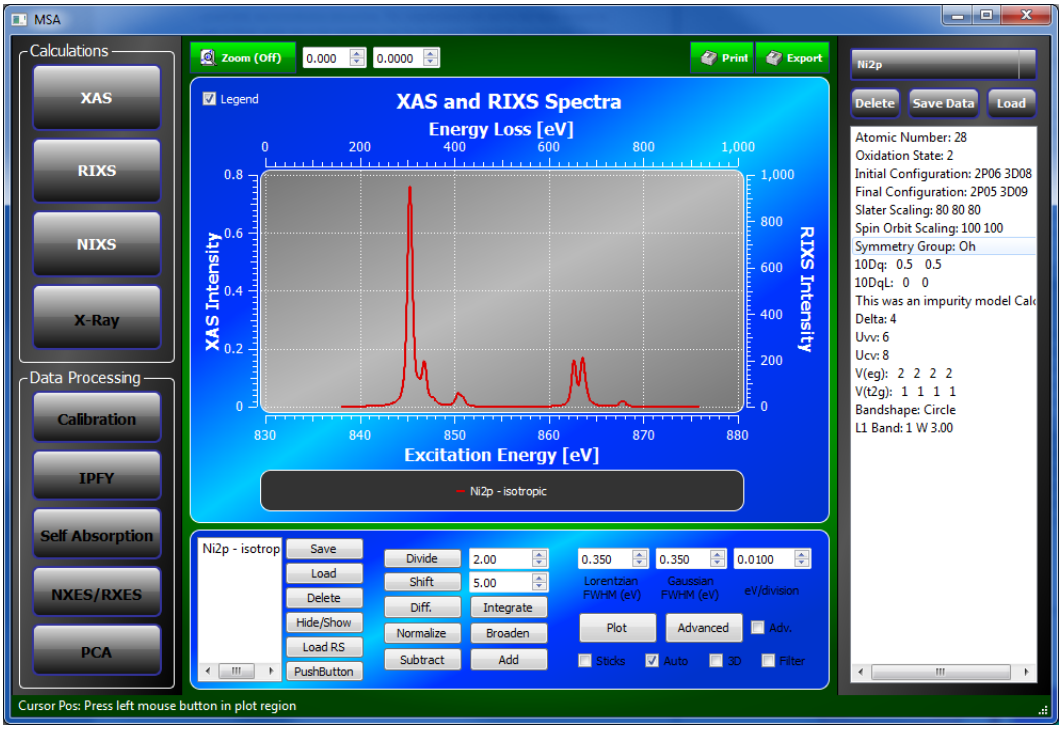

Figure 4.8: Interface software main window screenshot. The results of calculations are plotted with broadening directly in the program. Clicking the buttons on the left brings up windows for XAS (shown below in Figure 4.9), RIXS, and some other techniques not discussed here. Contact the author (Robert Green) for further details.

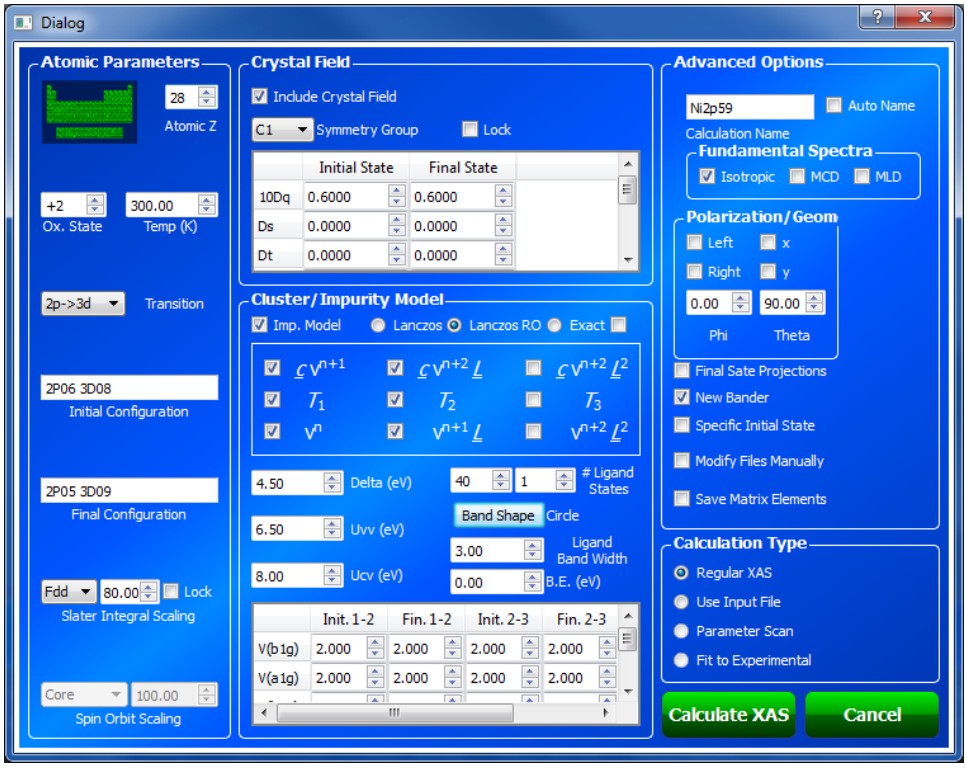

Figure 4.9: Interface software XAS window screenshot. The atomic input parameters are shown on the left. Symmetry group selection and crystal field parameters are in the upper center. Cluster and impurity model parameters are shown in the lower middle. Contact the author (Robert Green) for further details.

Chapter 5

Dilute Magnetic Semiconductors

> *Where a calculator like ENIAC today is equipped with 18,000 vacuum tubes and weighs 30 tons, computers in the future may have only 1,000 vacuum tubes and perhaps weigh only 1 ½ tons.*
>
> —Popular Mechanics (Andrew Hamilton), March 1949 [89]

As introduced in Chapter 1, the progress of electronics has been incredible over the last half century, with computer performance doubling about every two years. Such progress continues to surpass many expectations, such as the one given above. However, as we noted earlier, this trend of exponential progress will soon face some significant difficulties because the traditional approach of making transistors smaller is nearing fundamental limits. As a solution to this potential roadblock in computing improvements, spintronics [4, 5] has emerged with promising possibilities.

There are multiple research areas within the field of spintronics. For example, a very recent study has found that certain impurities in graphene actually have magnetic moments that can be switched on and off [90], which would be very useful for spin-based electronics. Topological insulators—materials discovered recently which have insulating bulks but conducting surface states—have also been suggested as candidates for spintronics applications [91]. Here, however, we are concerned with the class of materials known as Dilute Magnetic Semiconductors (DMSs), which aim to introduce spin control into conventional electronic semiconductors via the introduction of transition metal impurity atoms [5, 92, 93].

Studies of DMS materials actually date back to the 1980s where, for example, materials such as PbSnMnTe were found to exhibit low temperature ferromagnetism [94]. However, in the late 1990s and early 2000s, several developments took place that triggered an immense amount of research interest in DMS materials. First, advances in non-equilibrium sample growth techniques led Ohno and co-workers to synthesize $Ga_{1-x}Mnx$As in 1996, which showed ferromagnetic behaviour with a Curie temperature as high as 60 K for certain Mn concentrations [95]. This was a great leap over

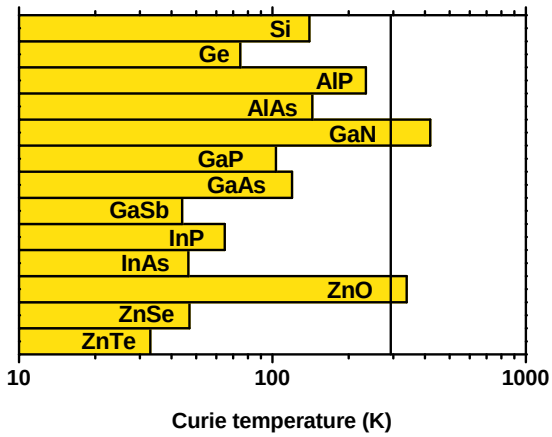

Figure 5.1: Predicted Curie temperatures of semiconductors with Mn impurities at 5% concentration. A Zener model of ferromagnetism is used for the calculations, with assumed hole doping. Figure from Ref. [96]. Reproduced with permission from the American Association for the Advancement of Science (AAAS).

previous DMSs, and hinted that perhaps it might be possible to find a DMS with a Curie transition above room temperature. Shortly after, in 2000, a theoretical work was reported that had an even larger impact on the field. Dietl and co-workers employed a Zener-based model of ferromagnetism and showed that with a 5% concentration of Mn impurities (coincident with hole doping), some semiconductors were predicted to exhibit room temperature ferromagnetism (RTFM) [96]. Their results were summarized in the now well-known plot reproduced in Figure 5.1, where the authors show predicted Curie temperatures for a range of hole-doped semiconductors with Mn-substitution. The incorporation of Mn in both ZnO and GaN was predicted to lead to T_C above room temperature, which is designated by the vertical line on the plot. This was an exciting development, and ignited a surge of experimental studies which attempted to realize this claim.

Very quickly after the prediction of Dietl *et al.*, DMSs with increasing Curie temperatures were discovered. In 2001, RTFM was actually found in $Ti_{1-x}Co_xO_2$ [97]. While the possibility of segregated, ferromagnetic Co clusters could not be ruled out entirely [93], this work nonetheless added to the growing excitement in the field. Shortly after, RTFM was found in $Zn_{1-x}Mn_xO$ [98]. While this discovery of RTFM was undoubtedly exciting, a slight problem emerged in that a previous study of seemingly crystalline $Zn_{1-x}Mn_xO$ did not find RTFM [99]. This early discrepancy of results was a sign of things to come, as in subsequent studies almost every kind of magnetic behaviour imaginable was found in $Zn_{1-x}Mn_xO$: paramagnetism [100, 101], ferrimagnetism [101], low temperature ferromagnetism [102], spinglass behaviour [99], and antiferromagnetism [103], for example.

The plethora of conflicting results in the field of DMSs expectedly led to controversy. Several possible explanations for the varied results are often considered. First, with such small quantities of magnetic atoms dilutely dispersed in a diamagnetic lattice, the measured moments are very small, so any unwanted impurities (iron filings from handling with tweezers, for example) could lead to an erroneous magnetic signal [104–106]. Further, the aggregation of metallic clusters of the impurities—too small to be detected by conventional characterization techniques such as X-Ray Diffraction (XRD)—can be the source of the magnetic signal in some cases [93]. Still more explanations include magnetism only arising from grain boundaries [107,108] or other general lattice defects [93, 109].

5.1 Determining Impurity Atom Locations From Crystal Field Excitations

As a contribution to the efforts addressing the conflicting and controversial results described above, we employed a less common, but powerful and complementary, characterization tool to study the locations and local environments of the transition metal impurity atoms in a variety of materials where different synthesis parameters led to varying magnetic behaviour. For both $Zn_{1-x}Mn_xO$ and $Ce_{1-x}Co_xO_2$, we were able to use synchrotron techniques to explain why samples with certain synthesis parameters showed ferromagnetism, while others did not. We will describe the samples and our analysis in detail below, but first we will introduce the specific approach we used to study the materials.

5.1.1 Crystal Field Excitations in RIXS

Optical spectroscopy is a technique that is closely linked to crystal field theory. By measuring absorption of photons with energies spanning the visible range, researchers are able to measure *dd* crystal field excitations and deduce information about the local bonding environment around the ions, albeit with some limitations. One of these limitations is that *dd* excitations for isolated atoms are dipole-forbidden. The reason they can be observed in practice is that if inversion symmetry around the atom is broken—by the coordination environment through T_d bonding for example, or through vibrational effects—the *d* orbitals are no longer pure and become *p*–*d* mixtures. However, the excitations nonetheless remain quite weak. A second limitation is that optical spectroscopy is not element selective, so for cases with dilute transition metal impurities (like DMSs), it can be

problematic to obtain a good measurement of the excitations of interest.

With these points considered, RIXS is an interesting alternative to optical spectroscopy for looking at *dd* excitations. As introduced in Chapters 3 and 4, RIXS allows access to the dipole-forbidden *dd* excitations through a pair of sequential dipole-allowed transitions using core-excited intermediate states. Additionally, because the dipole excitation amplitudes are well understood and can be combined using Equation 4.7 on page 37, we can fully simulate the RIXS spectral intensities. These intensities vary strongly with the resonant excitation energy, so in principle we can obtain a large amount of information by collecting *dd* spectra with different resonance energies. A crucial feature of RIXS here is the element selectivity, meaning we can preferentially excite the (often dilute) atoms of interest and obtain a spectrum dominated by the transitions local to those atoms.

Once we obtain the RIXS spectra, we can analyze them much like researchers analyze optical spectra. By applying crystal field theory [24], researchers can study the predicted *dd* energies for varying local crystal field symmetries and strengths, often by creating what are known as Tanabe-Sugano Diagrams (TSDs) [25]. These diagrams are energy level plots, like the one shown in Figure 5.2a, where we plot as an example the Mn^{2+} multiplets as a function of the cubic crystal field parameter, $10Dq$. By comparing these energy levels to experimental optical spectra, researchers can often deduce the local coordination of the ions of interest.

Using the theory developed in Chapter 4, we can calculate something analogous to a TSD, but now incorporating the *dd* intensities we would see in RIXS spectra. An example of this is shown in part (b) of Figure 5.2, where we show the same calculated multiplets as are in the TSD of panel (a), but now the colours correspond to the observed RIXS intensity when exciting with a particular resonance energy (here excitations in the L_2 XAS region was chosen). This is essentially the analysis we have applied to DMS materials; the specific coordinations of the impurity atoms introduced into the semiconductors can be determined by a crystal field analysis of the RIXS *dd* excitations.

5.1.2 Experimental Details

As introduced above, our studies for this project included two series of samples, namely $Zn_{1-x}Mn_xO$ and $Ce_{1-x}Co_xO_2$. The samples were not prepared by us during this study; instead they were obtained from collaborators skilled in synthesis. Full details of the sample synthesis and characterization can be found in Refs. [110] and [111] for $Zn_{1-x}Mn_xO$ and $Ce_{1-x}Co_xO_2$, respectively, but here we provide the details pertinent to this work.

The $Zn_{1-x}Mn_xO$ samples are thin films, prepared by molecular beam epitaxy (MBE) with x

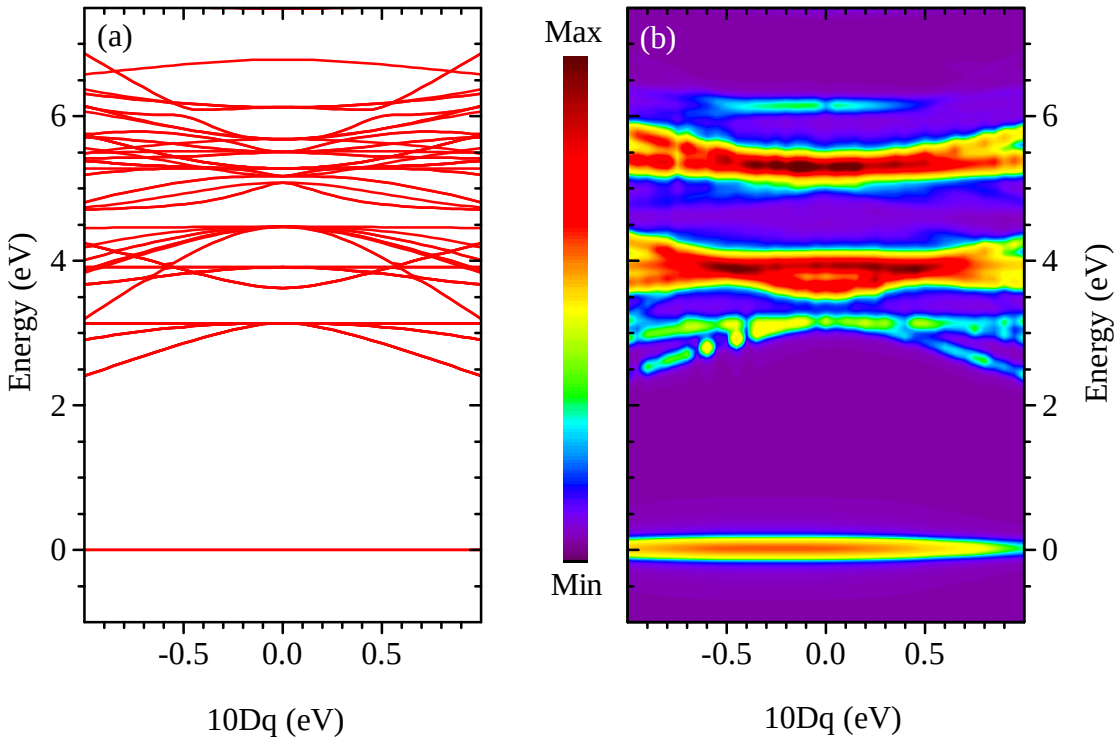

Figure 5.2: Analogy between RIXS and Tanabe-Sugano diagrams. (a) A TSD for Mn^{2+}. (b) Calculated RIXS spectra for L_2 excitation on Mn^{2+}. Both datasets were calculated from the same crystal field model, as described in Chapter 4.

varying from 0.03 to 0.33 across the series. Magnetic measurements showed ferromagnetism at low temperature ($T_C = 45$ K) for samples with low Mn concentration, and increasing antiferromagnetic contributions which eventually dominate the sample with the highest Mn concentration ($x = 0.33$).

The $Ce_{1-x}Co_xO_2$ samples with $x = 0.03$ and 0.05 were prepared by solid-state mixing. High purity precursors of $Ce_2(CO_3)_3$ and $CoCO_3$ were mixed and sintered in air at 1000 °C for 10 hours. Different samples were subjected to different variations of additional annealing, with some variations leading to magnetic behaviour. In particular, all samples were initially annealed at either a high (1000 °C, labelled as H from here forward) or low (450 °C, labelled as L) temperature. Some samples were then subjected to an additional annealing at 450 °C in a H_2/N_2 atmosphere (labelled as P from here forward). Here, three samples in total were studied: (i) a sample with 3% Co and with annealing H, (ii) a sample with 3% Co and with annealing HP, and (iii) a sample with 5% Co and with annealing LP. The sample with HP annealing exhibited RTFM, whereas the other two were paramagnetic both at room temperature and 5 K.

RIXS measurements were performed at Beamline 8 of the ALS, which was introduced in Section

3.5. For the $Zn_{1-x}Mn_xO$ samples, RIXS spectra were measured on the Mn L_2 and L_3 edges. For the $Ce_{1-x}Co_xO_2$ samples, spectra were measured at two different excitation energies at the L_3 edge.

5.1.3 Theoretical Details

As discussed above, the analysis of the RIXS spectra was carried out using the crystal field model (Section 4.3.2). The intensities were calculated using Equation 4.9 from page 37, using the same scattering geometry and polarization as experiment (given in Section 3.5). Tabulated values for intermediate state lifetime broadening (Γ_n in Equation 4.7) were used. For Mn we used FWHM values of 0.34 and 0.32 eV for the L_2 and L_3 edges, respectively, and for Co we used FWHM values of 0.43 eV for the L_3 edge [112]. The RIXS spectra were broadened with a 50 meV Lorentzian profile to account for final state lifetimes [78], and Gaussian profiles to account for instrumental resolution.

5.1.4 Results and Discussion

$Zn_{1-x}Mn_xO$

In Figure 5.3, we show RIXS spectra for two selected $Zn_{1-x}Mn_xO$ samples, with Mn concentrations (x) of 0.11 and 0.33 (referred to hereafter as 11% and 33% Mn, respectively). These two samples represent the series well, as spectra of samples with concentrations below 11% look identical to that of the 11% sample and spectra for intermediate Mn concentrations between the two presented here can be deconvoluted as a direct combination of the spectra from the 11 and 33% concentration samples. To show the chosen RIXS excitation energies, we display the XAS spectrum of the 11% sample in panel (a) of the Figure. The black arrows at 640.1 and 652.4 eV mark the excitation energies for the L_3 and L_2 RIXS, respectively. Note that the XAS spectral shape verifies that the Mn oxidation state is +2 [113], as expected from the stoichiometry.

Focusing now on the RIXS spectra displayed in Figure 5.3, we see discernible differences between the spectra for the two different samples. In general, the *dd* excitations for the higher concentration sample are more spread in energy, and have different relative intensities compared to those of the lower concentration (11%) sample. Note we also show experimental spectra from a MnO reference sample, which are very similar to the spectra for the high concentration (33%) case.

To understand the changes in the spectra between different samples, we can calculate RIXS maps for varying local crystal fields, using the analogy to TSDs that was introduced above. RIXS intensity

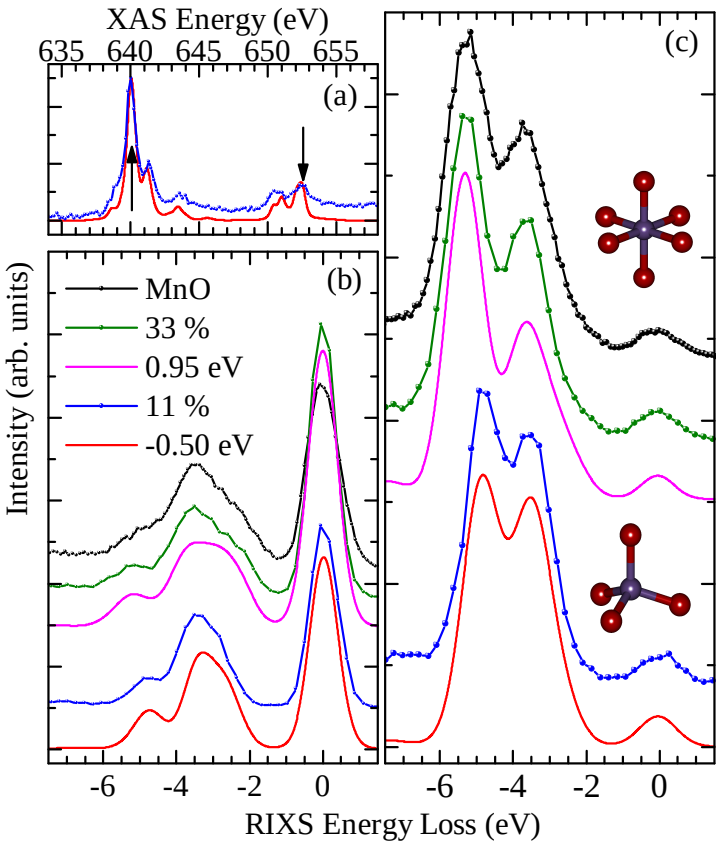

Figure 5.3: RIXS spectra for $Zn_{1-x}Mn_xO$. (a) Experimental and calculated $L_{2,3}$ XAS spectra to show the RIXS excitation energies. (b) Experimental and calculated L_3 RIXS spectra. (c) Experimental and calculated L_2 RIXS spectra. The legend applies to all panels. Experimental spectra are plotted with dotted lines, while calculated spectra use smooth lines. The experimental spectra are labelled with Mn concentration percentages, while calculated spectra are labelled with the value of the empirical crystal field splitting parameter, $10Dq$.

maps for the L_3 and L_2 excitation are shown in Figure 5.4 in panels (a) and (b) respectively. Reduced broadening compared to experiment is used for clarity. Indeed, strong changes in the spectra are observed for a varying crystal field parameter, $10Dq$. For both the L_3 and L_2 edge, we find the best agreement with experiment using $10Dq$ values of 0.95 eV for the high Mn concentration case and -0.50 eV for the low concentration case (marked by the dashed lines on the plots). Recall from Section 4.3.2 that here a positive $10Dq$ value indicates six-fold O_h coordination, while a negative value indicates four-fold T_d or eight-fold cubic coordination.

Figure 5.3 shows the best fit calculations, using the $10Dq$ values mentioned above, and with Slater integral factors as shown in Table 5.1. One can see the agreement with experiment is quite good, and the changes between the two materials are captured nicely by the changing crystal fields. Below we interpret what these results tell us.

First, considering the high concentration case, we see the O_h simulation agrees well both with the $Zn_{0.67}Mn_{0.33}O$ sample and the MnO reference. The $10Dq$ value of 0.95 eV also agrees well with values obtained previously for MnO using a similar model [78]. Thus, we have found that in this 33% concentration case, the Mn ions are located in O_h environments very similar to MnO. This is perhaps not surprising, as 33% impurity concentration is quite a high value, and could understandably lead to segregated phases of material. Here, we likely have inclusions very similar in structure to MnO forming due to the over-abundance of Mn ions.

For the low Mn concentration case, the agreement is very good with the -0.50 eV value for $10Dq$. As mentioned, this negative $10Dq$ value can be indicative of either tetrahedral bonding or eight-fold cubic coordination. We can differentiate between the two by the overall magnitude of $10Dq$. From the point charge derivation of crystal field splittings, it is found that for similar cations and anions with similar bond lengths, tetrahedral $10Dq$ values should have a magnitude of 4/9 that of O_h coordination, while for cubic coordination they should be 8/9 of O_h [24]. Thus, our value of -0.50 eV is quite close to what we should expect for T_d coordination in comparison to the strength of 0.95 eV obtained for the O_h case. That the magnitude of $10Dq$ is slightly larger than the 4/9 rule predicts can be explained by the shorter bond lengths in ZnO (1.98 Å average) versus octahedrally coordinated MnO (2.21 Å average) [115]. Thus, knowing that the Zn sites in the ZnO lattice have approximately T_d coordination, we see that we have successful substitution of Mn into these Zn sites for the low concentration case.

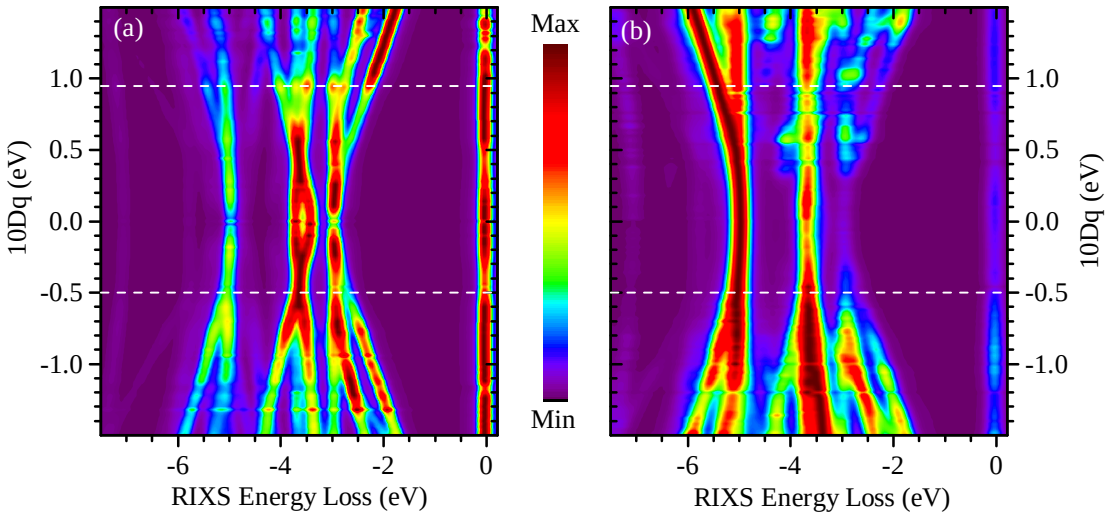

Figure 5.4: Calculated Mn^{2+} RIXS intensity for varying crystal field strength, using the crystal field model as described in Chapter 4. (a) and (b) show spectra for the L_3 and L_2 excitation energies labelled in Figure 5.3a, respectively. Figure adapted from Ref. [114].

Ion	Coordination	$10Dq$ (eV)	κ
Mn^{2+}	octahedral	0.95	0.75
Mn^{2+}	tetrahedral	-0.50	0.72
Co^{2+}	cubic	-0.60	0.75

Table 5.1: Crystal field calculation parameters for the DMS materials. κ is the scaling of the Slater integrals, given as a fractional amount of the Hartree-Fock values [9].

These results help us to understand the differing magnetic behaviour for the low- and high-concentration cases. For low Mn concentration, we find that the Mn ions successfully substitute into the Zn sites, and we do in fact obtain ferromagnetic behaviour, although only at low temperatures (under 45 K as stated earlier). However, for high Mn concentration, phase segregation occurs and we have MnO-like inclusions. Recalling that MnO is antiferromagnetic at low temperatures, we can then understand why increasing the concentration too much reduces the ferromagnetism and causes a change to antiferromagnetism. Here we can reiterate the importance of RIXS being an element selective local probe—if the MnO clusters appeared at lower concentration, and were very small in size, conventional characterization techniques like XRD might not be able to detect them. However with RIXS, we are guaranteed to measure properties specific to the Mn as long as it is present in the sample.

$\mathbf{Ce_{1-x}Co_xO_2}$

We can perform a very similar analysis for the $Ce_{1-x}Co_xO_2$ samples. In panel (a) of Figure 5.5, we show measured and calculated Co L_3 XAS spectra to denote the RIXS excitation energies, marked A and B. The rest of the panels in the Figure contain RIXS spectra, with those for excitation energy A in the upper portion, and those for excitation energy B in the lower portion. The Figure is arranged so that panel (b) shows the RIXS spectra for the two paramagnetic samples (3% H and 5% LP) while panel (c) shows the spectra for the ferromagnetic sample (3% HP). Comparing the experimental spectra—the red and black spectra in (b) and the magenta spectra in (c)—we see that the paramagnetic samples have spectra which are very similar to each other, while the ferromagnetic sample has spectra which are quite different from them. In particular, the spectra for the ferromagnetic sample have more weight in the -5 to -2 eV region compared to those of the paramagnetic samples.

Similar to the $Zn_{1-x}Mn_xO$ case described above, in Figure 5.5d we show calculated RIXS maps

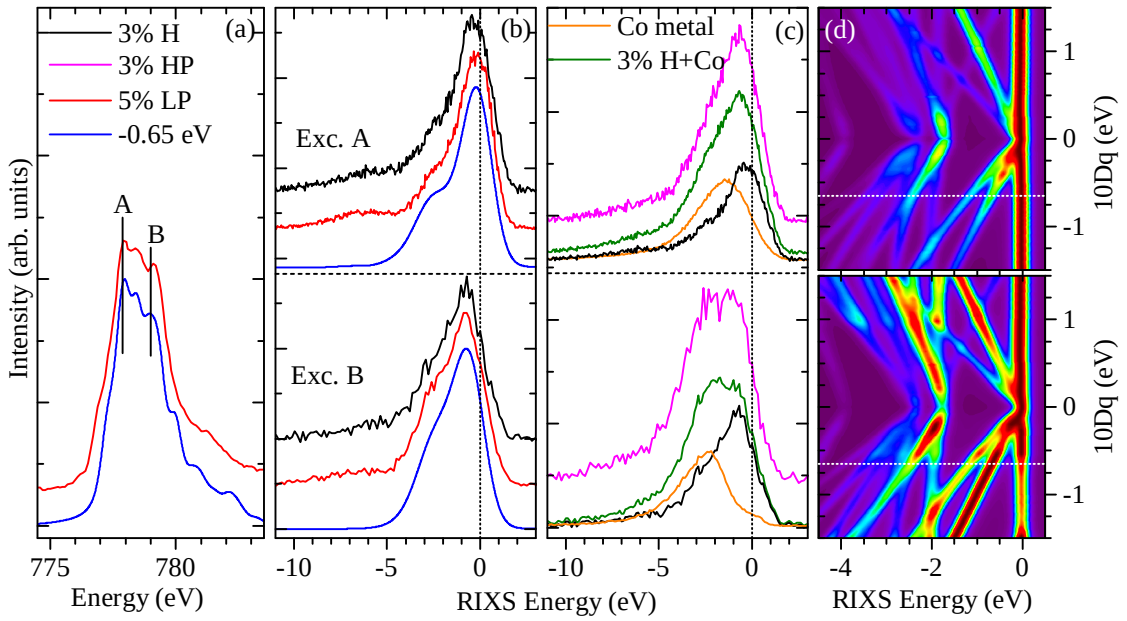

Figure 5.5: Experimental and calculated XAS and RIXS spectra for $Ce_{1-x}Co_xO_2$. Legends refer to Co concentrations and annealing procedures for experimental data, and the value of the empirical crystal field parameter, $10Dq$ for the calculated spectra. (a) Experimental Co L_3 XAS spectrum (red) indicating the RIXS excitation energies, along with a calculated spectrum (blue) for comparison. (b) Co L_3 RIXS spectra for paramagnetic samples excited at energy A (upper panel) and energy B (lower panel). Calculated spectra are shown in blue. (c) RIXS spectra for ferromagnetic sample (3% HP) excited at excitation energy A (upper) and B (lower). (d) Calculated RIXS spectra for varying crystal field strength. Upper panel for excitation energy A, lower for excitation energy B. Figure is adapted from Ref. [114].

for excitation energies A and B using varying crystal field strengths. Again we see a very strong dependence of the RIXS excitations on the crystal field. From these maps we can deduce that the spectra of the paramagnetic samples can be reproduced very well using calculations with a crystal field of $10Dq = -0.65$ eV. These spectra are marked by the dashed white lines in the contour plots, and are plotted in blue in panel (b). We can see the agreement with the experimental spectra is quite good at both excitation energies. This result tells us that for these samples, the Co ions substitute into the Ce sites in the lattice. The Ce sites have eight-fold cubic coordination, consistent with the negative $10Dq$ value obtained. Note that a negative $10Dq$ could also suggest tetrahedral coordination, but we can rule this out for multiple reasons. First, the CeO_2 lattice is cubic, so it makes more sense to see the Co ions in cubic rather than tetrahedral coordination. Second, we can consider the magnitude of the $10Dq$ value, much like we did for $Zn_{1-x}Mn_xO$. Octahedrally coordinated CoO has a $10Dq$ value in the range of 0.8–1.0 eV [69,116]. Recall for cubic coordination with the same atoms and bond lengths, we expect a $10Dq$ magnitude roughly 8/9 times as large

as this. Our value (-0.65 eV) is slightly smaller than one might first expect, but the CeO_2 bond lengths are longer than CoO (2.34 Å versus 2.13 Å [115]), so a slightly smaller $10Dq$ value should be expected for Co substitution in CeO_2.

The RIXS spectra of the ferromagnetic (3% HP) sample cannot be reproduced by contributions from a single site (either via calculations or comparison to existing experimental spectra). However, the extra spectral weight at higher energy loss can be identified as a contribution from metallic Co. In panel (c) we show scaled spectra of a metallic Co reference and the paramagnetic 3% H sample, in orange and black respectively. In green we show the summation of these spectra which agrees very well with the spectra of the ferromagnetic sample. Note that Co metal does not exhibit constant energy loss RIXS excitations like the correlated materials do; instead its spectra can be more aptly described as fluorescence which remains at a fixed absolute emission energy. This helps to explain the shift of spectral weight to higher energy loss for the ferromagnetic sample as we go from excitation energy A to excitation energy B (i.e. moving the incident energy further above the L_3 fluorescence line of Co).

The results obtained from the RIXS can explain the magnetic behaviour of the samples in a very natural way. First, we see for substitution of the Co atoms into the Ce sites we observe only paramagnetic behaviour. However, after additional post-annealing, metallic Co forms (likely in small clusters) which gives rise to a ferromagnetic signal simply because Co is a ferromagnet. Note that this result is in agreement with the magnetic measurements performed by our collaborators, where zero-field-cooled and field-cooled measurements suggested the presence of Co nanoparticles as well [111].

5.1.5 Conclusions

We have shown that RIXS can be a very successful technique for determining the locations of transition metal impurity atoms in dilute magnetic semiconductors, allowing a subsequent understanding of the magnetic behaviour. For the case of $Zn_{1-x}Mn_xO$, we found using RIXS that substitution of Mn into Zn sites occurs and leads to low temperature ferromagnetism for concentrations $\leq 11\%$, whereas MnO-like clusters form at higher Mn concentrations and quench the ferromagnetism. For $Ce_{1-x}Co_xO_2$, we found that certain post-annealing procedures can induce RTFM, but that this RTFM is due to an unwanted clustering of Co atoms into ferromagnetic metallic inclusions. Pure substitution, on the other hand, leads to only paramagnetism. The material-specific results should be a great benefit to the research community, as should the demonstration that RIXS can be a

powerful tool to use in this field.

5.1.6 Contributions

The work has been published in two manuscripts. The first is comparable to the discussion above, focusing largely on the RIXS technique:

> R. J. Green, G. S. Chang, X. Y. Zhang, A. Dinia, E. Z. Kurmaev, and A. Moewes. Identifying local dopant structures and their impact on the magnetic properties of spintronic materials. *Phys. Rev. B*, **83**:115207, 2011.

The authors contributed as follows:

- R. J. Green collected some of the synchrotron data, performed the analysis of the RIXS data, carried out the crystal field RIXS calculations, and wrote the manuscript, with input from all co-authors.
- G. S. Chang collected some of the synchrotron data.
- X. Y. Zhang and A. Dinia prepared the samples and performed initial characterization experiments.
- E. Z. Kurmaev and A. Moewes supervised the project and assisted with the manuscript preparation.

The second manuscript focuses on the synthesis, magnetic measurements, RIXS, and other spectroscopic studies of the $Ce_{1-x}Co_xO_2$ samples:

> A. Bouaine, R. J. Green, S. Colis, P. Bazylewski, G. S. Chang, A. Moewes, E. Z. Kurmaev, and A. Dinia. Appearance of ferromagnetism in Co-doped CeO_2 diluted magnetic semiconductors prepared by solid state reaction. *J. Phys. Chem. C*, **115**(5):1556-1560, 2011.

The authors contributed as follows:

- R. J. Green performed the analysis of the RIXS data, carried out the crystal field RIXS calculations, wrote most of the spectroscopy portion of the manuscript, and collected part of the synchrotron data.
- G. S. Chang and P. Bazylewski collected part of the synchrotron data.
- A. Bouaine, S. Colis, and A. Dinia prepared the samples and performed initial characterization experiments.
- E. Z. Kurmaev, A. Dinia, and A. Moewes supervised the project and assisted with the manuscript preparation.

5.2 Understanding the Ferromagnetism in $(In_{1-x}Fe_x)_2O_3$

The studies of $Zn_{1-x}Mn_xO$ and $Ce_{1-x}Co_xO_2$ in the previous section were very successful at correlating the locations of impurity atoms to the observed magnetic properties. However, in the case of substitution of impurity atoms into lattice cation sites (Mn into Zn sites and Co into Ce sites), we did not venture to suggest why the $Zn_{1-x}Mn_xO$ case showed low temperature ferromagnetism and why the $Ce_{1-x}Co_xO_2$ case only showed paramagnetic behaviour. These questions were beyond the scope of the previous project and require more advanced theory or different measurements directed at the magnetic mechanisms themselves.

In this section, however, we describe our study of $(In_{1-x}Fe_x)_2O_3$, where our spectroscopy methods not only revealed the impurity Fe locations, but also allowed us to draw important conclusions on the magnetic mechanisms. In particular, we found, using a unique quantitative XAS experiment, that the magnetism in this material arises due to Fe atoms which are directly adjacent to oxygen vacancy sites in the In_2O_3 lattice. Such a result has been predicted theoretically, and suggested from indirect experimental evidence, but our results provide a clear indication that this is in fact the case.

5.2.1 Experimental

The $(In_{1-x}Fe_x)_2O_3$ samples studied in this work were prepared by collaborators at Shanxi Normal University in Linfen, China. They are thin films prepared by pulsed laser deposition on Al_2O_3 substrates, with $x = 0.02$, 0.05, and 0.20. To promote the formation of oxygen vacancies—suspected to be linked to magnetic properties—the samples were synthesized in oxygen-deficient environments: the $x = 0.02$ sample was prepared in an oxygen partial pressure of 0.1 mTorr, while the others were prepared under 5×10^{-3} mTorr.

Earlier characterization studies on the samples used XRD to show no detectable metallic or oxide segregated phases or clusters were present [117]. The XRD also revealed a slight decrease in the lattice constant compared to pure In_2O_3, understandable via Fe ions substituting for the larger In ions in the lattice and from the presence of oxygen vacancies (V_O). All of the samples showed a metallic conduction due to the V_O impurity band, and all exhibited RTFM with varied saturation magnetizations, with the moment per Fe atom decreasing as Fe concentration increased [118].

The specific structure of the samples enabled us to use a unique approach for obtaining XAS spectra. The $(In_{1-x}Fe_x)_2O_3$ films were thin enough that incident x-rays were able to penetrate

through to the Al_2O_3 substrates. This lead to X-ray Excited Optical Luminescence (XEOL) within the substrates that was detectable using an optical spectrometer. By detecting the intensity of a strong Al_2O_3 luminescence line as we scanned the incident photons across the Fe $L_{2,3}$ edges, transmission XAS spectra were obtained for the films. This approach allowed us to perform a more quantitative XAS study than usual, as we will describe below. These Fe $L_{2,3}$ spectra were calibrated by setting the L_3 maximum of a Fe_2O_3 reference sample to 709.6 eV.

Oxygen K edge XAS spectra were recorded using TFY mode at the SGM beamline, while the XES spectra were recorded at Beamline 8.0.1 using the scattering geometry given in Section 3.5. For each sample, a set of resonant XES (RXES) spectra was recorded, where the incident energy was tuned across the XAS onset. The XAS and XES were calibrated using a well-characterized bismuth germanate (BGO) sample. The first XAS peak of the BGO was calibrated to 532.7 eV, while the XES maximum was calibrated to 526.4 eV.

5.2.2 Theory

To interpret the Fe $L_{2,3}$ XAS spectra, we employed the ligand field (cluster) model, as described in Chapter 4. For the unique local symmetries present in this material, we utilized a code which expands the electrostatic potential of a point charge distribution onto spherical harmonics [74], allowing us to determine the crystal field parameters in a more direct manner than usual. As usual, the simulated spectra were broadened using Lortenzian and Gaussian profiles to account for lifetime and experimental broadening, respectively.

5.2.3 Results and Discussion

Fe $L_{2,3}$ Edge Results

The raw Fe $L_{2,3}$ XAS spectra are shown in Figure 5.6a. As mentioned above, these spectra were acquired using a unique technique that is depicted in Figure 5.6d. Here, the incident x-rays are able to penetrate completely through the $(In_{1-x}Fe_x)_2O_3$ films, leading to XEOL from the Al_2O_3 substrates. The intensity of the strong Al_2O_3 luminescence line at 689 nm was detected as the incident energy was scanned across the Fe edge. The Fe absorption led to dips in the luminescence intensity, also depicted in panel (d), which provided a transmission-detected XAS signal. The advantages of this approach is that the transmission XAS is a uniform measurement which probes the entire depth of the film, and it can be used as a quantitative XAS measurement.

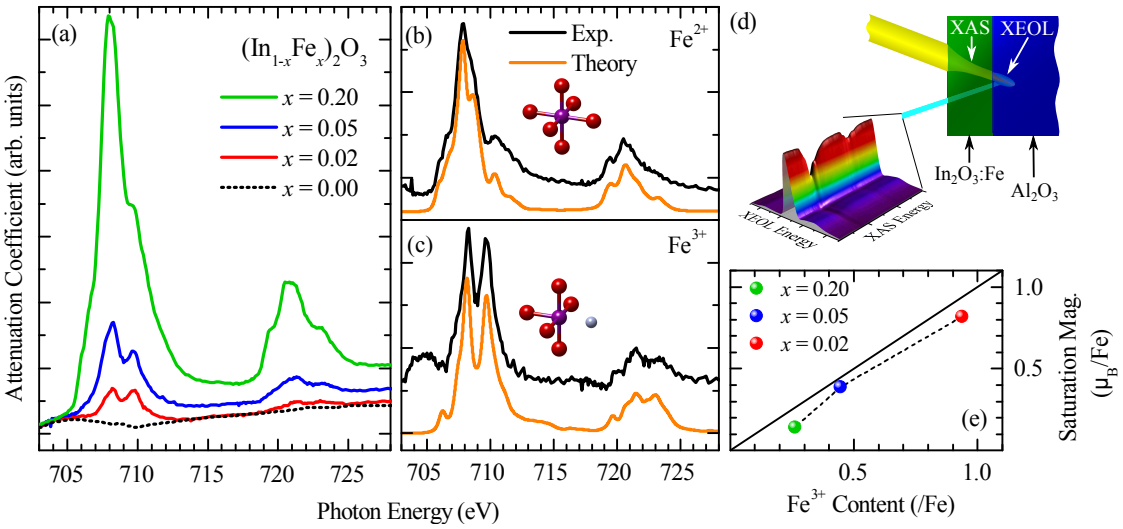

Figure 5.6: XAS results for $(In_{1-x}Fe_x)_2O_3$. (a) Raw experimental Fe $L_{2,3}$ XAS spectra. (b-c) Derived component spectra (black) with corresponding calculated spectra (orange). The structures depict the symmetries used in the calculations. (d) Schematic of the experimental technique. (e) Magnetic moments compared to relative Fe^{3+} concentration.

In panel (a) of Figure 5.6, we have plotted the spectra after normalizing the transmission signal to the In M_2 edge, which is a weak, gradually varying edge located primarily lower in energy than the Fe $L_{2,3}$ edge. The pure In edge can be seen for the $x = 0.00$ sample, plotted with the dashed line in the Figure. Since these are transmission spectra, normalizing them to the In edge means that the intensities of the Fe spectra provide us with quantitative information: the spectral areas are related directly to the number of Fe atoms. This is important for our later analysis.

From the XAS spectra shown in panel (a), we can see strong variations between samples. For the $x = 0.20$ sample, the spectrum looks very similar to that of FeO [119], demonstrating a significant proportion of octahedrally-coordinated Fe^{2+} atoms. As the Fe concentration decreases, however, a second peak just below 710 eV becomes more prominent, suggesting an increasing relative concentration of Fe^{3+} atoms. Interestingly though, for $x = 0.02$, where the second peak is strongest, the spectrum still does not resemble that of the Fe^{3+} oxide, Fe_2O_3 [119], or any other common Fe^{3+} compounds [54].

To extract the specific contributions making up the raw spectra, we have used the spectral differences technique. Note that because we have used transmission XAS, we need not worry about surface effects or self absorption, and our experimental spectra are accordingly pure linear combinations of the component spectra which are leading to the varying shapes. The experimental spectra can be reproduced exactly using the two component spectra shown in black in panels (b)

and (c) in Figure 5.6. As noted, the Fe^{2+} component which dominates the $x = 0.20$ sample is very similar to that of FeO. However, the Fe^{3+} spectrum is quite unique, showing a two peak structure in the L_3 region. Note that for the Fe^{3+} component spectrum, there is a small residual amount of the In M_2 peak present at 704 eV.

By fitting the optimal ratios of each component to reproduce each raw spectrum, we are able to extract the relative amounts of Fe^{2+} and Fe^{3+} in each sample. This is determined by finding the integrated intensity under the scaled component spectra, and adjusting each by the number of holes available for the XAS process (4 for the Fe^{2+} $3d^6$ configuration and 5 for the Fe^{3+} $3d^5$ configuration). For each sample, the relative amount of Fe^{3+} (normalized to the total amount of Fe) is plotted along the horizontal axis of Figure 5.6e. Along the vertical axis we have plotted the measured saturation magnetizations for each sample, also relative to the total Fe content. Here, we uncover a direct link between the number of Fe^{3+} atoms and the saturation magnetization, showing that it is almost certainly the Fe^{3+} atoms alone which contribute to the ferromagnetism of these samples.

Next, we can use the specific shape of the Fe^{3+} spectrum to determine where the atoms are in the host lattice and how they are interacting with the lattice to yield the magnetic behaviour. As noted above, the spectrum is quite different from that of Fe_2O_3, which suggests we do not have simple substitution of the Fe atoms into the octahedral In sites in the lattice. However, recalling that the samples were synthesized to contain oxygen vacancies V_O, and noting that some studies have suggested the importance of Fe atoms adjacent to V_O for magnetic properties in both $(In_{1-x}Fe_x)_2O_3$ [120] and other DMSs [120, 121], we can perform calculations to determine what spectra we should expect for adjacent Fe^{3+}–V_O complexes. To determine the crystal field symmetry for such a case, we performed a multipole expansion of the potential [74] for an octahedron of point charges missing a single x axis ligand charge, which roughly approximated a V_O. This provided relative magnitudes for the crystal field parameters within D_{2h} symmetry, and we left as a single tunable parameter the overall scaling of these parameters. Note that an actual electrostatic expansion using point charges is known to not generally provide appropriate magnitudes for crystal field parameters, but it is nonetheless useful for determining the relative sizes of different parameters through the symmetry of the field.

After adjusting the overall magnitude of the parameters to best fit the experimental data, we end up with the calculated spectrum shown in Figure 5.6c, using the inputs shown in Table 5.2. We see the agreement with experiment is very good—the assumption of an Fe^{3+}–V_O complex provides

Species	10Dq/Ds/Dt/Du/Dv	Hopping, V	Δ	U_{dd} - Q
Fe^{2+}	0.70/-0.05/0/0/0	2.0/2.0/1.0/1.0	6.0	-2.0
Fe^{3+}	1.20/-0.26/-0.02/0.70/-0.52	1.7/2.0/1.0/0.9	2.0	-2.0

Table 5.2: Cluster model calculation parameters for $(In_{1-x}Fe_x)_2O_3$ spectra. All values have units of eV. Hopping integral symmetries are $b_{1g}/a_{1g}/b_{2g}/e_g$.

the interesting two-peaked L_3 region and the overall proper shape of the L_2 region. Thus, not only can we determine it is the Fe^{3+} sites which drive the ferromagnetism, but we also see that these special sites are located next to oxygen vacancies in the In_2O_3 lattice.

For the Fe^{2+} component spectrum, we verified the earlier conclusion that it was attributable to Fe ions in the octahedral In sites of the lattice. The calculated spectrum is shown in Figure 5.6b, and the parameters are given in Table 5.2. The agreement with experiment is good, and the parameters are what one would expect for the Jahn-Teller-active case of Fe^{2+} in an octahedral environment [122].

O K Edge Results

Our Fe L edge results showed that the Fe^{3+} atoms interact strongly with the V_O in the samples to induce the ferromagnetism. This agrees with earlier theoretical predictions, which suggested that the interaction between $3d$ states and a V_O impurity band could lead to ferromagnetism [123]. Other studies used DFT to show theoretically that an energetically stable, ferromagnetic configuration can be present in $(In_{1-x}Fe_x)_2O_3$ with Fe atoms adjacent to V_O [120]. We can investigate the near gap DOS, and thus the interaction of the Fe $3d$ states with those of the impurity band, using oxygen K edge XAS and XES.

The oxygen K edge XAS and NXES for the samples are shown in Figure 5.7a. The general shapes of the spectra are similar to those of pure In_2O_3 [124], confirming that the introduction of Fe does not induce large changes on the electronic structure. However, in the pre-edge region of the XAS (529 – 532 eV), we see observable changes in the spectra which indeed correlate to the Fe concentration. In particular, there is increasing spectral weight in this region as the Fe concentration is increased. Note that it is this region which we expect to be sensitive to hybridization between the O $2p$ states and both the Fe $3d$ states and the impurity band states.

Next, we note that the introduction of the Fe states into the bottom of the conduction band and their interaction with the V_O impurity states leads to a considerable band gap narrowing in

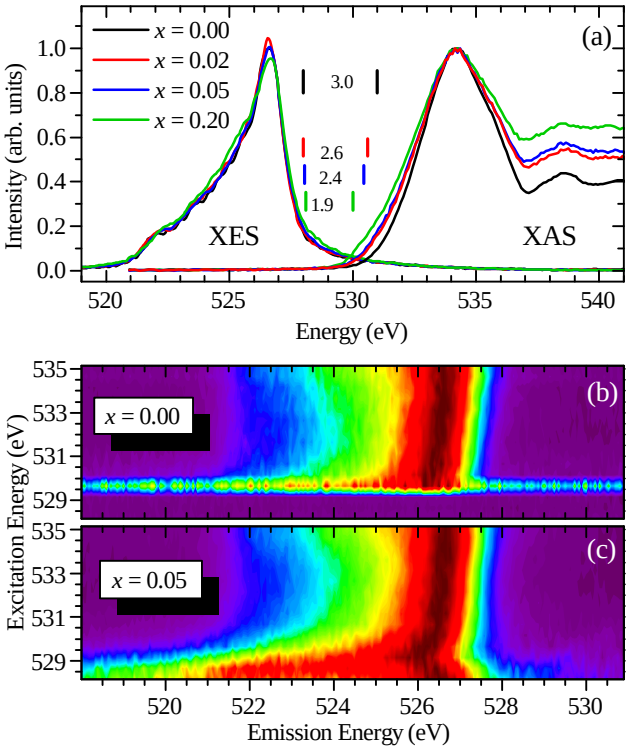

Figure 5.7: Experimental oxygen K edge results for $(In_{1-x}Fe_x)_2O_3$. (a) The XAS and NXES spectra, showing the states in the near gap region. (b) and (c) Resonant XES spectra for the pure and 5% concentration samples.

the Fe-substituted samples, compared to pure In_2O_3. In Figure 5.7a, we have marked the band edges determined using the second derivative technique [44], and have indicated the corresponding measured band gaps. We see the band gap decreases from the known value of ~3.0 eV for pure In_2O_3 [125] down to 1.9 eV for the 20% concentration sample. Such a range of tenability means $(In_{1-x}Fe_x)_2O_3$ might be useful for other applications like photo-catalysis, in addition to the spintronics focus we have here.

While the NXES spectra for all samples are quite similar, differences were enhanced by collecting resonantly-excited XES (RXES) spectra for excitation energies spanning the Fe-sensitive range from ~528.5 – 535 eV. Spectra for the pure and 5% Fe concentration samples are shown in panels (b) and (c) of Figure 5.7, respectively. The individual spectra (which make up horizontal slices in the colour plots) have been normalized for clarity. First, for the In_2O_3 sample, we see that as the excitation energy decreases, so too does the highest energy of the emission spectrum. This type of behaviour is indicative of an indirect band gap. Because RXES is a momentum-conserving process, decreasing the excitation energy down to the conduction band minimum can be used to test for a direct or

indirect band gap [126]. Interestingly, the band gap of In_2O_3 has been somewhat controversial in the past, particularly regarding its magnitude and whether it is direct or not. Here we see that it is indeed indirect, although with a very small valence band dispersion. Finally, note that for excitation energies below 529.5 eV, the spectra disappear as there are no longer unoccupied states to excite into; i.e. we are below the conduction band minimum.

For the RXES spectra for the Fe-substituted sample, we see quite a different behaviour. While we have the same slight dispersion between 530 and 535 eV excitation energy, the spectra do not cut off below 529.5 eV as they did for the In_2O_3 sample. Instead, we have a sharp dispersion, and at the lowest excitation energy, the maximum of the emission spectrum moves back up in energy. This behaviour is due to the presence of the Fe $3d$ and V_O states, which provide new partially filled states at the bottom of the conduction band to excite into. The abrupt shift of the emission spectral weight back up to near the valence band maximum indicates the impurity states are quite localized at the bottom of the conduction band, and that they show a different momentum dependence than the In_2O_3 states. Thus, we have a clear demonstration of the presence of the impurity states at the bottom of the conduction band, which are responsible for mediating the ferromagnetism, in line with theoretical models laid out earlier [123].

5.2.4 Conclusions

We have studied $(In_{1-x}Fe_x)_2O_3$ using a variety of spectroscopic techniques. Using Fe L edge XAS and cluster model calculations, we have shown that the room temperature ferromagnetism in these samples is linked to the presence of Fe^{3+} ions which are directly adjacent to oxygen vacancies in the In_2O_3 lattice, in agreement with recently proposed mechanisms for mediating the ferromagnetism in dilute magnetic semiconductors. Using oxygen K edge spectroscopy, we revealed the presence of Fe $3d$ states in the region of the V_O donor impurity band, found a strong and useful band gap narrowing upon the introduction of Fe, and presented a clear measurement of the indirect nature of the band gap in In_2O_3.

5.2.5 Contributions

A manuscript has been prepared based on the work presented in this section and is near the submission stage:

> R. J. Green, T. Z. Regier, X. H. Xu, G. S. Chang, E. Z. Kurmaev, and A. Moewes. Room temperature ferromagnetism driven by adjacent dopant-vacancy interactions in dilute magnetic oxide $(In_{1-x}Fe_x)_2O_3$. To be submitted for publication, 2013.

The authors contributed as follows:

- R. J. Green performed the experimental XAS and XES measurements, performed the cluster model calculations, and wrote the manuscript with input from all co-authors.
- T. Z. Regier assisted with the experimental data collection and organized portions of the experimental time.
- X. H. Xu synthesized the samples and performed the initial characterization measurements published previously.
- G. S. Chang performed some preliminary spectroscopy measurements, and assisted with the manuscript.
- E. Z. Kurmaev and A. Moewes supervised the project, assisted with data interpretation, and provided input for the manuscript.

Chapter 6

Band Gap Engineering

I'd put my money on the sun and solar energy. What a source of power! I just hope we don't have to wait until oil and coal run out before we tackle that.

—Thomas Edison, 1936 [127]

The previous chapter focused primarily on magnetic phenomena that occur upon introducing transition metals into semiconductors and insulators, but of course other changes take place as well. In particular, the introduction of transition metal impurities can have large effects on the electronic band gaps. Synthesizing new materials in efforts to tailor the band gaps for certain applications is known as *band gap engineering*.

Applications of band gap engineered materials are quite extensive, and are found in fields such as optoelectronics, water-splitting photocatalysts, and solar cells, among many others. For example, in the field of photo-catalytic water splitting to produce H_2 as an energy source, TiO_2 has long been considered a promising material. Some of the favourable properties of TiO_2 include a high photo-catalytic activity, low corrosion, low cost, and non-toxicity [128,129]. However, the native band gap of most forms of TiO_2 (there are several polymorphs, including rutile, anatase, and brookite) is in the range of 3.0 – 3.2 eV. An ideal photocatalyst would have a band gap of around 2.0 eV, in order to generate a strong photocurrent from the solar spectrum (which peaks in intensity at just over 2 eV, as shown in Figure 1.2) while driving the water splitting reaction (which requires at least 1.23 eV [129,130]). Thus, one would ideally try to modify the gap of TiO_2 to bring it near this desired value of 2.0 eV, while trying to keep many of its other favourable properties unchanged. Similar observations hold for other potential materials, such as ZnO, In_2O_3, and GaN, with gaps of about 3.4 [55], 3.0 [125,131], and 3.4 [55] eV.

Below we present some of our studies related to band gap engineering. First, in Section 6.1, we look at introducing titanium into SiO_2, an insulator with a wide band gap (~8.0 eV). While the pure and Ti-implanted gap energies we find are not very close to the visible range, this study

nonetheless provides a clear example of how strong gap modifications can be made and how soft x-ray spectroscopy can explain the source of these modifications. Next, in Section 6.2, we move on to a material that is very promising for applications in $Zn_{1-x}Ni_xO$. Lastly, in Section 6.3, we look at materials where instead of substituting transition metals for the cations, we replace oxygen anions with nitrogen-carbon ligands: the transition metal carbodiimides.

6.1 Titanium Ion Implantation in SiO_2

The combination of Ti and SiO_2 is somewhat of an ideal situation for band gap engineering. Pure SiO_2 has a wide band gap of about 8 eV, with a corresponding high energy conduction band onset. Titanium (IV) ions are formally $3d^0$, and thus lead to abundance of unoccupied $3d$ states in the conduction bands of materials they reside in. Accordingly, one would expect strong modifications of the wide SiO_2 gap when Ti ions are introduced into the material, as the empty $3d$ states should strongly affect the conduction band onset to lower it in energy. Indeed, some past studies have indicated that strong band gap modifications are possible in this situation. Using optical spectroscopy, it was found that the gap of SiO_2 could be reduced down to about 4 eV with the introduction of Ti [132]. Unfortunately though, with optical techniques one does not get a clear measurement of how the conduction and valence bands are independently modified; instead only the gap between the two is obtained. So it could not be verified in the optical study how exactly the Ti led to the gap reduction.

Additionally, it is important to know how the Ti ions interact with the SiO_2 structurally. Ideally a homogeneous material would be obtained through substitution of Ti into the Si sites, leading to tetrahedral Ti^{4+} centers. But there is also the possibility of other phases of material forming with Ti in other oxidation states. In previous studies of incorporating Ti into SiO_2 using a variety of techniques, including flame hydrolysis [132], the sol-gel method [133–136], chemical reduction [137], and ion implantation [138–142], varying results have been obtained regarding the Ti coordination and valence. Tetrahedral Ti^{4+} has in fact been observed in some studies employing flame hydrolysis or the sol-gel method with certain Ti concentrations [132–134, 136]. So far, however, only indirect evidence of Ti with T_d coordination has been found for ion implantation studies [139]. Other implantation studies have found metallic Ti [140] and Ti-composite nanostructures [138, 141, 142].

In order to add insight into these issues and provide a fuller understanding of the electronic structure modifications in SiO_2 via the introduction of Ti, we have studied Ti ion implantation

into high purity SiO_2 samples. The implantation was performed by our collaborators in Yekaterinburg, Russia, and we have applied synchrotron techniques as well as implantation simulations and crystal field XAS simulations to study the materials. Using these techniques we have indeed found tetrahedrally-coordinated Ti^{4+} and a reduced band gap, with independent measurements of the valence and conduction bands.

6.1.1 Experimental Details

The samples under study were prepared from amorphous SiO_2 (a-SiO_2) plates which were implanted with Ti^+ ions. The plates were 99% purity, and were $10 \times 10 \times 0.7$ mm^3 with surfaces of optical quality. The Ti implantation was carried out using a pulsed source with an ion beam current density of ~2–7 mA/cm^2 and a 400 μs pulse duration. The implantation energy was 30 keV, and the sample temperatures were maintained at 250 °C during implantation. Two samples were prepared with respective ion fluences of 1×10^{15} cm^{-2} and 5×10^{16} cm^{-2}. After implantation, the samples were annealed in air at 1000 °C for 1 hour.

Two reference samples were also used prepared. One was simply an unirradiated piece of the a-SiO_2 precursor material. The second was a SiO_2:TiO_2 mixture with 8% TiO_2 by weight, prepared by melting 99.9% purity TiO_2 and SiO_2 in a corundum crucible. The corresponding stoichiometry of this mixture is thus $(Si_{0.94}Ti_{0.06})O_2$. The mixture was melted under normal atmosphere at 2000 °C for 3 hours and then cooled. All sample synthesis was performed at the Ural Federal University in Yekaterinburg, Russia.

To study the coordination of the implanted ions we employed Ti $L_{2,3}$ XAS, and to determine overall changes in the electronic structure of the SiO_2 upon the introduction of Ti, we used both XAS and NXES at the O K edge. The NXES spectra were measured at BL8 of the ALS in Berkeley, while the XAS were measured at the SGM beamline at the CLS. To ensure the entire implantation region was probed, XAS spectra were collected using the bulk sensitive TFY technique (see Chapter 3). Note that the Ti $L_{2,3}$ TFY are susceptible to the TFY distortions discussed in Section 3.4 and elaborated on in Chapter 7. However, for Ti^{4+} the $3s \rightarrow 2p$ fluorescence channel (which does not suffer from distortions) is about as strong as the $3d \rightarrow 2p$ channel, minimizing the deviations from true XAS. Additionally, the thin layer of dilute, implanted Ti ions means saturation is minimized. The oxygen spectra were calibrated using a bismuth germanate (BGO) reference sample, where the main BGO XES peak was calibrated to 526.4 eV and the first XAS peak was calibrated to 532.7 eV. The Ti XAS spectra were calibrated using rutile TiO_2 as a reference, with the sharp L_3 peak

set to 457.25 eV.

6.1.2 Theoretical Details

Ion implantation is a powerful technique which permits the introduction of almost any impurity element into almost any type of host material. The 30 keV implantation energy used here leads to a Gaussian-shaped concentration profile of implanted ions located near the surface of the host. To approximately determine the depth of the Ti ions, and what concentration was achieved with the specified fluences, we performed implantation simulations using the SRIM program [143]. The implantation of a total number of 10^5 ions was simulated in order to obtain a converged concentration profile.

The Ti $L_{2,3}$ XAS spectra were analyzed with the crystal field model, which is often referred to as Multiplet Crystal Field Theory (MCFT). Such a model is usually quite successful for studying $3d^0$ systems [144]. The spectra were broadened with a Gaussian broadening to account for experimental resolutions, and a Lorentzian profile to account for the lifetime widths of the states. Note that for $3d^0$ systems it is often important to use a variable lifetime broadening as different portions of the spectra are broadened by different amounts. Here it was found that spectra could be reproduced well by using four different Lorentzian FWHM values across the span of the spectrum.

6.1.3 Results

Using the experimental implantation parameters as inputs for the SRIM simulation, we obtained the concentration profile shown in Figure 6.1. Note that because SRIM does not consider dynamic changes in the host material during the implantation process, there is no fluence dependence in the concentration profile shape. Thus the same profile applies to the two experimental fluences, but we have scaled the left and right vertical axes for the high and low fluence, respectively. From the Figure we see that the distribution has maximum concentration at 31.8 nm below the surface (denoted by R_p, meaning *projected range* [143]). The standard deviation of the projected range is $\sigma_{R_p} = 11.8$ nm. In the Figure we also denote the maximum and average concentrations (η_{max} and η_{ave}, respectively). For the higher fluence, we find maximum and average concentrations of 19.5 at. % and 6.9 at. %, respectively, while for the lower fluence we have 0.39 % and 0.14 %, respectively. Thus, the average concentrations of the two fluences fall above and below that of the SiO_2:TiO_2 mixture reference sample, which has a concentration of 2.0 at. %.

In Figure 6.2a, we show the experimental Ti $L_{2,3}$ XAS spectra of the implanted samples, the

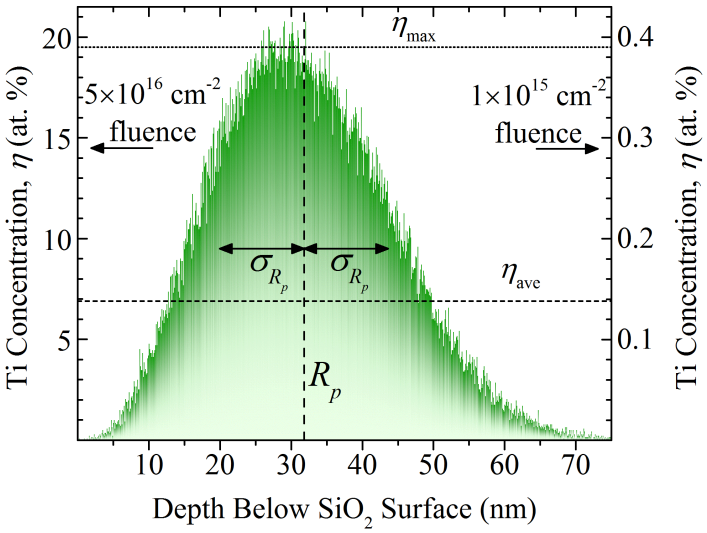

Figure 6.1: Simulation of the depth dependence of the concentration of implanted Ti ions, produced using the SRIM program. The left and right axes are scaled for the high and low implantation fluences used in experiment, respectively. The vertical dashed line denoted by R_p gives the average implantation depth, while σ_{R_p} gives the standard deviation of the implantation depth. η_{max} marks the maximum Ti concentration. This figure is adapted from Ref. [145].

reference sample, and a commercial rutile TiO_2 powder for comparison. One can see there are significant differences between the two implanted samples. The sample with the higher fluence (5×10^{16} cm^{-2}) has a spectrum which is very similar to that of the reference sample, while the spectrum of the lower fluence sample has different peak intensities and splittings. We also note that the TiO_2 spectrum is quite different from all of the others, ruling out the formation of TiO_2 aggregates in the samples.

The XAS spectra of Ti^{4+} are quite simple, due to the formal $3d^0$ ground state. This means the XAS final state is $2p^5 3d^1$, and there are no d–d multiplet interactions. Accordingly, in O_h coordination one can clearly distinguish between excitations into primarily e_g-type orbitals and excitations into primarily t_{2g}-type orbitals. This can be clearly seen, for example, in the reference spectrum of TiO_2 in Figure 6.2a. Note the spectrum is split by the $2p$ spin-orbit interaction into the L_3 region below 461.5 eV and the L_2 region above that energy. Within each of these regions we see two main peaks: a peak with mainly t_{2g} character at lower energy and a peak with mainly e_g character at higher energy. The splitting between these two types of peaks then relates closely to

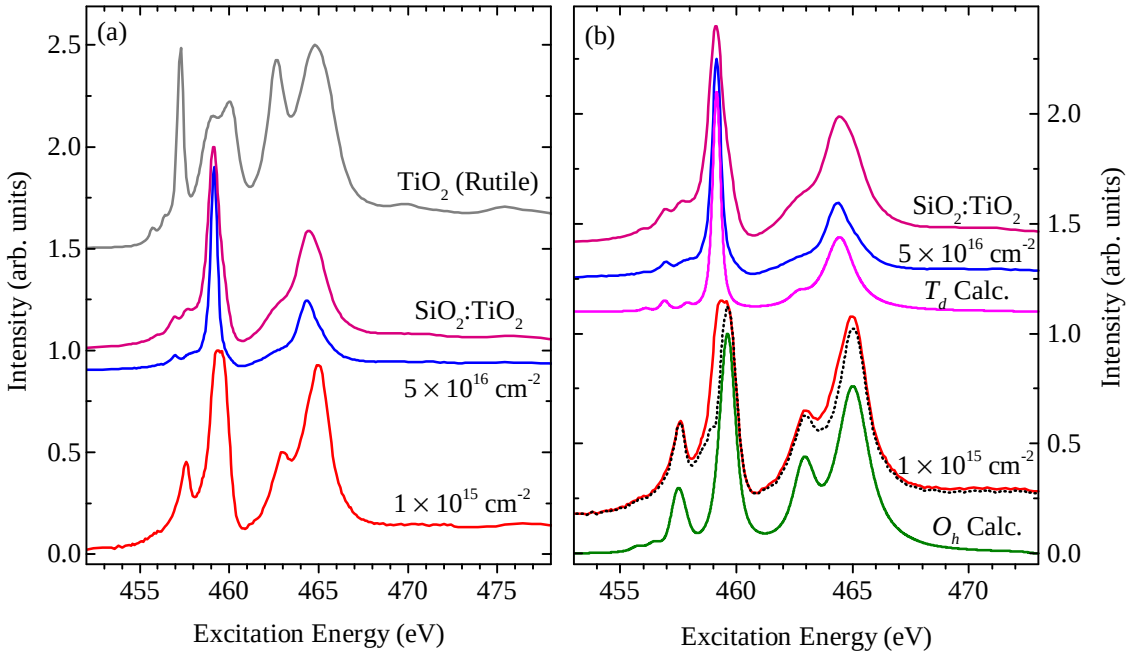

Figure 6.2: Ti $L_{2,3}$ XAS results for Ti-implanted SiO_2. (a) The raw experimental spectra. (b) Selected experimental spectra and corresponding MCFT calculations. The dotted spectrum is the result of subtracting 50% of the normalized 5×10^{16} cm^{-2} spectrum from the normalized 1×10^{15} cm^{-2} spectrum. These figures are adapted from Ref. [145]

the O_h crystal field splitting energy, $10Dq$. Note that some small pre-edge features are present in the spectrum due to the $2p-3d$ Coulomb interaction. Also, we see a splitting of the L_3 e_g-type peak at ~459 eV, due to a combination of long range effects and distortions from O_h symmetry [146–148].

For the implanted and SiO_2:TiO_2 reference samples, we see a similar general splitting into L_2 and L_3 regions, but we see quite different intensities and splittings for the peaks within these regions. These changes can be understood with the help of the MCFT calculations, as shown in Figure 6.2b. Here we see that the spectra of the high fluence sample and the SiO_2:TiO_2 reference are best reproduced with a Ti^{4+} calculation in tetrahedral symmetry. The specific inputs for the calculation are given in Table 6.1. For the low fluence sample, on the other hand, the spectrum is best reproduced with a calculation using O_h symmetry, again with parameters given in Table 6.1.

As mentioned in the introduction of this Section, for cationic substitution we expect the Ti to have T_d coordination, as this is the coordination of the Si atoms in SiO_2. Thus, our XAS results for the high fluence and SiO_2:TiO_2 reference samples indeed suggest we have successful substitution of Ti into the Si sites. For the low fluence sample, however, the O_h coordination indicates a different interaction of the Ti ions with the SiO_2. For the O_h calculation in this case, an additional

Ion	Symmetry	$10Dq$ (eV)	κ
Ti^{4+}	O_h	1.75	0.75
Ti^{4+}	T_d	-0.90	0.65

Table 6.1: Parameter used for Ti XAS crystal field model calculations. κ are rescaling factors for the intra-atomic Slater integrals, given as fractions of the Hartree-Fock values.

Gaussian broadening of 0.25 eV (above the amount which accounted for instrumental resolution) was necessary to establish good agreement with the experimental spectrum. This additional broadening suggests that in this case the Ti ions are possibly located in interstitial regions of the SiO_2, where varying crystal field effects at different sites with varying geometries would broaden the spectrum. Lastly, returning to the 1×10^{15} cm^{-2} experimental spectrum, we see that the evident splitting of the main L_3 peak at 459.4 eV indicates there are in fact some T_d-coordinated ions in this sample as well. A subtraction of 50% of the normalized higher fluence spectrum from this lower fluence spectrum yields the dotted curve in Figure 6.2b, which has improved agreement with the O_h calculation. Note that this analysis is not meant to be quantitative, but it does strongly support the fact that some T_d-coordinated ions are present in the lower fluence sample.

With the Ti coordination determined from the Ti $L_{2,3}$ XAS, we can now turn to the O K edge spectra for insight into the effects of Ti implantation on the SiO_2 band gap. Figure 6.3 shows the K edge XAS and XES for the full set of samples. As discussed previously, these spectra provide a close representation of the oxygen $2p$-projected conduction and valence bands, respectively. Considering first the XES spectra shown in panel (a) and enlarged in panel (b), we see a very similar shape for all samples (apart from the TiO_2 reference, expectedly), with only a slight shifting of the lower energy part of the spectrum when Ti is incorporated into the SiO_2. For the XAS shown in panel (a) and enlarged in panel (c), on the other hand, we see significant changes with Ti introduction. In particular, features appear in the pre-edge region of the SiO_2 spectrum as Ti is introduced. Comparing to similar features in the TiO_2 spectrum shown in shaded grey, we can see these features are indeed due to the unoccupied $3d$ states from the Ti ions [22, 45]. This is the effect that was hypothesized in the introduction: the copious empty $3d$ states should have a large effect to lower the conduction band of the wide gap SiO_2.

To quantify the changes in the band gap, we can use the second derivative method to determine the band edges from the spectra [44]. With this technique the first inflection point in both the XES and XAS is unambiguously chosen as the corresponding band edge. In the lower portion of

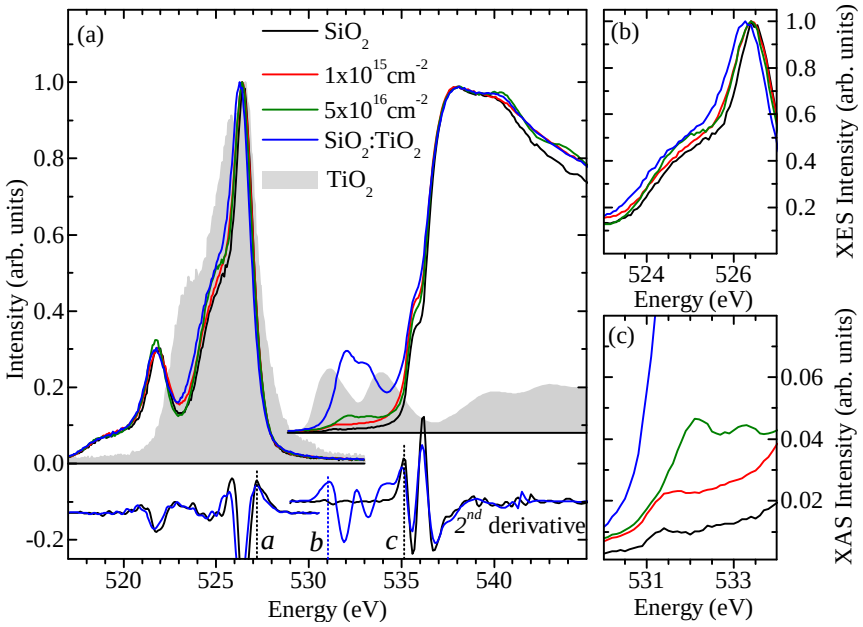

Figure 6.3: O K edge XAS and XES results for Ti-implanted SiO_2. (a) The raw experimental spectra, along with second derivative denoting the band edges. (b) An enlarged view of the XES. (c) An enlarged view of the XAS pre-edge region. This figure is adapted from Ref. [145]

Figure 6.3a, we plot these second derivatives for two samples. Shown in black are the results for pure SiO_2, with the valence band maximum VB_{max} marked by the dotted line labelled a and the conduction band minimum CB_{min} marked by the dotted line labelled c. Taking the difference between these two energies gives the gap of pure SiO_2: here we get a value of 8.0 ± 0.3 eV, in agreement with known values. In blue we show the second derivatives for the SiO_2:TiO_2 reference sample. Here we find that VB_{max} has not changed from pure SiO_2. However, the conduction band minimum has decreased considerably from the pure value, and is marked by the dotted line labelled b. Computing the gap gives 4.1 ± 0.3 eV, in close agreement for the optical value found for Ti-substituted SiO_2 [132]. Applying the second derivative technique again (but not showing the spectra for clarity in the Figure), we find the same band gap for the high fluence sample as we do for the SiO_2:TiO_2 sample. Finally, as clarified in the enlargement shown in panel (c) of the Figure, the XAS spectrum for the low fluence sample is very similar to the pure SiO_2 spectrum. Both show a small bump near 531.5 eV (likely due to defect states in the SiO_2), and the implanted sample only shows a constant increase in spectral weight compared to the pure sample—it does not show the distinct two-peaked structure found in the the higher fluence sample, the reference sample, and the TiO_2 sample. That we see only minimal changes for the low fluence sample is not surprising; there are 50 times fewer Ti atoms present in that sample compared to the high fluence sample, so the

Ti $3d$ character is expected to be weak. Additionally, if the Ti ions in this low fluence sample are located primarily in interstitial regions as suggested by the L edge results, the covalent interaction between the Ti and O will be reduced, weakening the Ti presence in the O edge spectra even further.

There are a few interesting points for discussion regarding these results. First, we found from the L edge spectra that low fluence implantation led to what is probably mainly interstitial Ti. For higher fluence implantation, however, we found almost entirely T_d coordinated Ti. This shows there is a fluence threshold to overcome for efficient substitution. Two possible explanations for this might be considered. First, the T_d coordination might be part of a stable phase of material where a certain ratio of Si and Ti sites need be present. If there is too little Ti, it might not be energetically favourable to form the Ti-O tetrahedra, causing the Ti to remain as interstitials. Another possible explanation could be related to a larger amount of damage to the lattice for higher fluence implantation. The increased damage might simply promote the incorporation of Ti into the Si sites. A preference toward either explanation is not evident from the data here, but future studies could look into this.

Finally, one last observation that is interesting to make is in regards to the presence of the pre-edge states in the O K XAS. For the samples with high enough Ti concentration, we see two distinct peaks in this region. It is known that these peaks in transition metal oxides relate to the e and t_2 bands of the metal atom [22], so the splitting between them relates to the crystal field splitting. Recalling from the previous chapter that the splitting for T_d coordination is generally weaker than that for O_h coordination, it makes sense that the splitting for our SiO_2:Ti samples (high fluence and reference) is smaller than that for the TiO_2, which has O_h coordination. Thus, the O K edge spectra can be used as supporting evidence for the coordination results drawn from the L edge spectra.

6.1.4 Conclusion

We have studied Ti ion implantation in amorphous SiO_2. We have shown that Ti $L_{2,3}$ XAS is sensitive to the Ti coordination, and from this we have found that above a certain fluence threshold we have very effective Ti substitution into the Si sites. Using oxygen K edge spectroscopy, we have found a significant band gap reduction upon the incorporation of Ti. The reduction—from 4.1 ± 0.3 eV down to 8.0 ± 0.3 eV—was found to be entirely due to a lowering of the conduction band onset. Thus, a clear explanation for the band gap reduction upon incorporation of Ti in SiO_2 has been presented.

6.1.5 Contributions

This work has been published as:

> R. J. Green, D. A. Zatsepin, A. Hunt, E. Z. Kurmaev, N. V. Gavrilov, and A. Moewes. The formation of Ti-O tetrahedra and band gap reduction in SiO_2 via pulsed ion implantation. *J. Appl. Phys.*, 113(10):103704, 2013.

The authors contributed as follows:

- R. J. Green performed the SRIM calculations, performed the crystal field XAS calculations, measured most of the synchrotron data, and wrote the manuscript, with input from co-authors.
- A. Hunt measured some of the synchrotron data, and provided significant input to the manuscript.
- D. Zatsepin and N. V. Gavrilov prepared the samples and assisted with the manuscript.
- E. Z. Kurmaev and A. Moewes supervised the project and assisted with the manuscript.

6.2 Ni Impurities in Zinc Oxide

Zinc oxide has been an extremely popular material in the literature of recent years. Traditionally it has found applications as sensors, transducers, and catalysts [149], due in large part to its combination of semiconducting and piezoelectric properties. Recently, interest has extended to nanostructured variants of ZnO, which exhibit unique electrical, mechanical, chemical, and optical properties compared to the bulk structure [149]. Additionally, as discussed in the previous chapter, ZnO has attracted a large amount of interest as a promising starting material for dilute magnetic semiconductors [55, 93].

The band gap of pure ZnO is about ~3.4 eV, out of the visible range [55]. Many studies have been undertaken to modify this gap through various means. In order to increase the gap of ZnO, it is often alloyed with MgO (which has a gap of 7.7 eV) [55]. Widening the gap is an approach taken for creating barrier layers in superlattice structures designed for stimulated emission [150]. Conversely, alloys of ZnO with CdO (which has a gap of 2.3 eV) are studied for reducing the gap [55]. Often the driving goal for narrowing the gap of ZnO is to push it closer to the visible spectrum, so that it could be more efficiently applied as a photo-activated material.

Here, we study the band gap modification of ZnO upon the introduction of nickel. $Zn_{1-x}Ni_xO$ has been studied in the past as a potential material for spintronics applications [107, 151, 152], but few studies have looked specifically at band gap effects when introducing Ni. Indeed, there are previous indications that band gap reduction is possible, as one $Zn_{1-x}Ni_xO$ film was reported to have

a gap of 3.18 eV [153]. We have investigated these possibilities by studying $Zn_{1-x}Ni_xO$ films using a combination of characterization techniques, including optical spectroscopy, XAS, NXES, and RIXS. Our results show extensive tenability of the ZnO gap by varying the Ni impurity concentration.

6.2.1 Experimental Details

$Zn_{1-x}Ni_xO$ films were prepared by our collaborators at the Bangladesh University of Engineering and Technology. The simple and low-cost spray pyrolysis method was used to synthesize the films. Precursor solutions of zinc acetate [$Zn(COOCH_3)\cdot 2H_2O$] and nickel acetate [$Ni(COOH_3)_3\cdot 4H_2O$] were used, with deionized water as a solvent. During the growth process, the substrate temperature was kept at 300 °C and was monitored with a thermocouple. $Zn_{1-x}Ni_xO$ films with $x = 0.02$, 0.04, 0.10, and 0.15 were prepared.

Characterizations were carried out using XRD, Scanning Electron Microscopy (SEM), electrical resistivity measurements, and optical transmittance measurements. Thorough discussion of the results from these tests can be found elsewhere [154], and here we provide just the key points relevant to this discussion. The SEM images showed that the films covered the substrates uniformly and exhibited a nano-fibrous morphology, which was consistent among samples. The XRD patterns showed that the hexagonal wurtzite phase of ZnO was successfully grown in polycrystalline form, and showed weak additional peaks at high Ni concentration (10 - 15%), indicative of a NiO-like phase being formed. Resistivity measurements verified the semiconducting nature of the samples and showed a decrease in resistivity as Ni concentration was increased.

The independent effects of Ni impurities on the conduction and valence bands were analyzed using oxygen K edge XAS and NXES, respectively. The NXES spectra were measured using Beamline 8 at the ALS [59], and the XAS were measured using PFY mode at the SGM beamline of the CLS [58]. The spectra were calibrated using a bismuth germanate (BGO) reference sample, where the main BGO XES peak was calibrated to 526.4 eV and the first XAS was calibrated to 532.7 eV.

The local environments of the Ni ions were analyzed using Ni $L_{2,3}$ XAS and Ni L_3 RIXS. The XAS spectra were collected using the IPFY technique in order to avoid sample charging effects (which were evident in TEY spectra that were also measured) and saturation effects (evident in PFY spectra). Due to the dilute nature of the samples, two to four scans were measured per sample with three silicon drift detectors (SDDs) simultaneously recording, in order to obtain sufficient statistics. NiO was used as a reference sample for calibration. The main L_3 XES and XAS peaks were calibrated to 850.9 and 853.1 eV, respectively.

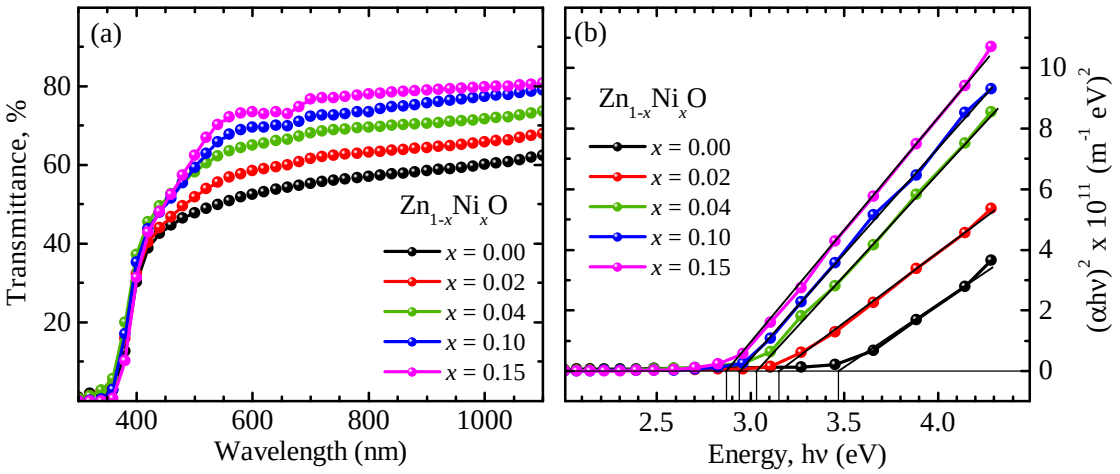

Figure 6.4: Optical data for $Zn_{1-x}Ni_xO$ measured by collaborators. (a) The raw transmittance spectra. (b) Band gap analysis. The band gaps are marked where the fitted linear lines cross zero. Figure adapted from Ref. [154].

6.2.2 Theoretical Details

The Ni XAS and RIXS spectra were analyzed using Single Impurity Anderson Model (SIAM) calculations. As introduced in Section 4.3.4, these calculations include atomic multiplet effects, crystal field splittings, and hybridization with a band of ligand (here, oxygen) $2p$ states. This is a more elaborate model than those used for the studies up to this point, but is necessary for obtaining information on the bonding properties from the charge transfer features in RIXS spectra. The parameter set for such calculations include the crystal field parameters ($10Dq$, $D\sigma$, $D\tau$), symmetry dependent hopping integrals (V_e, V_{t_2}), the charge transfer energy (Δ), the on-site Coulomb repulsion (U_{dd}), the core hole potential (Q), and the ligand bandwidth (W) and shape. Our RIXS calculations were performed for the same scattering geometry as experiment, which was given in Section 3.5.

6.2.3 Results and Discussion

Optical Spectra

Results of optical measurements performed by S. C. Das and J. Podder are shown in Figure 6.4. The raw transmittance spectra are displayed in panel (a), and show a consistent increase in transmittance with increased Ni concentration. From the transmittance data, the optical band gaps (E_g) were determined using the relation

$$(\alpha h\nu)^2 = A\,(h\nu - E_g) \tag{6.1}$$

	E_g (eV)	
x	optical (±0.10)	x-ray (±0.15)
0.00	3.47	3.32
0.02	3.15	3.13
0.04	3.03	2.98
0.10	2.94	2.89
0.15	2.87	2.93

Table 6.2: Measured band gaps for $Zn_{1-x}Ni_xO$. The gaps obtained using optical absorption are compared to those obtained from x-ray spectroscopy.

where A is a constant, $h\nu$ is the photon energy, and α is the absorption coefficient [155]. The values of $(\alpha h\nu)^2$ are plotted against the photon energy in panel (b) of the Figure. The direct-gap, semiconducting nature of the films is confirmed by the linear nature of the data, and from the plot (and displayed in the first two columns of Table 6.2), we see the optical gaps decrease from 3.47 eV for the pure ZnO film to 2.87 eV for the highest-concentration (15%) film. Thus, we have a clear trend where the gap narrows over a considerable range as more Ni is introduced.

Oxygen K Edge

To get a better understanding of what leads to the gap reduction upon the introduction of Ni, we can investigate the valence and conduction bands independently using oxygen K edge XES and XAS, much like was done for Ti-implanted SiO_2 in the previous section. In panel (a) of Figure 6.5, we show the spectra obtained for the samples. It is immediately evident that the XAS and XES show general shapes that are characteristic of ZnO [156], but a closer look shows the features begin to get slightly broader and less distinctive as the Ni concentration increases. For 15% Ni, the structures in the 540 – 545 eV range of the XAS are almost washed out completely. Similarly for the XES, we see a gradual filling of the valley between 520 and 523 eV. Thus we have clear first indications of the Ni ions altering the electronic structure.

Panel (b) of Figure 6.5 shows an enlarged version of the near-gap region for the XAS and XES spectra. Here we can see actual shifts in the band edges. The band edge onsets are determined using the second derivative technique, as was used for Ti-implanted SiO_2 in Section 6.1. The second derivatives are shown in the bottom of the panel, with the vertical bars marking the determined edge onsets. The energies of the edge onsets are plotted in panel (c) of the Figure, with the Ni concen-

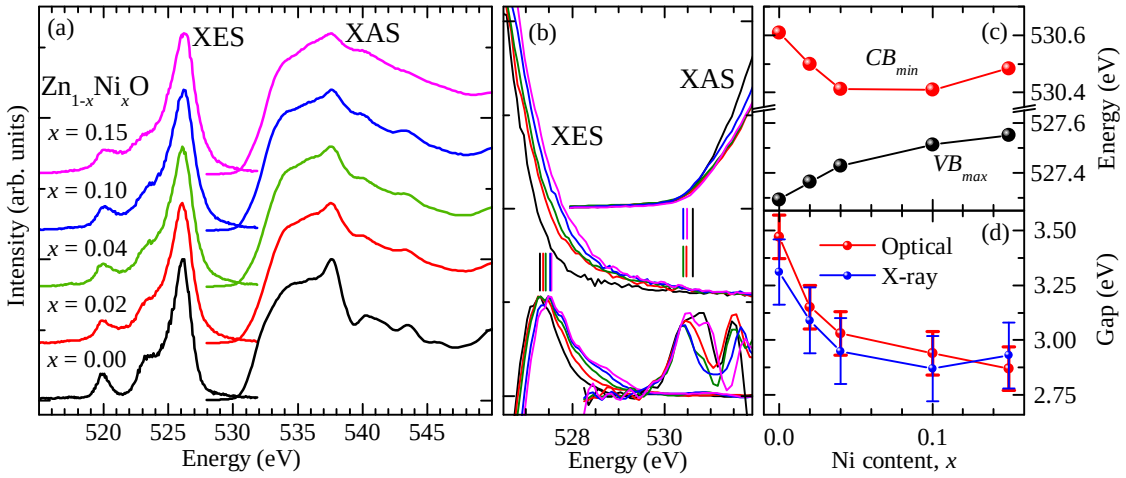

Figure 6.5: $Zn_{1-x}Ni_xO$ oxygen K edge results. (a) Raw experimental XAS and XES spectra. (b) Enlarged view of the near-gap region with second derivatives and band edges marked. (c) Extracted conduction band minima and valence band maxima. (d) Band gaps determined from x-ray and optical techniques. Figure adapted from Ref. [154].

tration as the abscissa. Here we see some interesting results. The valence band maximum (VB_{max}) extracted from the XES increases quickly for low Ni concentration, but the rate of increase slows for the higher concentration cases. Similarly, the conduction band minimum (CB_{min}) decreases strongly for low Ni concentration, but actually begins to increase again as the concentration is increased up to 15%.

If we take the difference between the CB_{min} and VB_{max} we get an approximation of the band gap, which is plotted along with the optically-determined gaps in panel (d). We see close agreement between the two approaches, and the behaviour of the band edges has manifested in a strong band gap reduction for low Ni concentration, with a weaker reduction at high concentration. These results further suggest Ni-substitution can be used to variably tune the gap of ZnO over a significant range.

Ni L Edge

To gain some insight on the specific interaction of the Ni atoms with the ZnO lattice, Ni $L_{2,3}$ XAS spectra were measured, and are shown in Figure 6.6a. The general shape shared by the spectra is clearly indicative of Ni in a +2 oxidation state ($3d^8$ configuration) [54, 73]. Note this is also evident from their similarity to a NiO reference spectrum shown in the Figure as well. Regarding the fine structure of the spectra, we see the $x = 0.15$ spectrum is quite similar to the spectrum of NiO, while the lower concentration samples (with $x = 0.02$ and $x = 0.04$) have spectra which are markedly different. In particular, we see a shoulder evident on the low energy side of the L_3 peak (~852.5 eV)

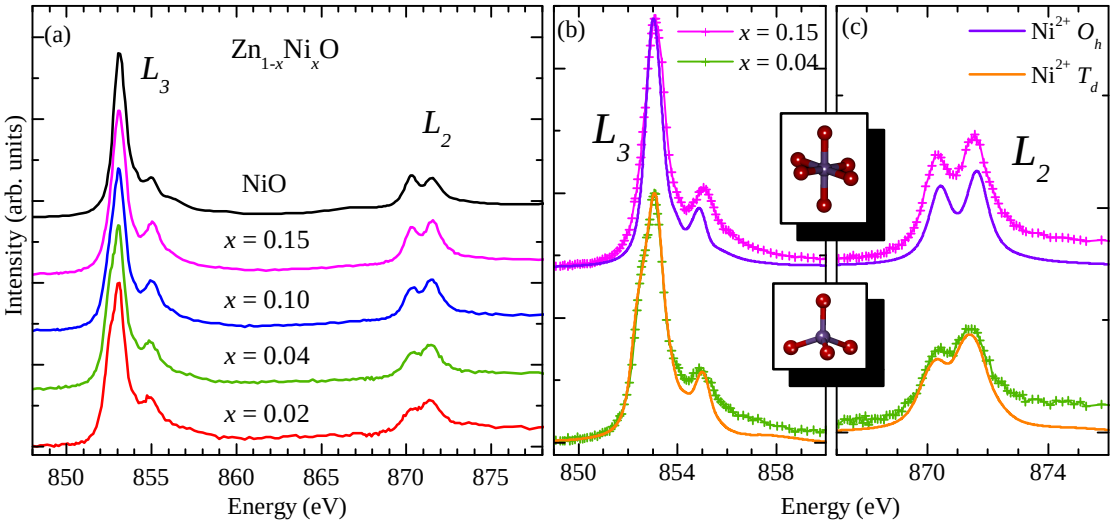

Figure 6.6: $Zn_{1-x}Ni_xO$ Ni $L_{2,3}$ XAS results. (a) Raw experimental spectra. (b) Enlarged view of the L_3 region, along with calculated spectra. (c) Enlarged view of the L_2 region, along with calculated spectra. The structures shown depict the symmetries used in the corresponding calculations. Figure adapted from Ref. [154].

for the low concentration samples, and we see the splitting of the L_2 region is less distinguished for these samples as well, with the 10% Ni concentration sample appearing intermediate between the lower and higher concentration cases. These spectral differences indicate changes in the local bonding environment of the Ni atoms as the Ni concentration changes. To understand the origin of these changes, SIAM calculations and spectral simulations were performed.

The calculated XAS spectra are shown in panels (b) and (c) of Figure 6.6. Here we see the high concentration sample is best modelled by a Ni^{2+} ion in octahedral (O_h) symmetry. For this calculation we have employed model parameters very similar to *ab initio* parameters available for NiO in the literature [157]. Additionally, the explicit shape of the O $2p$ VB for NiO was input from experiment (approximated from the O K-edge XES [44]). The full set of calculation parameters is shown in Table 6.3. For the low concentration samples, however, the spectra are best reproduced by Ni^{2+} in an approximately tetrahedral environment, indicating Ni substitution into the Zn sites of the ZnO. Again, the specific parameters used are shown in Table 6.3. The additional crystal field parameters, $D\sigma$ and $D\tau$, represent a trigonal symmetry distortion, consistent with the compression of the c-axis of the tetrahedron. This means the calculations are performed formally in C_{3v} symmetry as indicated in the Table, but the coordination is still close to T_d. This c-axis compression is consistent with the wurtzite ZnO lattice, where the c-axis Zn-O bond length is 1.80 Å, compared to 2.04 Å for the rest [115]. Note that the XAS is not very sensitive to the band shape, so we defer

Symmetry	$10Dq$	$D\sigma$	$D\tau$	V_e	V_{t_2}	Δ	$U-Q$	W
O_h	0.65	–	–	2.05	−1.20	4.0	−1.0	5.4
T_d (C_{3v})	−0.60	0.20	0.17	0.90	−1.50	4.0	−1.0	3.0

Table 6.3: Parameters for $Zn_{1-x}Ni_xO$ SIAM simulations. All values have units of eV. Slater integrals were scaled to 0.80 and 0.95 of Hartree-Fock values for the $2p^63d^8$ and $2p^53d^9$ configurations, respectively. Note the symmetry of the T_d case is formally C_{3v}, as a distortion along the C_3 axis of the tetrahedron was necessary to reproduce the spectra.

discussion of the narrow band width used for the T_d case to the RIXS analysis below.

From these XAS results we can see that for low Ni concentration (2 and 4%), we have substitution of the Ni into the Zn sites. However beginning somewhere between 4 and 10% concentration we begin to have octahedrally-coordinated Ni, and at 15% the spectra are dominated by O_h Ni. Thus, it seems there is a solubility limit between 4 and 10%, and above that limit we have a different phase of material with the octahedral coordination.

Having discerned the structural behaviour of the Ni atoms, we can now analyze the RIXS spectra to gain information on the electronic structure properties specific to these atoms. In Figure 6.7a, we show the experimental L_3 RIXS spectra collected for the series of samples. The spectra can be roughly divided into two slightly overlapping regions: between 0 and −4 eV are primarily *dd* excitations, while the −4 to −10 eV range contains primarily charge transfer (CT) excitations. Like the XAS, we see the RIXS spectrum for the 15% concentration sample is similar to that of NiO. The *dd* excitations are in close agreement, and the CT band has a similar intensity and width. However, for the lower concentration samples, we again see significant differences. The *dd* excitations—while not individually resolved at our experimental resolution—appear to shift in energy. Additionally, the CT band is narrower for these lower concentration samples compared to Ni and the 15% sample. Finally, the spectrum of the 10% concentration sample is intermediate between the extremes.

The SIAM calculations can provide insight into these RIXS changes. The *dd* excitations are mainly sensitive to the bonding symmetry (through the crystal field parameters and hopping integrals) whereas the CT band is more sensitive to the ligand band shape and charge transfer energy that enter into the calculation. Using the crystal field and hopping parameters found for the XAS, we get good agreement with the experimental *dd* excitations. The O_h calculation, shown in panel (b), has *dd* excitations of a similar shape which peak at the same energy as those of the NiO and 15% concentration sample. Accordingly, the *dd* excitations of the T_d calculation agree well with the low concentration samples.

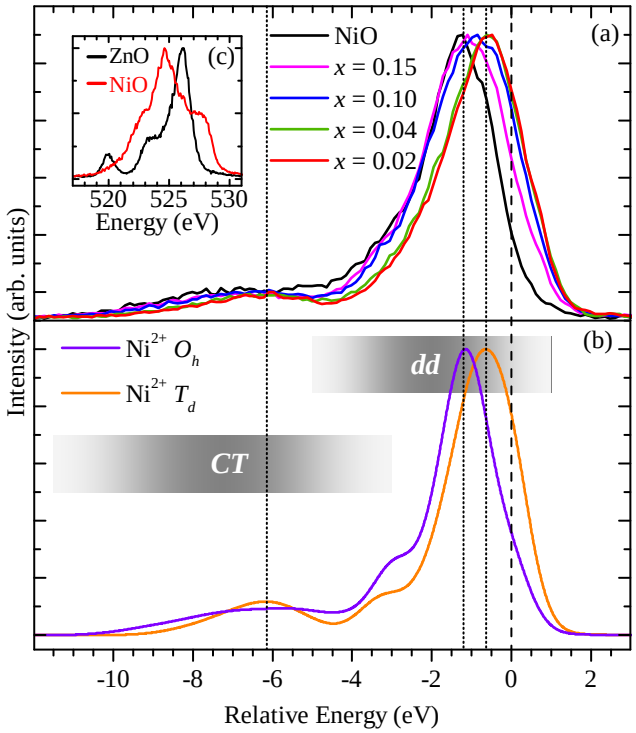

Figure 6.7: $Zn_{1-x}Ni_xO$ Ni L_3 RIXS results. (a) Experimental RIXS data. (b) Calculated RIXS spectra using the impurity model. The *dd* and charge transfer (CT) regions of the spectra are indicated. (c) Oxygen K edge XES used as input for ligand band shapes. This figure is adapted from Ref. [154].

To reproduce the narrowing of the CT band for the low concentration samples, we need to incorporate a different ligand band shape into the T_d calculation than we use for the O_h calculation. The XAS results help us here. For the low concentration case, we found the Ni atoms substituted into the Zn sites and were true impurity atoms. Thus, they are subjected to the O $2p$ valence band of ZnO when bonding. However, for high concentration the Ni atoms are no longer impurities, and a new phase of material has formed, which is very similar to NiO. This means the Ni atoms themselves now have an appreciable affect on the VB. In panel (c) of the Figure we plot the O K XES for NiO and ZnO. Recall that these provide us a view of the O $2p$ occupied DOS. We see the NiO $2p$ oxygen band is indeed much wider than that of ZnO. This is partly due to differing crystal structures, but largely due to the fact that Zn $3d$ states in ZnO form the isolated states at ~520 eV, minimally affecting the O $2p$ band, whereas the Ni $3d$ states in NiO interact strongly with the O $2p$ band causing it to widen.[1] Thus, we need to incorporate these NiO and ZnO band shapes into our

[1]To specify more clearly the nature of the 520 eV peak in the ZnO spectrum, it is due to transitions from the Zn $3d$ states well below the O $2p$ band to the O $1s$ core state, made possible by the finite O $2p$ – Zn $3d$ hybridization.

impurity model calculations for the high and low concentration cases, respectively. This is what has been done for the spectra in panel (b), and indeed we see the experimental trend is captured: for the low concentration, T_d case we have a narrow CT band peaked at $\sim$−6 eV, while for the high concentration case we have a broader CT band.

Finally, combining what we have learned, we can understand the band gap reduction upon the introduction of Ni. In pure ZnO the O $2p$ VB is quite narrow due to the semi-core nature of the Zn $3d$ states. The $3d$ states of the Ni atoms interact very strongly with this O $2p$ band, however, causing it to widen. This has the effect of pushing the VB_{max} up in energy (as we observed in the XES), narrowing the band gap. Eventually this widening effect must saturate as it approaches the NiO case, however, which is why we see the increase in VB_{max} taper off at high Ni concentration.

The behaviour of the CB_{min}, on the other hand, is likely more closely related to the change in Ni coordination. For low concentration, the empty Ni orbitals are t_2 (because of the T_d symmetry), whereas at high Ni concentration the empty orbitals are e_g. Thus our results tell us the t_2 states are more effective at lowering the conduction band than the e_g are. This could be a useful result for engineering strong band gap changes in other materials.

6.2.4 Conclusions

We have studied the electronic and crystal structure of $\mathrm{Zn}_{1-x}\mathrm{Ni}_x\mathrm{O}$ synthesized using the simple, low-cost spray pyrolysis method. Using x-ray spectroscopy and Anderson impurity model calculations, we have found that for concentrations up to 4% Ni, we have substitution of Ni into the Zn sites. For 10% and 15% phase segregation occurs and the Ni atoms have O_h coordination, similar to NiO. The introduction of Ni reduces the ZnO band gap in a very consistent (though non-linear) manner, providing a wide range of tenability from the pure ZnO value of 3.40 eV down to 2.90 eV. These results should be very beneficial to applications of ZnO directed toward optoelectronics and photocatalysis.

6.2.5 Contributions

This work has been published as

> S. C. Das, R. J. Green, J. Podder, T. Z. Regier, G. S. Chang, and A. Moewes. Band gap tuning in ZnO through Ni doping via spray pyrolysis. *J. Phys. Chem. C*, **117**(24):12745–12753, 2013.

The authors contributed as follows:

- R. J. Green collected the synchrotron data, performed the XAS and RIXS calculations, wrote the spectroscopy portion of the manuscript, and prepared the final version of the manuscript with input from co-authors.
- S. C. Das and J. Podder synthesized the samples, performed the optical and other characterization experiments, and wrote the synthesis portion of the manuscript.
- T. Z. Regier assisted with and provided support for the XAS measurements.
- G. S. Chang and A. Moewes supervised the project and assisted with manuscript preparation.

6.3 Transition Metal Carbodiimides

While the previous two studies in this chapter involved substituting transition metals into conventional semiconductors and insulators, we now study the effects of changing the anions in a solid already containing transition metals. Recently, it was found that materials analogous to transition metal monoxides can be synthesized, where the O^{2-} ligands are replaced with carbodiimide $(NCN)^{2-}$ ligands [158–164]. These MNCN materials have been successfully synthesized with M = Mn, Fe, Co, and Ni, among others. Here the O_h coordination of the metal ion is the same as the oxides, as shown in Figure 6.8, but the crystal forms a layered structure (to accommodate the multi-atomic ligands), rather than the rocksalt structure of the oxides. Remarkably, the MNCN materials are found to behave very similarly to the corresponding MO monoxides. In particular, MnO, FeO, CoO, and NiO are all antiferromagnetic insulators, and so too are their counterparts, MnNCN, FeNCN, CoNCN, and NiNCN.

Even with the similarities discussed so far, the NCN ligands are expected to induce significant changes in the electronic structure compared to the oxides, likely including increased covalency between the metals and ligands and possibly reduced (more useful[2]) band gaps. However, little is currently known in this area, due in part to the materials only recently being discovered, and in part to the fact that they are hard to synthesize and only small quantities are currently available. To this end, we have studied one of these materials, MnNCN, using x-ray spectroscopy and theoretical calculations. Small sample quantities are not an issue for most synchrotron-based techniques, since for our techniques the beamspot is only hundreds of microns in diameter and only probes a few hundred nanometers into materials. Note that this is a joint project with fellow Ph. D. student Teak Boyko (U of S), so his contributions will be identified where appropriate.

[2]The band gap of MnO, for example, is around 3.9 eV [165]. Reducing this could open the door for use in electronics or solar-based applications.

6.3.1 Experimental Details

A polycrystalline powder sample of MnNCN synthesized at RWTH Aachen University in Germany was studied, with a commercial powder MnO sample used as a reference. Specific details of synthesis procedures and crystal structure characterization can be found elsewhere [159]. As they are somewhat moisture sensitive, the MnNCN samples were kept under inert gas after synthesis, and transferred into ultra high vacuum for experiment using a glove-box flooded with N_2 to avoid exposure to atmosphere.

In order to study the direct interaction between the Mn ions and the NCN ligands, Mn $L_{2,3}$ XAS and L_3 RIXS spectra were measured. Like the previous studies in this thesis, the XAS was collected at the SGM beamline of the CLS while the RIXS was collected at Beamline 8.0.1 at the ALS. The XAS was measured using TEY mode. The same spectra were also acquired for MnO to enable a direct comparison. To directly study how the electronic band gap of MnNCN compares to MnO, nitrogen K edge XAS and XES were also measured. The XAS was measured using TFY mode at the SGM beamline of the CLS, while the XES was measured using Beamline 8.0.1 at the ALS.

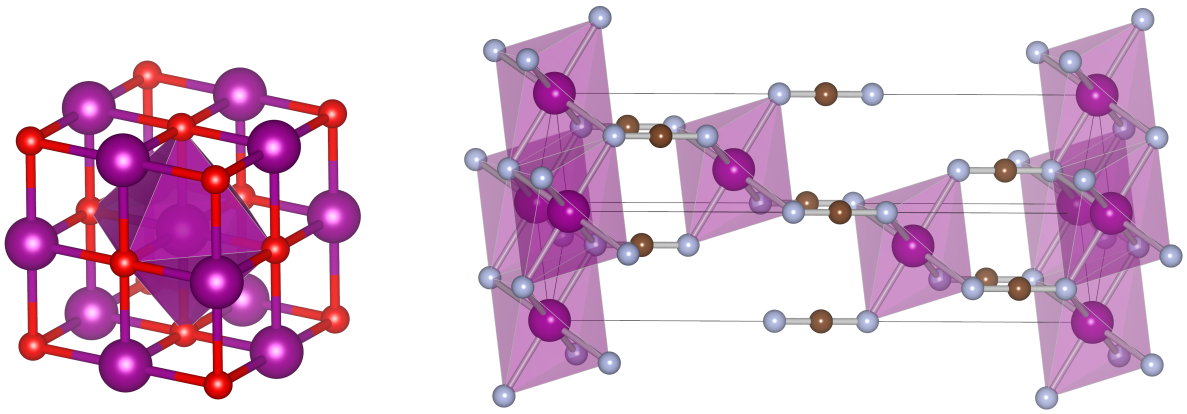

Figure 6.8: Comparison of MnO and MnNCN structures. MnO, shown on the left, has the rocksalt structure where the Mn and O atoms have octahedral coordination. MnNCN, shown on the right, has octahedral coordination of Mn with the NCN ligands, but a layered structure is now formed to accommodate the multi-atomic ligands. Colours: Mn–purple, O–red, N–blue, C–brown.

6.3.2 Theoretical Details

The electronic band gap was extracted from the N K edge spectra using the second derivative technique [44]. Though not presented here, an extensive DFT + U analysis of the DOS was also carried out by Teak Boyko. Such analysis proved very important, as it uncovered an unexpectedly large core hole effect in the nitrogen XAS which needed to be accounted for when determining the band gap.

The Mn L edge spectra were analyzed using the Single Impurity Anderson Model (SIAM) discussed earlier. Both MnO and MnNCN have approximately O_h coordination for the Mn ions, so only one crystal field parameter ($10Dq$) and two hopping integrals (V_{e_g} and $V_{t_{2g}}$) were needed to reproduce the spectra. Other parameters included the charge transfer energy (Δ), the on-site Coulomb repulsion (U), the core hole potential (Q), and the ligand band width (W) and shape.

6.3.3 Results and Discussion

Figure 6.9a shows experimental Mn $L_{2,3}$ XAS spectra for MnNCN and MnO (plotted with dotted lines). We see the spectra are very similar, and they expectedly exhibit the characteristic shape of Mn^{2+} ions with six-fold octahedral coordination [54, 113]. Since these spectra are sensitive to the local crystal field symmetry and strength, the similarity of the MnNCN spectrum to that of MnO reinforces the idea that the $(NCN)^{2-}$ ligands behave quite like the O^{2-} ligands of the oxide. In fact, the only differences evident between the spectra are minor effects in the regions above the L_3 and L_2 edges, specifically at ~644 and ~654 eV, respectively. We see the MnNCN has slightly more spectral weight in these regions, with the small dip at 644 eV noticeably filled in somewhat for MnNCN. These regions of the spectra are sensitive to charge transfer effects [54], so this is a first indication of increased covalency, or hybridization, between the Mn ions and the NCN ligands compared to the O ligands of the oxide. These changes appear quite minor in the XAS spectra, but this is mainly a consequence of the low sensitivity of XAS to the charge transfer effects. To gain more insight into these changes, we can look at the L_3 RIXS spectra.

The RIXS spectra are shown in Figure 6.9b. As with the Ni L_3 RIXS of the last section, the spectra can be divided into the charge transfer (CT) and dd regions, which slightly overlap. First, we note the dd excitations are very similar for the two materials (apart from slight differences due to different experimental energy resolutions of the measurements), which agrees with the XAS observations discussed above. However, we see significant changes in the CT regions of the spectra.

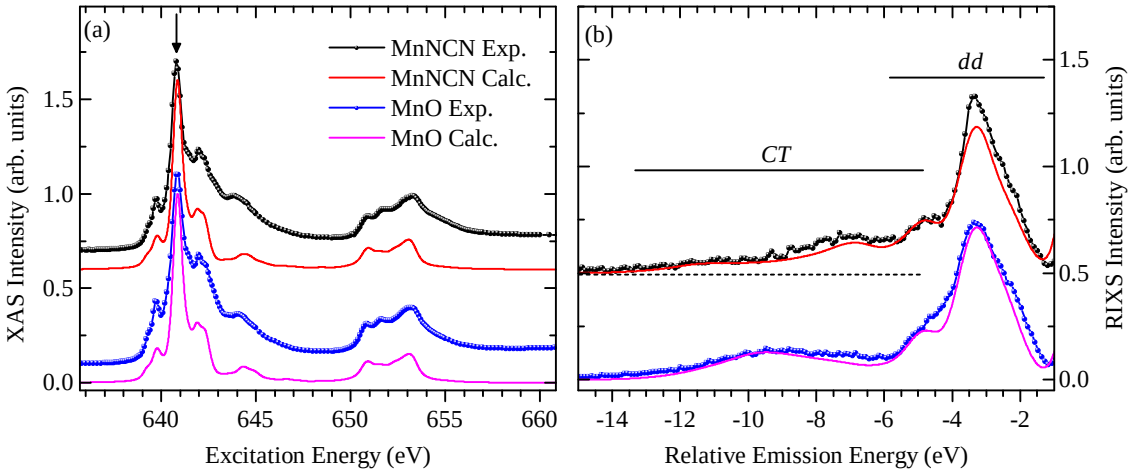

Figure 6.9: MnNCN Mn L edge XAS and RIXS. (a) The TEY XAS spectra, along with SIAM calculations. (b) L_3 RIXS spectra, along with SIAM calculations. The simulation parameters are given in Table 6.4

While the CT excitations of MnO show a single-peaked structure well separated from the *dd* region, the MnNCN CT excitations are more spread out with a two-peaked structure, and are shifted more into the *dd* region. This clearly indicates a decrease in the charge transfer energy of MnNCN compared to MnO, again reinforcing the XAS observations.

The observations made for both the XAS and RIXS can be understood using SIAM calculations. For each experimental spectrum in Figure 6.10, we show a corresponding spectrum calculated using the SIAM. We see good agreement in all cases and, most importantly, we see the calculations reproduce the changes between the spectra of the two materials. For the SIAM calculations, the Slater integrals (κ), crystal field ($10Dq$) and hopping integral (V_{e_g}, $V_{t_{2g}}$) parameters were taken from *ab initio* values for MnO available in the literature [157], and only slightly adjusted to improve agreement with experiment. Additionally, the difference between the on-site Coulomb interaction (U_{dd}) and the core hole potential (Q), was fixed to the typical value of -1 eV used for transition metal compounds [54] (variations of this value were tested, and -1 eV proved optimal). For the ligand band width and shape, we input experimental values from the N and O K XES for MnNCN and MnO, respectively. Thus, the only parameter truly allowed to vary for the calculations was the charge transfer energy, Δ. This quantity was expected to vary between the oxide and carbodiimide due to differences in ligand electronegativity. The final calculation parameters are shown in Table 6.4. Note that in Table 6.4, the values for Δ are given as the difference between the lowest $3d^5$ multiplet and the lowest $3d^6\underline{L}$ multiplet in the initial state before the inclusion of hybridization. This is not the same as the difference between the configuration-averaged energies which is often

Material	κ	$10Dq$	V_{e_g}	$V_{t_{2g}}$	$U-Q$	Δ	W
MnNCN	0.75/0.85	0.65	1.70	0.95	-1.0	3.82	8.0
MnO	0.75/0.85	0.65	1.70	0.95	-1.0	4.32	6.0

Table 6.4: SIAM parameters for MnNCN and MnO. Values for Slater integral scaling factors κ are given as fractional amounts of Hartree-Fock values. All other quantities have units of eV.

given [52, 54, 77, 78], but it is more meaningful in this case where we include variations in ligand band shapes and widths.

Once we have determined the optimal parameter set for the SIAM to reproduce the experimental spectra, we can actually extract the charge transfer band gaps using the ZSA theory. This involves correcting the Δ values in Table 6.4 for the energy level shifts upon incorporation of hybridization [23]. Performing this correction gives us estimated charge transfer band gaps for MnO and MnNCN of 3.8 and 3.2 eV, respectively. Thus, we do indeed see a reduction in the band gap of MnNCN compared to MnO, as hypothesized in the introduction to this section. Note that the value for MnO is in close agreement with the value of 3.9 eV found in the literature [165].

Using the N K edge spectra, the MnNCN band gap can be investigated as well. This analysis was performed by Teak Boyko, who measured the spectra shown in Figure 6.10. Using the second derivative technique to estimate the band edges, Teak extracted a difference of 2.0 eV between the maximum of the XES and minimum of the XAS. This does not agree well with the SIAM band gap, but the reason for this is that there are strong core hole effects acting to lower the N K XAS in this case. Using DFT + U calculations (presented in Ref. [166]) Teak calculated a predicted core hole shift of 1.4 eV for the XAS. This is quite large, especially compared to the oxides where we usually see almost no shift, but the reason is likely due to the extremely covalent NCN molecule that the nitrogen is a part of. Correcting the experimental gap with this core hole shift gives an estimated band gap of 3.4 eV for MnNCN. This is in better agreement with the SIAM results, again showing the gap is reduced compared to MnO.

6.3.4 Conclusion

We have performed a multi-faceted x-ray spectroscopy study of a new and relatively unstudied material, MnNCN. By analyzing Mn $L_{2,3}$ XAS and RIXS with a Single Impurity Anderson Model, we found that the local symmetry properties of the Mn ions in MnNCN are very similar to those

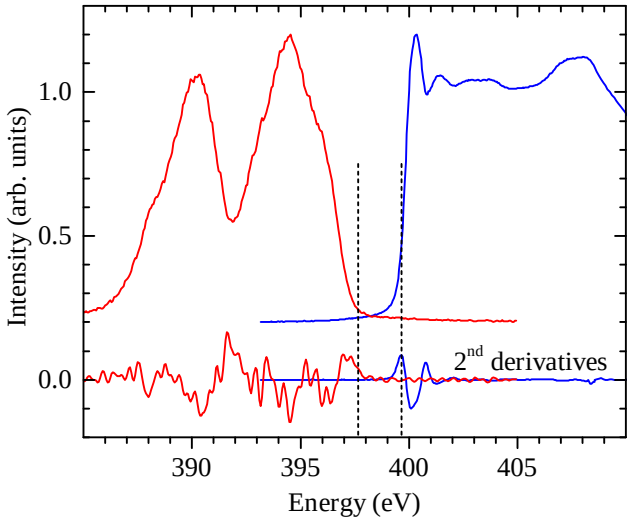

Figure 6.10: MnNCN N K edge XAS and XES. Second derivatives are shown with the corresponding band edges marked by the vertical dashed lines. Spectra acquired and analysis performed by T. D. Boyko.

in MnO. However, we found a decreased effective charge transfer energy in MnNCN, due to a larger ligand electronegativity and overall wider ligand valence band. Using the SIAM results we extracted band gaps of 3.2 and 3.8 eV for MnNCN and MnO, respectively. These results compared well with nitrogen K edge analysis performed by Teak Boyko, which found an electronic band gap of 3.4 eV for MnNCN. These results suggest MnNCN could prove useful for electronic applications, and suggest that other carbodiimides might show similar interesting properties.

6.3.5 Contributions

This work has been published as

> T. D. Boyko, R. J. Green, R. Dronskowski, and A. Moewes. Electronic Band Gap Reduction in Manganese Carbodiimide: MnNCN. *J. Phys. Chem. C*, **117**(24):12754-12761, 2013.

The authors contributed as follows:

- R. J. Green assisted with some of the spectroscopy measurements, performed the impurity model calculations and analysis, and assisted with manuscript preparation.
- T. D. Boyko collected most of the synchrotron data, performed the DFT+U calculations and corresponding analysis, and wrote the majority of the manuscript.
- R. Dronskowski synthesized the samples and provided input for the manuscript.
- A. Moewes supervised the project and provided input for the manuscript.

Chapter 7

Fluorescence Yield Absorption of Aqueous Complexes

The important thing in science is not so much to obtain new facts as to discover new ways of thinking about them.

—Sir William Bragg [167]

The previous two chapters have dealt with studying unique, new materials, designed for specific purposes. Now we will shift our focus to work which looked at well-studied materials, where the main motivation was to determine the applicability and utility of some new experimental and theoretical approaches. Additionally, our results from this study helped to clear up a recent controversy regarding fluorescence yield spectroscopy of aqueous transition metal complexes, and provided complementary characterizations of these well-known materials.

7.1 Background

As stated in Chapter 3, XAS is a well established technique that has existed in some form for about a century now. Currently, it is a widely used technique, and is still seeing rapid growth in various fields, like biology, environmental science, and catalysis. Advances in instrumentation continue to expand the influence of XAS, for example through the development of liquid flow cells in the past few years which have allowed for soft x-ray studies on liquid samples in the necessary ultra high vacuum environments.

Of course, every experimental technique has its limitations and disadvantages. As mentioned in Chapter 3, soft XAS almost always has to be detected using yield methods. Electron yield is plagued by a sensitivity to surface effects as well as sample charging effects. Fluorescence yield often suffers from saturation and self absorption, as well as a more fundamental issue: often fluorescence decay rates can vary strongly as a function of incident energy, meaning the detected signal is not truly proportional to the XAS.

The decay rate issue with fluorescence yield has been known about by part of the research community for a while now. De Groot and co-workers gave a nice demonstration of the effect in 1994 [57], and followed that up with another study in 2012 [168]. Other researchers have looked at the implications of fluorescence yield decay rates on magnetic dichroism studies [169,170]. However, instrumentation limitations have prevented clear experimental comparisons of pure XAS and pure PFY spectra. Ideally one would like to compare a bulk sensitive, true XAS spectrum, and a PFY spectrum with no saturation or self absorption. Until recently, this was a very demanding request.

Recent developments based on work done at the Canadian Light Source have yielded a new experimental XAS technique: Inverse Partial Fluorescence Yield (IPFY) [47, 48]. As introduced in Chapter 3 on page 22, IPFY involves detecting the fluorescence from edges not being resonantly excited. The inverse of this fluorescence is found to be directly proportional to the true x-ray absorption. The IPFY effect can be observed in Figure 7.1 where we show fluorescence spectra collected with the excitation energy scanned across the Fe absorption edge for $[Fe(H_2O)_6]^{3+}$. The intense line is non-resonant fluorescence from the O atoms in the solution, while the small bumps are the Fe fluorescence. Typically one detects the bumps (i.e. the direct Fe PFY), which are assumed to be proportional to the XAS. However, one can see that superimposed on the O fluorescence are dips which correspond to the inverse of the positive Fe signal. This is the IPFY signal, and thus by integrating the intensity of the O peak for each excitation energy, and taking the inverse of the resulting spectrum, one obtains a measure of the true XAS. With the recent addition of solid state detectors to the SGM beamline which can discriminate these two fluorescence lines, one can now measure PFY and IPFY simultaneously for the same material, allowing a very direct comparison of PFY and XAS (IPFY).

The inherent differences between PFY and XAS actually call into question many experimental results based on unique or unexpected observations in PFY (or TFY) spectra. For example, some studies have applied magnetic dichroism analyses of XAS collected in TEY and TFY modes. Upon finding differences between the results of each, conclusions are drawn about surface versus bulk magnetic effects [171]. However, one should be careful to check that the differences are not caused simply by decay rate effects in the fluorescence yield. A second example of conclusions drawn from unexpected fluorescence yield results is related to a discovery known as *dark channel* fluorescence recently found in TFY studies of aqueous iron complexes [172]. Spectral dips in the TFY spectra were attributed to hitherto undetected ultra–fast charge transfer processes from the Fe atoms to the ligands. However, these results were quickly called into question by authors suggesting the spectral

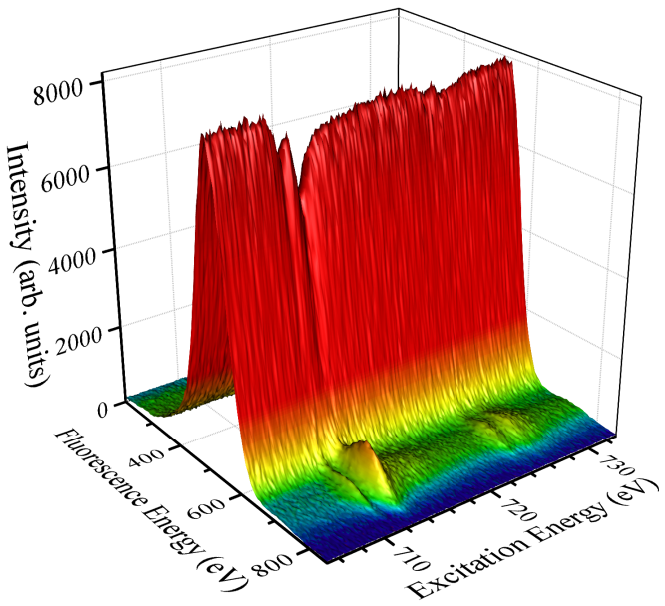

Figure 7.1: Energy-resolved, fluorescence yield XAS for the Fe $L_{2,3}$ edge of $[Fe(H_2O)_6]^{3+}$. The intense line is the oxygen fluorescence, while the bumps are the resonant Fe fluorescence. The dips in the oxygen line are inversely proportional to the Fe XAS.

dips were likely just an artefact of the TFY yield technique [173, 174].

In an effort to help resolve this dark channel fluorescence controversy, as well as carefully study the relation between XAS and PFY using the unique experimental capabilities of the CLS, we performed studies of two different aqueous Fe complexes. In each case we found distinct differences between the PFY and the true XAS measured via IPFY. These differences were explained very well by considering the true nature of PFY—that it is actually energy-integrated RIXS—and calculating expected differences between XAS and PFY. Our cluster model calculations showed the same differences between XAS and fluorescence yield that we found in experiment. They also provided a quantitative determination of the Jahn-Teller effect in aqueous Fe^{2+}. Further, we provide a general explanation of why lower energy portions of the PFY spectrum are suppressed, while higher energy portions are enhanced compared to the XAS. This result could be used as a way to probe spin states of materials using the XAS + PFY approach.

7.2 Experimental Details

Aqueous systems are in general quite difficult to study with transition metal L edge approaches. The necessity of Ultra-High Vacuum (UHV) systems for working with soft x-rays means the measurement environment is not conducive to liquid samples. However, recent instrumentation developments have led to liquid flow cells which separate the liquids from vacuum using a thin (~100 nm) Si_3N_4 window that is partially transparent to the x-rays. This allows one to perform photon–in, photon–out techniques such as XAS, XES, and RIXS on liquid samples.

We studied $[Fe(H_2O)_6]^{2+}$ and $[Fe(H_2O)_6]^{3+}$, prepared by dissolving $FeCl_2$ and $FeCl_3$ in 0.1 M HCl, respectively. The pH of the samples was brought to 1.0 through the addition of a few drops of 1 M HCl. The solution was continuously flowed through a liquid cell to eliminate the risk of radiation damage during the experiment. Separate solutions with three different Fe concentrations were prepared in each case to test for saturation and self absorption effects in the PFY.

The Fe $L_{2,3}$ XAS spectra were collected using three silicon drift detectors simultaneously recording. This allows detection of both the O K edge fluorescence yield and the Fe $L_{2,3}$ edge fluorescence yield, which then provide the IPFY and PFY spectra, respectively. The spectra were normalized to the incident flux as usual, and corrected for the energy dependence of transmission through the Si_3N_4 window by measuring the background signal over a very wide pre–edge energy range.

7.3 Theoretical Details

The IPFY and PFY spectra were investigated using the crystal field and cluster models, also referred to as multiplet crystal field theory (MCFT) and multiplet ligand field theory (MLFT), respectively. Six-fold coordinated Fe^{2+} is in general susceptible to weak Jahn–Teller (JT) symmetry distortions, so calculations were performed for the undistorted O_h case, as well as two possible JT distortions (D_{4h} and D_{2h}). For Fe^{3+} in O_h symmetry, there are no JT distortions, so only O_h calculations were performed.

The XAS (IPFY) simulations were performed using Equation 4.8. To simulate the PFY spectra, we have used Equation 4.9 on page 39 as defined for RIXS, but integrated out the emitted energy dependence, since we are only interested in total scattered intensity for a particular geometry. Thus,

using the same formalisms as Chapter 4, for temperature dependent PFY, we have

$$I_{PFY}\left(\omega,\boldsymbol{\epsilon},\boldsymbol{\epsilon}',T\right)=\sum_{i}\exp\left(-\frac{E_i-E_g}{k_BT}\right)I_i^{PFY}\left(\omega,\boldsymbol{\epsilon},\boldsymbol{\epsilon}'\right) \tag{7.1}$$

where the PFY intensity starting from initial state $|i\rangle$ is given by

$$I_i^{PFY}\left(\omega,\boldsymbol{\epsilon},\boldsymbol{\epsilon}'\right)\propto\sum_{f}\left|\sum_{\alpha,\alpha'}\epsilon_\alpha\left(\epsilon'_{\alpha'}\right)^*\mathcal{F}^{if}_{\alpha\alpha'}\left(\omega\right)\right|^2 \tag{7.2}$$

The scattering amplitudes $\mathcal{F}^{if}_{\alpha\alpha'}\left(\omega\right)$ are given by the same expression as for RIXS, shown in Equation 4.7 on page 37.

7.4 Results and Discussion

The experimental results of the IPFY and PFY measurements are shown in Figure 7.2. Panel (a) shows the results for the Fe^{2+} solution, while panel (b) shows the results for Fe^{3+}. The spectra for different concentrations are offset for clarity, with the PFY and IPFY overlaid in each case for direct comparison. As expected, the spectra obtained from the different techniques show marked differences. We see a general trend among all of the spectra where the PFY is weaker than the IPFY (i.e. the XAS) at low energies, but stronger than the XAS at high energies. For the different concentrations, we see primarily only changes in the statistical noise, demonstrating the saturation and self absorption effects are insignificant and are not the cause of the spectral changes.

7.4.1 Analysis of the Fe^{2+} Spectra

Recalling from our studies in previous chapters that XAS is very sensitive to local symmetry effects, the IPFY and PFY spectra provide a nice opportunity to examine the Jahn–Teller (JT) symmetry distortions for the $[Fe(H_2O)_6]^{2+}$. We expect such a distortion because the six–fold approximately octahedral coordination means the electrons in the $3d$ orbitals will be distributed as $t_{2g}^4e_g^2$. This is because H_2O ligands produce relatively weak crystal fields, leading to a high spin ground state. Accordingly, the first five electrons will be spin up, with one in each orbital. It is the sixth electron–which will be spin down in a t_{2g} orbital—that leads to the JT distortion. Since there would be a degeneracy in that the spin down electron could go into any one of the three t_{2g} orbitals, the Jahn–Teller theorem tells us that the complex will reach a lower energy by undergoing a physical distortion to remove the degeneracy [175].

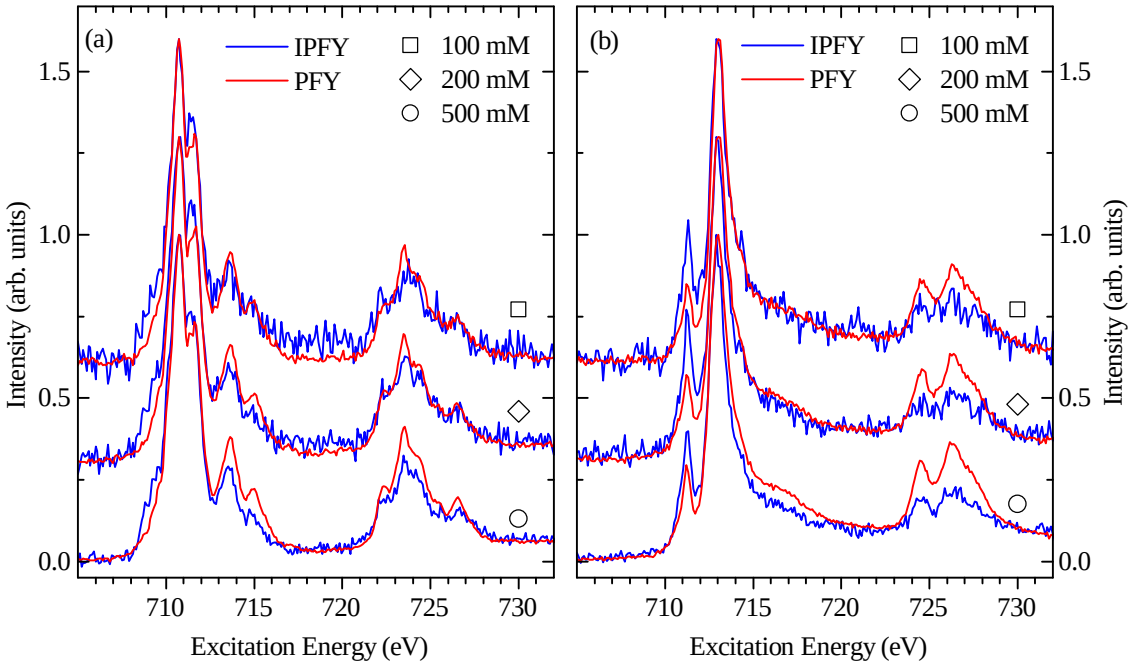

Figure 7.2: Experimental PFY and IPFY data for aqueous Fe complexes. (a) The data for the Fe^{2+} complex, measured at three different concentrations. (b) The data for the Fe^{3+} complex, also measured at three concentrations.

To investigate both the differences between the PFY and IPFY, as well as the JT distortion, we performed a set of MCFT calculations in different symmetries. Shown in Figure 7.3a (for XAS) and Figure 7.3b (for PFY), we have performed O_h calculations, as well as calculations with tetragonal (D_{4h}) and orthorhombic (D_{2h}) distortions, both of which could remedy the JT instability. All calculation parameters are given in Table 7.1. First, we see that in general our calculations capture the differences between the XAS and the PFY.[1] The weaker pre-edge and stronger peaks at 714 and 724 eV in the PFY compared to the XAS are both reproduced well. Next, we see that agreement between the O_h calculation and experiment is not ideal, as some peak intensities are incorrect. Both of the calculated distortion cases agree better with experiment, but we find the tetragonal (D_{4h}) distortion agrees best. This can be verified by the shoulder on the high energy side of the main L_3 peak, and by the shape of the overall L_2 peak (especially in the PFY), where the D_{4h} agrees with experiment better than the D_{2h}. Thus, not only have we shown the differences between XAS and PFY can be clearly understood, but we have provided a clear measurement of the type of JT distortion present. Some previous optical studies (see Ref. [24]) for an overview) have observed the

[1]Note that in this chapter we use XAS and IPFY somewhat interchangeably. Formally, the IPFY experimental technique measures the true XAS.

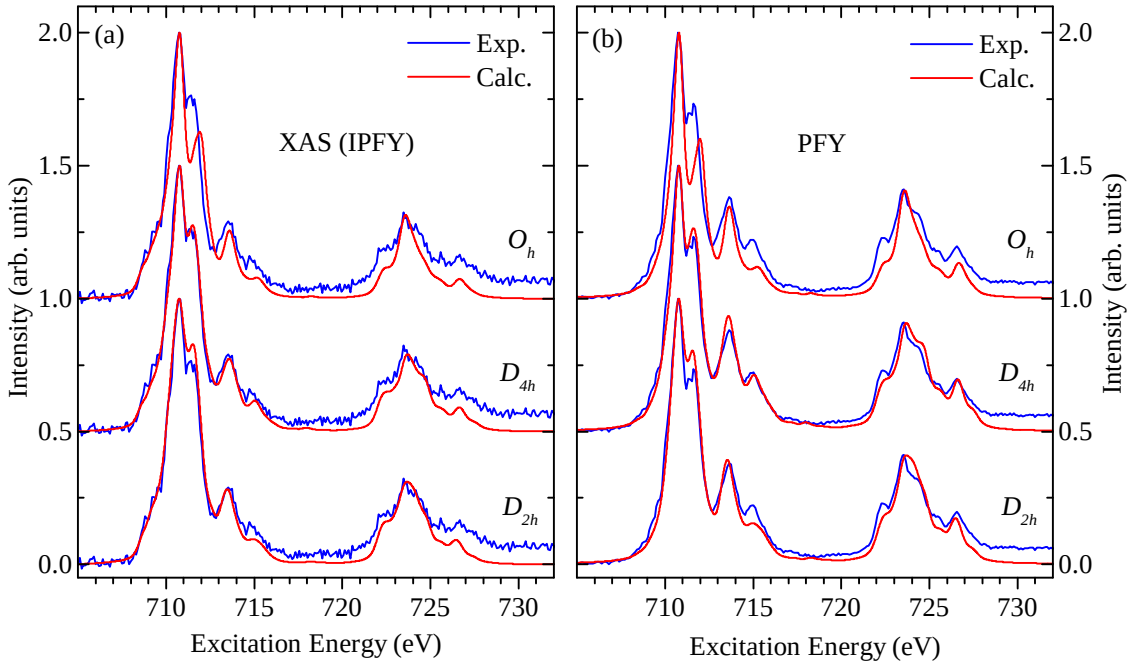

Figure 7.3: Crystal field model calculations of spectra for the Fe^{2+} complex. (a) The XAS calculations for different symmetries are compared to the experimental IPFY. (b) The PFY calculations for different symmetries are compared to the experimental PFY.

JT splitting in $[Fe(H_2O)_6]^{2+}$, but typically have not investigated specifically the type of distortion present nor its magnitude.

The agreement between the crystal field model calculations and experiment is quite good for $[Fe(H_2O)_6]^{2+}$, indicating the bonding is very ionic. To verify this, we performed Multiplet *Ligand* Field Theory (MLFT) calculations—i.e., the cluster model approach—using the D_{4h} symmetry case to determine if any improvement in agreement could be obtained. These MLFT calculations are compared with the MCFT and experimental spectra in Figure 7.4a for both XAS and PFY. From the Figure, we see the MLFT does have slightly improved agreement with experiment—for the peaks at 711.5 eV and 714.5 eV mainly, but overall the MLFT spectra are very similar to the MCFT spectra, verifying the ionic nature of the bonding in this sample. The MLFT calculation parameters are given in Table 7.2.

7.4.2 Analysis of the Fe^{3+} Spectra

The $[Fe(H_2O)_6]^{3+}$ complex is not susceptible to JT effects, so only O_h calculations needed to be considered. In Figure 7.4b we show the experimental XAS and PFY as well as the MCFT and MLFT calculations. Again we see the calculations reproduce the differences between XAS and PFY

Ion	Group	κ_{dd}	κ_{pd}	$10Dq$	Ds	Dt	Du	Dv
Fe^{2+}	O_h	0.85	0.85	0.85	–	–	–	–
Fe^{2+}	D_{4h}	0.80	0.90	0.85	−0.065	0.00	–	–
Fe^{2+}	D_{2h}	0.85	0.85	1.00	0.12	0.05	0.083	-0.096
Fe^{3+}	O_h	0.68	0.68	1.50	–	–	–	–

Table 7.1: MCFT model parameters fitted for aqueous Fe^{2+} and Fe^{3+}. κ_{dd} and κ_{pd} are fractional scaling factors of Slater integrals between d electrons and between p and d electrons, respectively. All other parameters are crystal field splitting parameters, in units of eV.

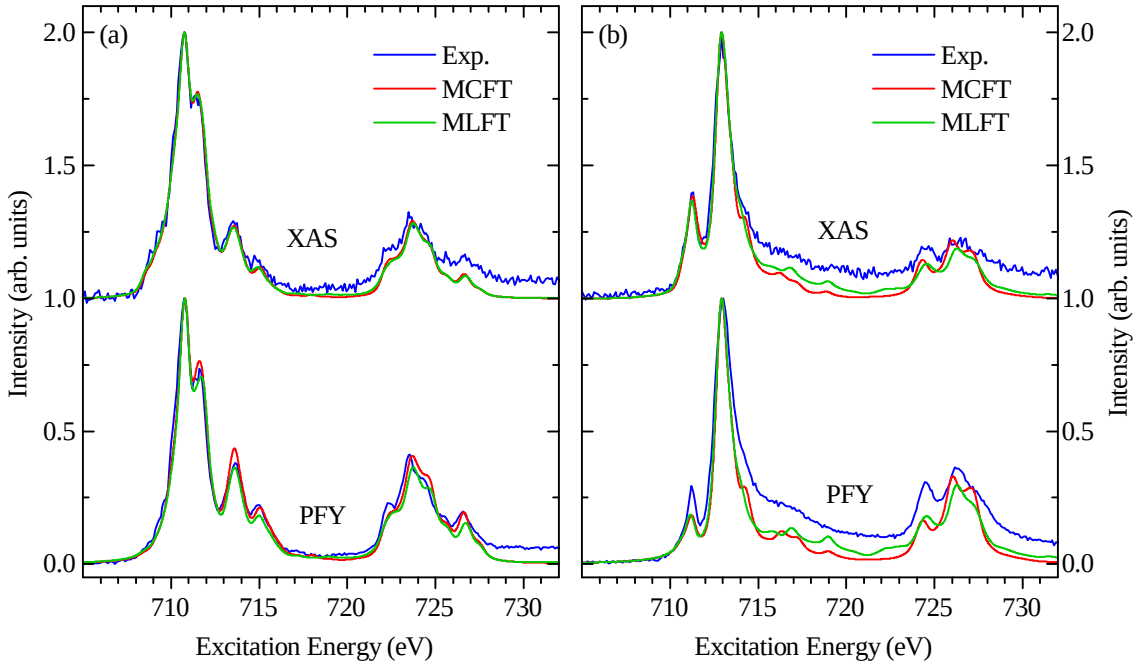

Figure 7.4: Comparison of crystal and ligand field models for aqueous Fe^{2+} and Fe^{3+}. Comparisons of the two models with the experimental XAS and PFY are shown for Fe^{2+} in (a) and Fe^{3+} in (b).

very well, though perhaps not quite as nicely as for the Fe^{2+} sample. Additionally, here we see greater differences between the MCFT and MLFT calculations, due to the fact that this sample is much more covalent than the Fe^{2+} sample. The MCFT and MLFT calculation parameters are given in Tables 7.1 and 7.2, respectively, and the significantly smaller Δ value compared to the Fe^{2+} sample quantifies the change in covalency. From the Figure we see the agreement is improved quite a bit for the MLFT calculation compared to the MCFT calculation. In particular, the shape of the L_2 peak agrees more with experiment, and the spectral weight between the L_3 and L_2 peaks—which is primarily sensitive to charge transfer effects—is improved for the MLFT calculation.

Ion	Group	κ_{dd}	κ_{pd}	$10Dq$	Ds	Dt	V_{e_g}	$V_{t_{2g}}$	Δ	$U-Q$
Fe^{2+}	D_{4h}	0.85	0.95	0.64	−0.045	0.0	1.75/1.85	0.88/0.94	6.5	-1.5
Fe^{3+}	O_h	0.85	0.85	1.20	–	–	2.0	1.0	1.0	-2.0

Table 7.2: MLFT model parameters fitted for aqueous Fe^{2+} and Fe^{3+}. κ_{dd} and κ_{pd} are fractional scaling factors of Slater integrals between d electrons and between p and d electrons, respectively. All other parameters have units of eV. $10Dq$, Ds, and Dt are crystal field splitting parameters. V_x are hopping integrals of x symmetry (note that in D_{4h} symmetry the e_g and t_{2g} parameters split into b_{1g}/a_{1g} and b_{2g}/e_g parameters, respectively. Δ is the charge transfer energy, U is the on-site Coulomb repulsion of the d electrons, and Q is the core hole potential acting on d electrons.

7.5 Explanation of XAS and PFY Differences

We have shown that PFY is different from XAS because it is better described as a second order scattering process. Additionally, our clear measurements of the PFY effect help to understand the distortions that were once attributed to dark channel fluorescence. Now we look at what specific information might be contained in PFY that can be extracted if properly understood. Ideally we would like to take full advantage of having an additional spectroscopy technique available.

One of the observations we made when comparing the XAS and PFY above was that when normalized spectra were plotted, the PFY generally was weaker than the XAS at low energies and stronger than the XAS at higher energies. If we consider what might be different between states at low energies compared to states at high energies, something that comes to mind are Hund's rules. These three rules—presented by Friedrich Hund in 1927 [9, 176]—qualitatively predict the ground state configuration of a multi-electron atom. The first of the rules is generally the most important, and states that terms with the largest spin (S) will be lowest in energy.

We should stress that Hund's rules are only general guidelines for predicting the ground state, and in some cases actually do not predict the correct ground state [9]. However, in general the full set of multiplets for an atom will be ordered to a certain extent in agreement with Hund's rules. Thus for isolated atoms or atoms in weak crystalline fields, lower energy states will tend to be higher spin states, and high energy states will tend to be of lower spin. This gives us a hint at what might be happening in the PFY spectra. In particular, perhaps high spin states are located at the low energy portion of the spectrum and do not decay as strongly as the low spin states located at the high energy portion of the spectrum.

Note that the large spin-orbit interaction present in the final states of $L_{2,3}$ XAS spectra results

in strongly-mixed spin states. In fact, it is because of this mixing that we can reach final XAS states of different spin from the ground state at all. Recall that as part of the dipole selection rules, we have $\Delta S = 0$, meaning that if we start in a high spin ground state (which we do for the aqueous Fe systems), then we should only reach high spin final states. However, the spin-orbit interaction mixes the spin character of the multiplets, allowing us to reach states with certain amounts of low spin character.[2] Thus instead of strictly saying high spin states are at low energy and low spin states are at high energy, we can say that the lower energy states have more high spin character and higher energy states have more low spin character.

For the atomic case (no crystal field or hybridization effects), we plot the XAS spectra of Fe^{2+} and Fe^{3+} in Figures 7.5a and 7.5b, respectively. Additionally, we break the spectra down into final states that have more of each type of spin character (here we have high, intermediate, and low spin cases for each oxidation state). Indeed, we generally see what Hund's rules suggest: the lower energy part of the spectrum is made of mainly of high spin states, while the high energy part of the spectrum is made of up intermediate and low spin states (apart from the S = 1/2 peak at low energy in the Fe^{3+} spectrum, which seems to be an exception to the rule). While these spectra are atomic and do not have exactly the same shape as the spectra shown above, this spin-state ordering should hold for the weak crystal fields in our aqueous complexes. Thus, it seems to be true that in the PFY spectra the high spin states lose intensity and the intermediate spin states gain intensity.

We can understand why the intermediate spin states gain intensity by again considering the dipole selection rules. Since we are restricted to starting from a high spin ground state, the states of mainly high spin character should be strong in the XAS because formally $\Delta S = 0$. However, for PFY, we are not restricted to decaying back to the ground state, so the intermediate spin states can decay strongly to intermediate spin states. Combinatorics and the Pauli exclusion principle tell us there should be an abundance of intermediate spin states to decay to (i.e. there are more ways to arrange electrons with mixed spins rather than with more high spins), so the intermediate spin states become magnified in the PFY.

These results suggest that one can use the comparison of PFY and XAS to extract information regarding the spin states of a material. More rigorous theoretical details are currently being investigated to determine the feasibility of this approach.

[2] Even the ~50 meV spin-orbit interaction in the $3d$ shell mixes the initial states somewhat.

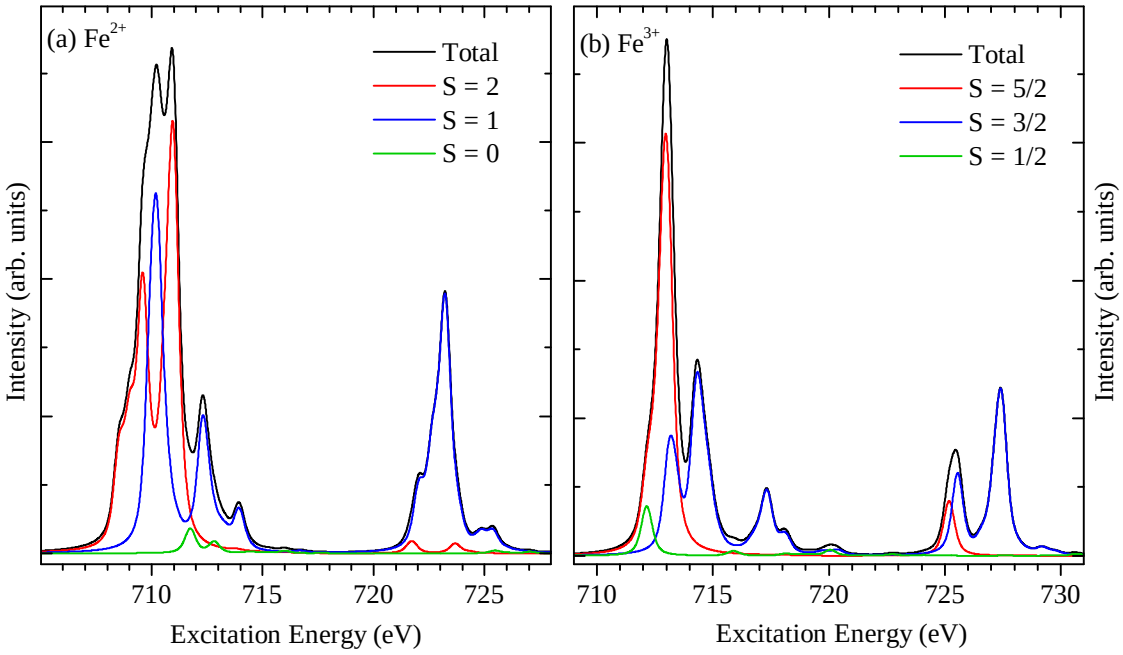

Figure 7.5: Atomic Fe XAS spectra broken down by final spin states. (a) Spectra for Fe^{2+}. (b) Spectra for Fe^{3+}. The calculations use the atomic model discussed in Chapter 4, with Slater integrals scaled to 80% of Hartree-Fock values.

7.6 Conclusions

We have employed the unique experimental facilities of the Canadian Light Source to perform a direct comparison of true XAS (via IPFY measurements) and fluorescence yield XAS (via PFY measurements) for aqueous Fe complexes. Our spectra allowed us to help rule out the phenomenon of dark channel fluorescence in fluorescence yield XAS spectra. The results also provided a direct and quantitative analysis of the Jahn-Teller effect for aqueous Fe^{2+}. Further, our results showed clear differences between XAS and PFY which were explained well by considering PFY as a second order scattering process. We explained the PFY shape using dipole selection rules and Hund's rule ordering of the spin character of states. This work shows potential for a new technique to be developed which can probe spin character of materials in a very direct manner.

7.7 Contributions

A manuscript has been prepared based on the work presented in this chapter and is near the submission stage:

T. Z. Regier, R. J. Green, D. Peak, A. J. Achkar, J. S. Tse, A. Moewes, and D. G.

Hawthorn. Excited state spin sensitivity through the comparison of fluorescence and absorption intensities at the Fe L-edge of ferric and ferrous solutions. To be submitted for publication, 2013.

The authors contributed as follows:

- R. J. Green performed the XAS and PFY calculations, developed the spin-based explanation of PFY spectra, and assisted with writing the calculation-related portions of the manuscript.
- T. Z. Regier organized the project, lead the experimental data acquisition, and wrote most of the manuscript.
- D. Peak assisted with experiments, especially with sample preparation, and provided input for the manuscript.
- A. J. Achkar and D. G. Hawthorn contributed regarding the IPFY technique and provided input for the manuscript.
- J. S. Tse and A. Moewes provided insight for the calculations and data interpretation and contributed to the manuscript.

Chapter 8

Conclusions and Future Work

No man should escape our universities without knowing how little he knows.

—J. Robert Oppenheimer

At the beginning of this thesis, we introduced a need for improved understanding of the magnetic and electronic effects of transition metal impurities in semiconductors. Such materials have exciting applications in the fields of spintronics, solar-based energy production, and various other fields of applied electronics. Our work has helped address this need and has satisfied most of our goals, but there are still opportunities for further work. Below we summarize our results and implications of our results, and present some specific paths where future work could contribute further.

8.1 Conclusions

In the introductions of Chapters 1 and 5, we discussed the field of spintronics and potential materials for use in spintronics called dilute magnetic semiconductors (DMSs). We introduced the varied and conflicting results that have plagued the field of DMS research over the past decade. This relates to one of our main goals, which was to assist in resolving the conflicting results from different studies in this field. By applying experimental synchrotron techniques and theoretical quantum model calculations using software developed during this thesis work, we have made some contributions which should be beneficial to the field. For different materials exhibiting different magnetic behaviour, we explained the differences based on a careful analysis of the physical locations of impurity atoms. We showed these locations were very sensitive to the synthesis parameters, and could be responsible for some of the discrepancies in the field. Additionally, for Fe-substituted In_2O_3, we revealed that room temperature ferromagnetism was due to substitutional Fe atoms adjacent to oxygen vacancy sites in the lattice. This is a direct confirmation of some existing theories for DMS materials, and should help to develop a better understanding of magnetism in such materials.

The second of the main goals of our work was to investigate the possibilities of band gap engineering in semiconductors and insulators through the introduction of transition metal atoms. The motivation for this goal was the development of materials suitable for solar-based energy production (either through H_2 production or direct solar conversion), as well as materials suitable for applications such as optoelectronics which require specific electronic band gaps. Again we performed synchrotron experiments which allowed us to study changes in the semiconductor valence band and conduction band independently, providing clear insight into the effects induced upon the introduction of transition metals. We showed that in Ti-implanted SiO_2, strong band gap reductions of about 4 eV were induced solely by the introduction of Ti $3d$ states to the conduction band. For Ni-substituted ZnO, we demonstrated a band gap tenability through varied Ni concentration and provided a thorough explanation of two regimes of band gap behaviour. Finally, we showed that the carbodiimide MnNCN behaves much like MnO but with a narrower, more useful band gap. We used an Anderson impurity model approach to directly compare MnNCN and MnO, explaining why the band gap of MnNCN was smaller. These results demonstrate the wide range of possibilities for band gap tuning by the introduction of transition metal atoms.

Finally, using the computational techniques developed in this work, we performed a study comparing true x-ray absorption spectroscopy (XAS) and partial fluorescence yield (PFY) XAS for aqueous iron complexes. Our calculations agreed with the experimental observations where PFY deviated from the XAS. We explained these PFY deviations based on excited spin states of the iron atoms, a result which hints at a possibly powerful experimental technique. By combining PFY and IPFY, one might be able to determine quantitative spin state information about novel materials. Lastly, we also showed during this study that fluorescence yields of aqueous compounds can be properly understood without the need of the controversial dark channel fluorescence process, and we obtained a quantitative description of the Jahn-Teller effect in aqueous Fe^{2+}.

8.2 Future Work

As described above, the work presented in this thesis has led to some interesting conclusions which should benefit the research community. However, there are areas where our results can still be expanded on. Below we discuss some work that is currently under way and present some other directions that can be investigated.

8.2.1 Dilute Magnetic Semiconductors

The field of dilute magnetic semiconductors is vast, to say the least—a simple search for this term on the Thomson Reuters *Web of Science* currently yields 5482 publications. This number is especially large, considering the field only became popular about fifteen years ago. Part of the reason for the large amount of research directed at this field is that there are a lot of candidate materials to study. In principle, any of the $3d$ transition metals can be introduced as an impurity in any semiconductor, and the resulting material can be studied. Thus, a natural extension of future work based on this thesis is to apply our techniques for studying impurities in semiconductors to other DMS materials. The goals would be to investigate controversial or conflicting claims using these techniques (RIXS with a model Hamiltonian analysis) to try to add insight to the field. The ultimate goal is to reveal an ideal DMS material for applications: one that is easy to reliably synthesize, interfaces well with conventional electronics, and exhibits magnetic behaviour at room temperatures. At present it seems that the first of these criteria is the most difficult to address (evident by the varied results for similar materials in the literature), and our techniques should be helpful in distinguishing which materials have been reliably synthesized.

8.2.2 Band Gap Engineering

Similar to the arguments above, one could introduce any of the transition metals into almost any kind of insulator or semiconductor and study the band gap of the resulting material. The approach of using ligand K edge XAS and XES to determine the electronic band gap, and adding transition metal L edge XAS and RIXS to help understand why the band gap has a certain value, not only can successfully analyze a new material, but can also help predict how to design other materials. For example, we saw that the empty Ti $3d$ states helped drastically lower the conduction band in SiO_2, while the mostly full Ni $3d$ states helped raise the valence band in ZnO. The suggests that combining Ti and Ni incorporation in either host could yield a further reduced gap or improved tenability. Such a study would definitely be interesting to undertake in the future.

8.2.3 Fluorescence Yield XAS

Our studies on the fluorescence and inverse fluorescence yields of aqueous iron showed some very interesting results. We provided a suggested explanation for the deviations of the PFY from the IPFY, based on the spin character of the excited states. However, this analysis was largely qualitative.

An important extension of our work will be to perform a more rigorous theoretical interpretation to try to quantify the differences between the spectra. In a similar vein as the sum rules developed for x-ray magnetic circular dichroism, perhaps quantitative spin information can be revealed through an analysis based on PFY and IPFY spectra.

8.2.4 Computational Software

During the course of this thesis work, we have developed extensive software to aid in the analysis of spectra using model Hamiltonians, starting from very powerful existing codes. Our software is currently very useful, and is used by several other members in our research group. However, steps are under way to further improve the software, both in terms of user friendliness and the range of calculations possible. Eventually the software will be released to the broader synchrotron research community. We have found it to be a very helpful analysis tool for the studies contained in this thesis, and hope that others can find it just as useful in the future.

References

[1] William Shockley. The path to the conception of the junction transistor. *IEEE Trans. Electron Devices*, 23(7):597–620, 1976.

[2] G. E. Moore. Moore's law at 40. In *Understanding Moore's Law: Four Decades of Innovation*. Chemical Heritage Foundation, 2006.

[3] Intel microprocessor quick reference guide, (accessed June 2013). http://www.intel.com/pressroom/kits/quickrefyr.htm.

[4] S. A. Wolf, D. D. Awschalom, R. A. Buhrman, J. M. Daughton, S. von Molnar, M. L. Roukes, A. Y. Chtchelkanova, and D. M. Treger. Spintronics: A spin-based electronics vision for the future. *Science*, 294(5546):1488–1495, 2001.

[5] C. Felser, G. H. Fecher, and B. Balke. Spintronics: A challenge for materials science and solid-state chemistry. *Angew. Chem. Int. Ed.*, 46(5):668–699, 2007.

[6] Air mass 1.5 reference solar spectral irradiance, (accessed May 2013). http://rredc.nrel.gov/solar/spectra/am1.5/.

[7] J. H. Van Vleck. Quantum mechanics: The key to understanding magnetism. In *Nobel Lectures*. Nobel Media AB, 2013.

[8] D. Mendelejeff. On the relationship of the properties of the elements and to their atomic weights. *Z. Chem.*, 12:405–406, 1869.

[9] R. D. Cowan. *The Theory of Atomic Structure and Spectra*. University of California Press, 1981.

[10] A. P. French and E. F. Taylor. *An Introduction to Quantum Physics*. W. W. Norton & Company, Inc., 1978.

[11] M. Kaupp. The role of radial nodes of atomic orbitals for chemical bonding and the periodic table. *J. Comput. Chem.*, 28:320–325, 2006.

[12] A. Hunt, D. Muir, and A. Moewes. Studying 4d-4f transitions in Er using resonant inelastic scattering. *J. Electron. Spectrosc. Relat. Phenom.*, 144 - 147(0):573 – 576, 2005.

[13] A. Moewes, A. V. Postnikov, E. Z. Kurmaev, M. M. Grush, and D. L. Ederer. Resonant mixing of widely separated intermediate states and charge transfer at the 4d - 4f resonance of La compounds. *Europhys. Lett.*, 49(5):665, 2000.

[14] J. H. de Boer and E. J. W. Verwey. Semi-conductors with partially and with completely filled 3d–lattice bands. *Proc. Phys. Soc.*, 49(4S):59, 1937.

[15] J. Stöhr and H. C. Siegmann. *Magnetism: From Fundamentals to Nanoscale Dynamics*. Springer, 2006.

[16] N. F. Mott. The basis of the electron theory of metals, with special reference to the transition metals. *Proc. Phys. Soc. A*, 62(7):416, 1949.

[17] N. F. Mott. On the transition to metallic conduction in semiconductors. *Can. J. Phys.*, 34(12A):1356–1368, 1956.

[18] N. F. Mott. The transition to the metallic state. *Philos. Mag.*, 6(62):287–309, 1961.

[19] J. Hubbard. Electron correlations in narrow energy bands. II. The degenerate band case. *Proc. R. Soc. A*, 277(1369):237–259, 1964.

[20] J. Hubbard. Electron correlations in narrow energy bands. III. An improved solution. *Proc. R. Soc. A*, 281(1386):401–419, 1964.

[21] P. Olalde-Velasco, J. Jiménez-Mier, J. D. Denlinger, Z. Hussain, and W. L. Yang. Direct probe of Mott-Hubbard to charge-transfer insulator transition and electronic structure evolution in transition-metal systems. *Phys. Rev. B*, 83:241102, 2011.

[22] F. M. F. de Groot, M. Grioni, J. C. Fuggle, J. Ghijsen, G. A. Sawatzky, and H. Petersen. Oxygen 1*s* x-ray-absorption edges of transition-metal oxides. *Phys. Rev. B*, 40:5715–5723, 1989.

[23] J. Zaanen, G. A. Sawatzky, and J. W. Allen. Band gaps and electronic structure of transition-metal compounds. *Phys. Rev. Lett.*, 55:418–421, 1985.

[24] C. J. Ballhausen. *Introduction to Ligand Field Theory*. McGraw-Hill Book Co., 1962.

[25] S. Sugano, Y. Tanabe, and H. Kamimura. *Multiplets of Transition-Metal Ions in Crystals*. Academic Press, Inc., 1970.

[26] P. A. Cox. *Transition Metal Oxides: An Introduction to their Electronic Structure and Properties*. Oxford University Press, 1992.

[27] W. A. Harrison. *Electronic Structure and the Properties of Solids: The Physics of the Chemical Bond*. W. H. Freeman and Company, 1980.

[28] I. B. Bersuker. *Electronic Structure and the Properties of Transition Metal Compounds*. John Wiley & Sons, Inc., 2nd edition, 2010.

[29] G. C. Baldwin and D. W. Kerst. Origin of synchrotron radiation. *Physics Today*, 28(1):9–11, 1975.

[30] A. C. Thompson, D. T. Attwood, E. M. Gullikson, M. R. Howells, J. B. Kortright, A. L. Robinson, J. H. Underwood, K.-J. Kim, J. Kirz, I. Lindau, P. Pianetta, H. Winick, G. P. Williams, and J. H. Scofield. *X-Ray Data Booklet*. Lawrence Berkeley National Labratory, 2009.

[31] G. Sagnac. Relations des rayons x et de leurs rayons secondaires avec la matiere et l'electricite (Relations of x-rays and secondary rays with matter and electricity). *Ann. Chim. Phys.*, 23:145–198, 1901.

[32] R. Stumm von Bordwehr. A history of x-ray absorption fine structure. *Ann. Phys. (Paris)*, 14(4):377–465, 1989.

[33] C. G. Barkla. On x-rays and the theory of radiation. *Philos. Trans. R. Soc. London*, A217:315–360, 1918.

[34] M. Inokuti and T. Noguchi. Why do you call the innermost atomic electron a K electron? *Am. J. Phys.*, 42:1118–1119, 1974.

[35] R. W. Johnston and D. H. Tomboulian. Absorption spectrum of beryllium in the neighborhood of the K edge. *Phys. Rev.*, 94:1585–1589, 1954.

[36] J. Stöhr. *NEXAFS Spectroscopy*. Springer-Verlag, 1992.

[37] H. Ebert, J. Stöhr, S. S. P. Parkin, M. Samant, and A. Nilsson. L–edge x-ray absorption in fcc and bcc Cu metal: Comparison of experimental and first-principles theoretical results. *Phys. Rev. B*, 53:16067–16073, 1996.

[38] F. M. F. de Groot. Multiplet effects in x-ray spectroscopy. *Coord. Chem. Rev.*, 249(1-2):31–63, 2005.

[39] R. Laskowski and P. Blaha. Understanding the $L_{2,3}$ x-ray absorption spectra of early $3d$ transition elements. *Phys. Rev. B*, 82:205104, 2010.

[40] J. Fink, Th. Müller-Heinzerling, B. Scheerer, W. Speier, F. U. Hillebrecht, J. C. Fuggle, J. Zaanen, and G. A. Sawatzky. *2p* absorption spectra of the *3d* elements. *Phys. Rev. B*, 32:4899–4904, 1985.

[41] G. van der Laan, J. Zaanen, G. A. Sawatzky, R. Karnatak, and J.-M. Esteva. Comparison of x-ray absorption with x-ray photoemission of nickel dihalides and NiO. *Phys. Rev. B*, 33:4253–4263, 1986.

[42] B. T. Thole, R. D. Cowan, G. A. Sawatzky, J. Fink, and J. C. Fuggle. New probe for the ground-state electronic structure of narrow-band and impurity systems. *Phys. Rev. B*, 31:6856–6858, 1985.

[43] G. van der Laan, B. T. Thole, G. A. Sawatzky, and M. Verdaguer. Multiplet structure in the $L_{2,3}$ x-ray-absorption spectra: A fingerprint for high- and low-spin Ni^{2+} compounds. *Phys. Rev. B*, 37:6587–6589, 1988.

[44] E. Z. Kurmaev, R. G. Wilks, A. Moewes, L. D. Finkelstein, S. N. Shamin, and J. Kuneš. Oxygen x-ray emission and absorption spectra as a probe of the electronic structure of strongly correlated oxides. *Phys. Rev. B*, 77:165127, 2008.

[45] F. M. F. de Groot, J. Faber, J. J. M. Michiels, M. T. Czyżyk, M. Abbate, and J. C. Fuggle. Oxygen $1s$ x-ray absorption of tetravalent titanium oxides: A comparison with single-particle calculations. *Phys. Rev. B*, 48:2074–2080, 1993.

[46] T. Mazza, P. Piseri, G. Bongiorno, L. Ravagnan, M. Amati, M. Devetta, C. Lenardi, M. Coreno, M. Simone, and P. Milani. Probing the chemical reactivity of free titanium clusters by x-ray absorption spectroscopy. *Appl. Phys. A*, 92(3):463–471, 2008.

[47] A. J. Achkar, T. Z. Regier, H. Wadati, Y.-J. Kim, H. Zhang, and D. G. Hawthorn. Bulk sensitive x-ray absorption spectroscopy free of self-absorption effects. *Phys. Rev. B*, 83:081106, 2011.

[48] A. J. Achkar, T. Z. Regier, E. J. Monkman, K. M. Shen, and D. G. Hawthorn. Determination of total x-ray absorption coefficient using non-resonant x-ray emission. *Sci. Rep.*, 3:182, 2013.

[49] A. Kotani and S. Shin. Resonant inelastic x-ray scattering spectra for electrons in solids. *Rev. Mod. Phys.*, 73:203–246, 2001.

[50] L. J. P. Ament, M. van Veenendaal, T. P. Devereaux, J. P. Hill, and J. van den Brink. Resonant inelastic x-ray scattering studies of elementary excitations. *Rev. Mod. Phys.*, 83:705–767, 2011.

[51] R. P. Feynman. *QED: The Strange Theory of Light and Matter*. Princeton University Press, 1985.

[52] G. Ghiringhelli, M. Matsubara, C. Dallera, F. Fracassi, R. Gusmeroli, A. Piazzalunga, A. Tagliaferri, N. B. Brookes, A. Kotani, and L. Braicovich. NiO as a test case for high resolution resonant inelastic soft x-ray scattering. *J. Phys.: Condens. Matter.*, 17(35):5397, 2005.

[53] S. M. Butorin, J.-H. Guo, M. Magnuson, P. Kuiper, and J. Nordgren. Low-energy d-d excitations in MnO studied by resonant x-ray fluorescence spectroscopy. *Phys. Rev. B*, 54:4405–4408, 1996.

[54] F. M. F. de Groot and A. Kotani. *Core Level Spectroscopy of Solids*. CRC Press, Taylor & Francis Group, 2008.

[55] Ü. Özgür, Ya. I. Alivov, C. Liu, A. Teke, M. A. Reshchikov, S. Doğan, V. Avrutin, S.-J. Cho, and H. Morkoç. A comprehensive review of ZnO materials and devices. *J. Appl. Phys.*, 98(4):041301, 2005.

[56] S. Eisebitt, T. Böske, J.-E. Rubensson, and W. Eberhardt. Determination of absorption coefficients for concentrated samples by fluorescence detection. *Phys. Rev. B*, 47:14103–14109, Jun 1993.

[57] F. M. F. de Groot, M. A. Arrio, Ph. Sainctavit, Ch. Cartier, and C. T. Chen. Fluorescence yield detection: Why it does not measure the x-ray absorption cross section. *Solid State Commun.*, 92(12):991 – 995, 1994.

[58] T. Regier, J. Krochak, T. K. Sham, Y. F. Hu, J. Thompson, and R. I. R. Blyth. Performance and capabilities of the Canadian Dragon: The SGM beamline at the Canadian Light Source. *Nucl. Instrum. Methods Phys. Res., Sect. A*, 582(1):93–95, 2007.

[59] J. J. Jia, T. A. Callcott, J. Yurkas, A. W. Ellis, F. J. Himpsel, M. G. Samant, J. Stohr, D. L. Ederer, J. A. Carlisle, E. A. Hudson, L. J. Terminello, D. K. Shuh, and R. C. C. Perera. First experimental results from IBM/TENN/TULANE/LLNL/LBL undulator beamline at the Advanced Light Source. *Rev. Sci. Instrum.*, 66:1394–1397, 1995.

[60] P. A. M. Dirac. Quantum mechanics of many-electron systems. *P. R. Soc. Lond. A - Conta.*, 123(792):714–733, 1929.

[61] C. Brouder. Angular dependence of x-ray absorption spectra. *J. Phys.: Cond. Matter*, 2(3):701, 1990.

[62] F. M. F. de Groot. X-ray absorption and dichroism of transition metals and their compounds. *J. Electron. Spectrosc. Relat. Phenom.*, 67(4):529 – 622, 1994.

[63] J. J. Sakurai. *Advanced Quantum Mechanics*. Addison-Wesley Publishing, 1967.

[64] O. Gunnarsson and K. Schönhammer. Electron spectroscopies for Ce compounds in the impurity model. *Phys. Rev. B*, 28:4315–4341, 1983.

[65] E. Dagotto. Correlated electrons in high-temperature superconductors. *Rev. Mod. Phys.*, 66:763–840, 1994.

[66] P. Ferriani. *Resonant Inelastic X-ray Scattering and Magnetic Circular Dichroism from 3d Transition Metals*. PhD thesis, University of Modena and Reggio Emilia, 2003.

[67] J. Tulkki and T. Aberg. Statistical theory of electronic Raman resonance scattering by oriented atoms. *J. Phys. B: At. Mol. Phys.*, 13(17):3341, 1980.

[68] J. Tulkki and T. Aberg. Behaviour of Raman resonance scattering across the K x-ray absorption edge. *J. Phys. B: At. Mol. Phys.*, 15(13):L435, 1982.

[69] F. M. F. de Groot, M. Abbate, J. van Elp, G. A. Sawatzky, Y. J. Ma, C. T. Chen, and F. Sette. Oxygen 1s and cobalt 2p x-ray absorption of cobalt oxides. *J. Phys.: Condens. Matter*, 5(14):2277, 1993.

[70] H. Bethe. Thermal division in crystals. *Ann. Phys. (Berlin)*, 3(2):133–208, 1929.

[71] J. H. Van Vleck. Theory of the variations in paramagnetic anisotropy among different salts of the iron group. *Phys. Rev.*, 41:208–215, 1932.

[72] B. T. Thole, G. Van Der Laan, and P. H. Butler. Spin-mixed ground state of Fe phthalocyanine and the temperature-dependent branching ratio in x-ray absorption spectroscopy. *Chem. Phys. Lett.*, 149(3):295 – 299, 1988.

[73] F. M. F. de Groot, J. C. Fuggle, B. T. Thole, and G. A. Sawatzky. $2p$ x-ray absorption of $3d$ transition-metal compounds: An atomic multiplet description including the crystal field. *Phys. Rev. B*, 42:5459–5468, 1990.

[74] M. W. Haverkort. *Spin and orbital degrees of freedom in transition metal oxides and oxide thin films studied by soft x-ray absorption spectroscopy*. PhD thesis, University of Cologne, 2005.

[75] J. Zaanen, C. Westra, and G. A. Sawatzky. Determination of the electronic structure of transition-metal compounds: *2p* x-ray photoemission spectroscopy of the nickel dihalides. *Phy. Rev. B*, 33:8060–8073, 1986.

[76] M. Matsubara, T. Uozumi, A. Kotani, Y. Harada, and S. Shin. Polarization dependence of resonant x-ray emission spectra in early transition metal compounds. *J. Phys. Soc. Jpn.*, 69(5):1558–1565, 2000.

[77] S. G. Chiuzbăian, T. Schmitt, M. Matsubara, A. Kotani, G. Ghiringhelli, C. Dallera, A. Tagliaferri, L. Braicovich, V. Scagnoli, N. B. Brookes, U. Staub, and L. Patthey. Combining M- and L-edge resonant inelastic x-ray scattering for studies of $3d$ transition metal compounds. *Phys. Rev. B*, 78:245102, 2008.

[78] G. Ghiringhelli, M. Matsubara, C. Dallera, F. Fracassi, A. Tagliaferri, N. B. Brookes, A. Kotani, and L. Braicovich. Resonant inelastic x-ray scattering of MnO : $L_{2,3}$ edge measurements and assessment of their interpretation. *Phys. Rev. B*, 73(3):035111, 2006.

[79] M. Magnuson, S. Butorin, J. H. Guo, and J. Nordgren. Electronic structure investigation of CoO by means of soft x-ray scattering. *Phys. Rev. B*, 65(20):205106, 2002.

[80] M. Magnuson, S. M. Butorin, A. Agui, and J. Nordgren. Resonant soft x-ray Raman scattering of NiO. *J. Phys.: Condens. Matter*, 14(13):3669, 2002.

[81] C. Lanczos. An iteration method for the solution of the eigenvalue problem of linear differential and integral operators. *J. Res. Nat. Bur. Stand.*, 45(4):255–282, 1950.

[82] G. Meurant. *The Lanczos and Conjugate Gradient Algorithms*. SIAM, Philadelphia, PA, 2006.

[83] J. K. Cullum and R. A. Willoughby. *Lanczos Algorithms for Large Symmetric Eigenvalue Computations*, volume 1. Birkhäuser Boston, Inc., 1986.

[84] A. Weiße, G. Wellein, A. Alvermann, and H. Fehske. The kernel polynomial method. *Rev. Mod. Phys.*, 78:275–306, 2006.

[85] Z. Bai, J. Demmel, J. Dongarra, A. Ruhe, and H. van der Vorst, editors. *Templates for the Solution of Algebraic Eigenvalue Problems: A Practical Guide*. SIAM, Philadelphia, PA, 2000. http://web.eecs.utk.edu/ dongarra/etemplates/book.html.

[86] A. Tanaka and T. Jo. Resonant $3d$, $3p$ and $3s$ photoemission in transition metal oxides predicted at $2p$ threshold. *J. Phys. Soc. Jpn.*, 63(7):2788–2807, 1994.

[87] E. Stavitski and F. M.F. de Groot. The CTM4XAS program for EELS and XAS spectral shape analysis of transition metal L edges. *Micron*, 41(7):687 – 694, 2010.

[88] E. Anderson, Z. Bai, C. Bischof, S. Blackford, J. Demmel, J. Dongarra, J. Du Croz, A. Greenbaum, S. Hammarling, A. McKenney, and D. Sorensen. *LAPACK Users' Guide*. SIAM, Philadelphia, PA, third edition, 1999.

[89] H. Hamilton. Brains that click. *Popular Mechanics*, 91(3):162, 1949.

[90] R. R. Nair, I.-L. Tsai, M. Sepioni, O. Lehtinen, J. Keinonen, A. V. Krasheninnikov, A. H. Castro Neto, M. I. Katsnelson, A. K. Gaim, and I. V. Grigorieva. Dual origin of defect magnetism in graphene and its reversible switching by molecular doping. *Nature Commun.*, 4:2010, 2013.

[91] J. E. Moore. The birth of topological insulators. *Nature*, 464(7286):194–198, 2010.

[92] H. Ohno. Making nonmagnetic semiconductors ferromagnetic. *Science*, 281(5379):951–956, 1998.

[93] S. B. Ogale. Dilute doping, defects, and ferromagnetism in metal oxide systems. *Adv. Mater.*, 22(29):3125–3155, 2010.

[94] T. Story, R. R. Gałązka, R. B. Frankel, and P. A. Wolff. Carrier-concentration induced ferromagnetism in PbSnMnTe. *Phys. Rev. Lett.*, 56:777–779, 1986.

[95] H. Ohno, A. Shen, F. Matsukura, A. Oiwa, A. Endo, S. Katsumoto, and Y. Iye. (Ga,Mn)As: A new diluted magnetic semiconductor based on GaAs. *Appl. Phys. Lett.*, 69(3):363–365, 1996.

[96] T. Dietl, H. Ohno, F. Matsukura, J. Cibert, and D. Ferrand. Zener model description of ferromagnetism in zinc-blende magnetic semiconductors. *Science*, 287(5455):1019–1022, 2000.

[97] Y. Matsumoto, M. Murakami, T. Shono, T. Hasegawa, T. Fukumura, M. Kawasaki, P. Ahmet, T. Chikyow, S.-Y. Koshihara, and H. Koinuma. Room-temperature ferromagnetism in transparent transition metal-doped titanium dioxide. *Science*, 291(5505):854–856, 2001.

[98] P. Sharma, A. Gupta, K. V. Rao, F. J. Owens, R. Sharma, R. Ahuja, J. M. O. Guillen, B. Johansson, and G. A. Gehring. Ferromagnetism above room temperature in bulk and transparent thin films of Mn-doped ZnO. *Nature Mater.*, 2(10):673–677, 2003.

[99] T. Fukumura, Z. Jin, M. Kawasaki, T. Shono, T. Hasegawa, S. Koshihara, and H. Koinuma. Magnetic properties of Mn-doped ZnO. *Appl. Phys. Lett.*, 78(7):958–960, 2001.

[100] X. M. Cheng and C. L. Chien. Magnetic properties of epitaxial Mn-doped ZnO thin films. *J. Appl. Phys.*, 93(10):7876–7878, 2003.

[101] S.-J. Han, T.-H. Jang, Y.-B. Kim, B.-G. Park, J.-H. Park, and Y. H. Jeong. Magnetism in Mn-doped ZnO bulk samples prepared by solid state reaction. *Appl. Phys. Lett.*, 83(5):920–922, 2003.

[102] S. W. Jung, S.-J. An, G.-C. Yi, C. U. Jung, S.-L. Lee, and S. Cho. Ferromagnetic properties of $Zn_{1-x}Mn_xO$ epitaxial thin films. *Appl. Phys. Lett.*, 80(24):4561–4563, 2002.

[103] M. H. Kane, K. Shalini, C. J. Summers, R. Varatharajan, J. Nause, C. R. Vestal, Z. J. Zhang, and I. T. Ferguson. Magnetic properties of bulk $Zn_{1-x}Mn_xO$ and $Zn_{1-x}Co_xO$ single crystals. *J. Appl. Phys.*, 97(2):023906, 2005.

[104] D. W. Abraham, M. M. Frank, and S. Guha. Absence of magnetism in hafnium oxide films. *Appl. Phys. Lett.*, 87(25):252502, 2005.

[105] J. M. D. Coey, P. Stamenov, R. D. Gunning, M. Venkatesan, and K. Paul. Ferromagnetism in defect-ridden oxides and related materials. *New J. Phys.*, 12(5):053025, 2010.

[106] M. A. Garcia, E. Fernandez Pinel, J. de la Venta, A. Quesada, V. Bouzas, J. F. Fernández, J. J. Romero, M. S. Martín González, and J. L. Costa-Krämer. Sources of experimental errors in the observation of nanoscale magnetism. *J. Appl. Phys.*, 105(1):013925, 2009.

[107] P. V. Radovanovic and D. R. Gamelin. High-temperature ferromagnetism in Ni^{2+}-doped ZnO aggregates prepared from colloidal diluted magnetic semiconductor quantum dots. *Phys. Rev. Lett.*, 91:157202, 2003.

[108] J. D. Bryan, S. M. Heald, S. A. Chambers, and D. R. Gamelin. Strong room-temperature ferromagnetism in Co^{2+}-doped TiO_2 made from colloidal nanocrystals. *J. Am. Chem. Soc.*, 126(37):11640–11647, 2004. PMID: 15366911.

[109] T. C. Kaspar, S. M. Heald, C. M. Wang, J. D. Bryan, T. Droubay, V. Shutthanandan, S. Thevuthasan, D. E. McCready, A. J. Kellock, D. R. Gamelin, and S. A. Chambers. Negligible magnetism in excellent structural quality $Cr_xTi_{1-x}O_2$ anatase: Contrast with high-T_c ferromagnetism in structurally defective $Cr_xTi_{1-x}O_2$. *Phys. Rev. Lett.*, 95:217203, Nov 2005.

[110] W. Xu, Y. Zhou, X. Zhang, D. Chen, Y. Xie, T. Liu, W. Yan, and S. Wei. Local structures of mn in dilute magnetic semiconductor znmno. *Solid State Commun.*, 141(7):374–377, 2007.

[111] A. Bouaine, R. J. Green, S. Colis, P. Bazylewski, G. S. Chang, A. Moewes, E. Z. Kurmaev, and A. Dinia. Appearance of ferromagnetism in Co-doped CeO_2 diluted magnetic semiconductors prepared by solid-state reaction. *J. Phys. Chem. C*, 115(5):1556–1560, 2011.

[112] M. O. Krause and J. H. Oliver. Natural widths of atomic K-levels and L-levels, K-alpha x-ray lines and several KLL Auger lines. *J. Phys. Chem. Ref. Data*, 8(2):329–338, 1979.

[113] S. P. Cramer, F. M. F. De Groot, Y. Ma, C. T. Chen, F. Sette, C. A. Kipke, D. M. Eichhorn, M. K. Chan, and W. H. and Armstrong. Ligand field strengths and oxidation states from manganese L-edge spectroscopy. *J. Am. Chem. Soc.*, 113(21):7937–7940, 1991.

[114] R. J. Green, G. S. Chang, X. Y. Zhang, A. Dinia, E. Z. Kurmaev, and A. Moewes. Identifying local dopant structures and their impact on the magnetic properties of spintronic materials. *Phys. Rev. B*, 83:115207, 2011.

[115] R. W. G. Wyckoff. *Crystal Stuctures 1.* Interscience Publishers, New York, New York, 1963.

[116] T. Jo and T. Shishidou. Orbital magnetic moments of CoO and FeO and isotropic Co and Fe $L_{2,3}$ absorption spectroscopy. *J. Phys. Soc. Jpn.*, 67:2505–2509, 1998.

[117] X.-H. Xu, F.-X. Jiang, J. Zhang, X.-C. Fan, H.-S. Wu, and G. A. Gehring. Magnetic and transport properties of n-type Fe-doped In_2O_3 ferromagnetic thin films. *Appl. Phys. Lett.*, 94(21):212510, 2009.

[118] F.-X. Jiang, X.-H. Xu, J. Zhang, X.-C. Fan, H.-S. Wu, M. Alshammari, Q. Feng, H. J. Blythe, D. S. Score, K. Addison, M. Al-Qahtani, and G. A. Gehring. Room temperature ferromagnetism in metallic and insulating $(In_{1-x}Fe_x)_2o_3$ thin films. *J. Appl. Phys.*, 109(5):053907, 2011.

[119] T. J. Regan, H. Ohldag, C. Stamm, F. Nolting, J. Lüning, J. Stöhr, and R. L. White. Chemical effects at metal/oxide interfaces studied by x-ray-absorption spectroscopy. *Phys. Rev. B*, 64:214422, 2001.

[120] S. Qi, F. Jiang, J. Fan, H. Wu, S. B. Zhang, G. A. Gehring, Z. Zhang, and X. Xu. Carrier-mediated nonlocal ferromagnetic coupling between local magnetic polarons in Fe-doped In_2O_3 and Co-doped ZnO. *Phys. Rev. B*, 84:205204, Nov 2011.

[121] G. Ciatto, A. Di Trolio, E. Fonda, P. Alippi, A. M. Testa, and A. Amore Bonapasta. Evidence of cobalt-vacancy complexes in $Zn_{1-x}Co_xO$ dilute magnetic semiconductors. *Phys. Rev. Lett.*, 107(12):127206, 2011.

[122] T. Haupricht, R. Sutarto, M. W. Haverkort, H. Ott, A. Tanaka, H. H. Hsieh, H.-J. Lin, C. T. Chen, Z. Hu, and L. H. Tjeng. Local electronic structure of Fe^{2+} impurities in MgO thin films: Temperature-dependent soft x-ray absorption spectroscopy study. *Phys. Rev. B*, 82:035120, 2010.

[123] J. M. D. Coey, M. Venkatesan, and C. B. Fitzgerald. Donor impurity band exchange in dilute ferromagnetic oxides. *Nature Mater.*, 4(2):173–179, 2005.

[124] L. F. J. Piper, A. DeMasi, S. W. Cho, K. E. Smith, F. Fuchs, F. Bechstedt, C. Körber, A. Klein, D. J. Payne, and R. G. Egdell. Electronic structure of In_2O_3 from resonant x-ray emission spectroscopy. *Appl. Phys. Lett.*, 94(2):022105, 2009.

[125] A. Walsh, J. L. F. Da Silva, S.-H. Wei, C. Körber, A. Klein, L. F. J. Piper, A. DeMasi, K. E. Smith, G. Panaccione, P. Torelli, D. J. Payne, A. Bourlange, and R. G. Egdell. Nature of the band gap of In_2O_3 revealed by first-principles calculations and x-ray spectroscopy. *Phys. Rev. Lett.*, 100:167402, 2008.

[126] S Eisebitt and W Eberhardt. Band structure information and resonant inelastic soft x-ray scattering in broad band solids. *J. Electron Spectrosc. Relat. Phenom.*, 110(1-3, SI):335–358, 2000.

[127] J. D. Newton. *Uncommon Friends: Life with Thomas Edison, Henry Ford, Harvey Firestone, Alexis Carrel, and Charles Lindbergh.* Harcourt Brace Jovanovich, 1987.

[128] R. Long and N. J. English. Band gap engineering of double-cation-impurity-doped anatase-titania for visible-light photocatalysts: a hybrid density functional theory approach. *Phys. Chem. Chem. Phys.*, 13:13698–13703, 2011.

[129] A. Fujishima and K. Honda. Electrochemical photolysis of water at a semiconductor electrode. *Nature*, 238(5358):37–38, 1972.

[130] A. J. Bard and M. A. Fox. Artificial photosynthesis: Solar splitting of water to hydrogen and oxygen. *Accounts of Chemical Research*, 28(3):141–145, 1995.

[131] P. D. C. King, T. D. Veal, F. Fuchs, Ch. Y. Wang, D. J. Payne, A. Bourlange, H. Zhang, G. R. Bell, V. Cimalla, O. Ambacher, R. G. Egdell, F. Bechstedt, and C. F. McConville. Band gap, electronic structure, and surface electron accumulation of cubic and rhombohedral In_2O_3. *Phys. Rev. B*, 79:205211, 2009.

[132] S. C. Cheng. Coordination and optical attenuation of TiO_2–SiO_2 glass by electron energy loss spectroscopy. *J. Non-Cryst. Solids*, 354(31):3735 – 3741, 2008.

[133] G. S. Henderson, X. Liu, and M. E. Fleet. Titanium coordination in silicate glasses investigated using O K-edge x-ray absorption spectroscopy. *Mineral. Mag.*, 67(4):597–607, 2003.

[134] G. S. Henderson, X. Liu, and M. E. Fleet. A Ti L-edge x-ray absorption study of Ti-silicate glasses. *Phys. Chem. Minerals*, 29(1):32–42, 2002.

[135] C. F. Song, M. K. Lu, P. Yang, D. Xu, and D. R. Yuan. Study on the photoluminescence properties of sol-gel Ti^{3+} doped silica glasses. *J. Sol-Gel Sci. Technol.*, 25(2):113–119, 2002.

[136] M. W. Gaultois and A. P. Grosvenor. XANES and XPS investigations of $(TiO2)_x(SiO2)_{1-x}$: the contribution of final-state relaxation to shifts in absorption and binding energies. *J. Mater. Chem.*, 21:1829–1836, 2011.

[137] V. F. Lebedev, V. V. Koltashev, E. B. Kryukova, V. G. Plotnichenko, and A. O. Rybaltovsky. Luminescence, Raman, and ESR spectroscopy of Ti doped SiO_2 hosts. *Phys. Chem. Glasses*, 43C:141–144, 2002.

[138] E. Cattaruzza, G. Mattei, P. Mazzoldi, R. Bertoncello, G. Battaglin, and L. Mirenghi. Formation of amorphous silicide nanoclusters in chromium- and titanium-implanted silica. *Appl. Phys. Lett.*, 67(19):2884–2886, 1995.

[139] V. Belostotsky. Some effects of Ti^+-ion implantation at elevated temperatures and following annealing on optical spectra of silica glass. *J. Non-Cryst. Solids*, 202(12):194 – 197, 1996.

[140] P. Martin, M. Dufour, A. Ermolieff, S. Marthon, F. Pierre, and M. Dupuy. Electrical surface conductivity in quartz induced by ion-implantation. *J. Appl. Phys.*, 72(7):2907–2911, 1992.

[141] Z. Pan, S. H. Morgan, D. O. Henderson, R. H. Magruder III, and R. A. Zuhr. Optical and infrared studies of Ti, Au, O ion implanted fused silica. *Nucl. Instrum. Methods Phys. Res. B*, 114(34):281 – 287, 1996.

[142] J. P. Zhao, Z. Y. Chen, M. Lu, and J. W. Rabalais. Linear optical properties of a Ti-SiO_2 nanoparticle composite. *J. Appl. Phys.*, 93(1):566–575, 2003.

[143] J. F. Ziegler, J. P. Biersack, and M. D. Ziegler. The stopping and range of ions in matter: Electronic manual for SRIM program. 2009.

[144] F. M. F. de Groot, J. C. Fuggle, B. T. Thole, and G. A. Sawatzky. $L_{2,3}$ x-ray-absorption edges of d^0 compounds: K^+, Ca^{2+}, Sc^{3+}, and Ti^{4+} in O_h (octahedral) symmetry. *Phys. Rev. B*, 41:928–937, 1990.

[145] R. J. Green, D. A. Zatsepin, A. Hunt, E. Z. Kurmaev, N. V. Gavrilov, and A. Moewes. The formation of Ti–O tetrahedra and band gap reduction in SiO_2 via pulsed ion implantation. *J. Appl. Phys.*, 113(10):103704, 2013.

[146] F. M. F. Groot, M. O. Figueiredo, M. J. Basto, M. Abbate, H. Petersen, and J. C. Fuggle. 2p x-ray absorption of titanium in minerals. *Phys. Chem. Minerals*, 19(3):140–147, 1992.

[147] P. Krüger. Multichannel multiple scattering calculation of $L_{2,3}$-edge spectra of $TiO_2$and $SrTiO_3$: Importance of multiplet coupling and band structure. *Phys. Rev. B*, 81:125121, 2010.

[148] J. P. Crocombette and F. Jollet. Ti 2p x-ray absorption in titanium dioxides (TiO_2): the influence of the cation site environment. *J. Phys.: Cond. Matter*, 6(49):10811, 1994.

[149] Z. L. Wang. Zinc oxide nanostructures: growth, properties and applications. *J. Phys.: Cond. Matter*, 16(25):R829, 2004.

[150] A. Ohtomo, K. Tamura, M. Kawasaki, T. Makino, Y. Segawa, Z. K. Tang, G. K. L. Wong, Y. Matsumoto, and H. Koinuma. Room-temperature stimulated emission of excitons in ZnO/(Mg, Zn)O superlattices. *Appl. Phys. Lett.*, 77(14):2204–2206, 2000.

[151] G. Pei, C. Xia, S. Cao, J. Zhang, F. Wu, and J. Xu. Synthesis and magnetic properties of Ni-doped zinc oxide powders. *J. Magn. Magn. Mater.*, 302(2):340 – 342, 2006.

[152] L. Arda, M. Acikgoz, and A. Gungor. Magnetic and microstructure properties of Ni-doped ZnO films and powder by sol-gel process. *J. Supercond. Nov. Magn.*, 25(8):2701–2705, 2012.

[153] X. Wang, L. Zhu, L. Zhang, J. Jiang, Z. Yang, Z. Ye, and B. He. Properties of Ni doped and Ni–Ga co-doped ZnO thin films prepared by pulsed laser deposition. *J. Alloys Compd.*, 509(7):3282 – 3285, 2011.

[154] S. C. Das, R. J. Green, J. Podder, T. Z. Regier, G. S. Chang, and A. Moewes. Band gap tuning in ZnO through Ni doping via spray pyrolysis. *J. Phys. Chem. C*, 117(24):12745–12753, 2013.

[155] R. Chauhan, A. Kumar, and R. Chaudhary. Structures and optical properties of $Zn_{1-x}Ni_xO$ nanoparticles by coprecipitation method. *Res. Chem. Intermed.*, 38:1483–1493, 2012.

[156] C. L. Dong, C. Persson, L. Vayssieres, A. Augustsson, T. Schmitt, M. Mattesini, R. Ahuja, C. L. Chang, and J.-H. Guo. Electronic structure of nanostructured ZnO from x-ray absorption and emission spectroscopy and the local density approximation. *Phys. Rev. B*, 70:195325, Nov 2004.

[157] M. W. Haverkort, M. Zwierzycki, and O. K. Andersen. Multiplet ligand-field theory using Wannier orbitals. *Phys. Rev. B*, 85:165113, 2012.

[158] M. Launay and R. Dronskowski. A theoretical study on the existence and structures of some hypothetical first-row transition-metal M(NCN) compounds. *Z. Naturforsch. B Chem.*, 60(4):437–448, 2005.

[159] X. Liu, M. Krott, P. Muller, C. Hu, H. Lueken, and R. Dronskowski. Synthesis, crystal structure, and properties of MnNCN, the first carbodiimide of a magnetic transition metal. *Inorg. Chem.*, 44(9):3001–3003, 2005.

[160] X. H. Liu, M. A. Wankeu, H. Lucken, and R. Dronskowski. A novel method for synthesizing crystalline copper carbodiimide, CuNCN. Structure determination by x-ray Rietveld refinement. *Z. Naturforsch. B Chem.*, 60(6):593–596, 2005.

[161] M. Krott, X. Liu, B. P. T. Fokwa, M. Speldrich, H. Lueken, and R. Dronskowski. Synthesis, crystal-structure determination and magnetic properties of two new transition-metal carbodiimides: CoNCN and NiNCN. *Inorg. Chem.*, 46(6):2204–2207, 2007.

[162] X. Liu, L. Stork, M. Speldrich, H. Lueken, and R. Dronskowski. FeNCN and $Fe(NCNH)_2$: Synthesis, structure, and magnetic properties of a nitrogen-based pseudo-oxide and -hydroxide of divalent iron. *Chem. Eur. J.*, 15(7):1558–1561, 2009.

[163] X. Tang, H. Xiang, X. Liu, M. Speldrich, and R. Dronskowski. A ferromagnetic carbodiimide: $Cr_2(NCN)_3$. *Angew. Chem. Int. Ed.*, 49(28):4738–4742, 2010.

[164] X. Liu, R. Dronskowski, R. Glaum, and A. L. Tchougreff. Experimental and quantum-chemical investigations of the UV/Vis absorption spectrum of manganese carbodiimide, MnNCN. *Z. Anorg. Allg. Chem.*, 636(2):343–348, 2010.

[165] J. van Elp, R. H. Potze, H. Eskes, R. Berger, and G. A. Sawatzky. Electronic structure of MnO. *Phys. Rev. B*, 44:1530–1537, 1991.

[166] T. D. Boyko, R. J. Green, R. Dronskowski, and A. Moewes. Electronic band gap reduction in manganese carbodiimide: MnNCN. *J. Phys. Chem. C*, 117(24):12754–12761, 2013.

[167] A. Koestler and J. R. Smithies. *Beyond Reductionism.* Hutchinson, London, 1958.

[168] R. Kurian, K. Kunnus, P. Wernet, S. M. Butorin, P. Glatzel, and de Groot F. M. F. Intrinsic deviations in fluorescence yield detected x-ray absorption spectroscopy: The case of the transition metal $L_{2,3}$ edges. *J. Phys.: Condens. Matter*, 24(45):452201, 2012.

[169] M. van Veenendaal, J. B. Goedkoop, and B. T. Thole. Polarized x-ray fluorescence as a probe of ground state properties. *Phys. Rev. Lett.*, 77:1508–1511, 1996.

[170] J. B. Goedkoop, N. B. Brookes, M. van Veenendaal, and B. T. Thole. Soft x-ray fluorescence yield XMCD sum rules. *J. Electron. Spectrosc. Relat. Phenom.*, 86(13):143 – 150, 1997.

[171] V. R. Singh, K. Ishigami, V. K. Verma, G. Shibata, Y. Yamazaki, T. Kataoka, A. Fujimori, F.-H. Chang, D.-J. Huang, H.-J. Lin, C. T. Chen, Y. Yamada, T. Fukumura, and M. Kawasaki. Ferromagnetism of cobalt-doped anatase TiO_2 studied by bulk- and surface-sensitive soft x-ray magnetic circular dichroism. *Appl. Phys. Lett.*, 100(24):242404, 2012.

[172] E. F. Aziz, M. H. Rittmann-Frank, K. M. Lange, S. Bonhommeau, and M. Chergui. Charge transfer to solvent identified using dark channel fluorescence-yield L-edge spectroscopy. *Nat. Chem.*, 2(10):853–857, 2010.

[173] F. M. F. de Groot. Dips and peaks in fluorescence yield x-ray absorption are due to state-dependent decay. *Nat. Chem.*, 4(10):766–767, 2012.

[174] T. Z. Regier, A. J. Achkar, D. Peak, J. S. Tse, and D. G. Hawthorn. Dark channel fluorescence observations result from concentration effects rather than solvent-solute charge transfer. *Nat. Chem.*, 4(10):765–766, 2012.

[175] H. A. Jahn and E. Teller. Stability of polyatomic molecules in degenerate electronic states. I. orbital degeneracy. *Proc. R. Soc. Lond. A*, 161(905):220–235, 1937.

[176] F. Hund. *Linienspektren und Periodisches System der Elemente*. Number 4 in Linienspektren und periodisches System der Elemente. Julius Springer, 1927.

[177] G. Ghiringhelli, A. Piazzalunga, X. Wang, A. Bendounan, H. Berger, F. Bottegoni, N. Christensen, C. Dallera, M. Grioni, J.-C. Grivel, M. Moretti Sala, L. Patthey, J. Schlappa, T. Schmitt, V. Strocov, and L. Braicovich. Crystal field and low energy excitations measured by high resolution RIXS at the L_3 edge of Cu, Ni and Mn. *Eur. Phys. J. Special Topics*, 169(1):199–205, 2009.

[178] J. Laverock, A. R. H. Preston, D. Newby, K. E. Smith, and S. B. Dugdale. Maximum entropy deconvolution of resonant inelastic x-ray scattering spectra. *Phys. Rev. B*, 84:235111, 2011.

[179] D. A. Varshalovich, A. N. Moskalev, and V. K. Khersonskii. *Quantum Theory of Angular Momentum*. World Scientific, 1988.

Appendix A

Image Correction for RIXS Spectra

The experimental RIXS data collected for this thesis were acquired using an older generation soft x-ray spectrometer. Consequently, the experimental resolution was not as high as that of current leading-edge spectrometers (see Ref. [177] for an example of leading-edge resolution). In many cases, our resolution was only just sufficient to extract the desired information from the *dd* excitations, so every effort was made to attain the best experimental spectra possible with the instrumentation available. Here we describe a technique that was developed during this thesis work to help with this.

As discussed in Chapter 3, soft x-ray RIXS experiments typically make use of diffraction gratings to disperse the x-rays of varying wavelengths which are then counted on an area sensitive detector. An example of an image that one would obtain on such a detector is shown in Figure A.1.[1] The horizontal axis is the energy axis, and by summing the values in the vertical column for each energy, we obtain the normal two dimensional RIXS spectra that were shown in this work. However, in the Figure we see that the spectral lines are slightly curved with respect to the pixel columns of the detector. This curvature is a natural consequence of the optical design of RIXS spectrometers. Such curvature creates a problem as simply summing each vertical column would lead to a blurring of data since spectral lines would contribute to the sums in different columns.

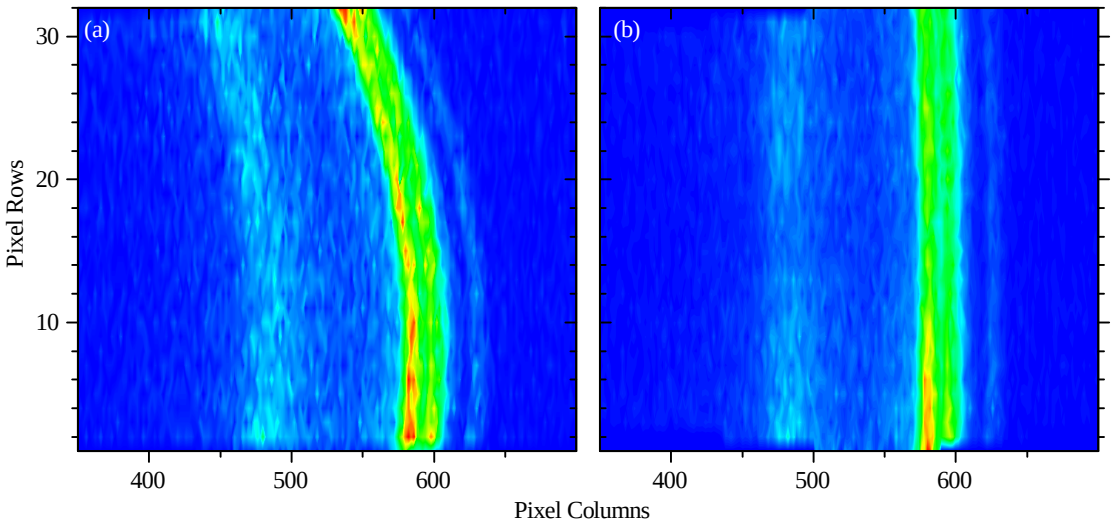

Figure A.1: Raw and corrected RIXS images. (a) The raw image, where the spectral lines are curved due to the detection geometry. (b) The corrected image, obtained by shifting the individual rows of the raw image by a varying amount.

[1] These images are zoomed in slightly to better show the curvature and correction. For an example of an entire (32×1024) RIXS image, see Figure 3.9.

A.1 Shifting Approaches for XES and RIXS Images

To process RIXS data that are subjected to the curvature distortion described above, we take the raw, warped image I with n rows by m columns of pixels and transform it to a corrected image C with the same dimensions. Figure A.1 provides an example of this correction, where a raw image is shown on the left and a corrected image on the right. Note that our corrections are only performed via transformations in the x direction (within rows).

A.1.1 Constant Integer Shifts

The traditional approach is to have one column vector S of length n which contains shift values. The element S_i contains the amount of pixels that the ith row of I has been shifted by due to the experimental setup. The case of constant integer shifts is quite simple to implement. For a given pixel in row i, column j, we have

$$C_{i,j-S_i} = I_{i,j} \tag{A.1}$$

We call this the *constant integer shift* approach because within each row the pixels are shifted by the same constant integer. This is the technique that has been typically used for the data at Beamline 8.0.1 at the Advanced Light Source.

A.1.2 Constant Floating Point Shifts

The constant integer shift approach is adequate when spectral features are spread over large numbers of detector columns. However, when striving for high resolution this is often not the case. Here, it becomes advantageous to be able to shift the raw image over by a non-integer number of pixels. In this case, the shift vector S contains entries which are non-integer. This means that the intensity of a pixel in the raw image I generally gets split into two pixels in the corrected image C. So, with C initialized to be an empty image (zeroes for each entry), we have

$$C_{i,\lfloor j-S_i \rfloor} = C_{i,\lfloor j-S_i \rfloor} + I_{i,j} \times (S_i - \lfloor S_i \rfloor) \tag{A.2}$$

and

$$C_{i,\lceil j-S_i \rceil} = C_{i,\lceil j-S_i \rceil} + I_{i,j} \times (\lceil S_i \rceil - S_i) \tag{A.3}$$

where the standard ceiling ($\lceil\ \rceil$) and floor ($\lfloor\ \rfloor$) operators have been used. Note that this formulation works for both positive and negative values in the shift vector S. Here more than one pixel from the original image can contribute to a particular pixel in the corrected image, which explains the cumulative sum nature of the expressions.

To demonstrate this method, we can consider a simple example using a single row image as shown in Figure A.2. Say we have data in the pixel which is in the 11^{th} column of the i^{th} row of the detector, and consider the case where the shift vector has the element $S_i = -1.2$. Recall this means the data in the i^{th} row is 1.2 columns too low (or to the left in the image) due to the experimental distortions. If we apply the equations, we get

$$C_{i,\lfloor 11-(-1.2) \rfloor} = 0.0 + I_{i,11} \times (-1.2 - \lfloor -1.2 \rfloor) \tag{A.4}$$

and

$$C_{i,\lceil 11-(-1.2) \rceil} = 0.0 + I_{i,11} \times (\lceil -1.2 \rceil - (-1.2)) \tag{A.5}$$

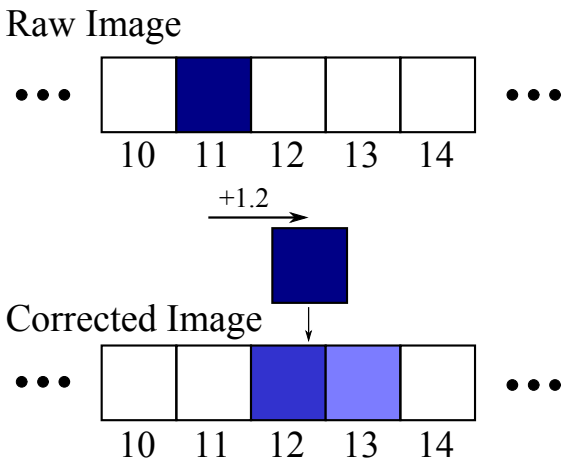

Figure A.2: Example of constant floating point shift correction for a single row of a RIXS image. The data must be shifted by 1.2 pixels, causing the intensity of the original pixel to be split among two pixels in the corrected image.

Simplifying gives

$$C_{i,12} = I_{i,11} \times (0.8) \tag{A.6}$$

and

$$C_{i,13} = I_{i,11} \times (0.2) \tag{A.7}$$

Thus, the intensity from the raw pixel has been split into two pixels due to the fractional shift value, as shown in the Figure. Note that this simple example might suggest the floating point shift technique would blur images, since the data from one pixel is split into two. However, it only appears like this for the simple example of a one-pixel spectrum. When all pixels have data, multiple raw pixels contribute to each corrected pixel, and a blurring of the data does not occur.

A.1.3 Varying Floating Point Shifts

To ensure we obtain the best possible spectra, one final layer of complexity to the shifting can be added. It turns out that generally the amount of shift necessary to correct the images changes not only for different rows on the detector, but also varies slightly across the columns of the detector. In practice it is not generally possible to know the necessary shift amount for each column across the detector, but one can determine shifts to use for columns near opposite sides. This can be done by fitting the curvature to two spectral lines that are on either side of the detector. A linear interpolation between these two fitted sets of shift values can then be made.

The implementation of this approach is very similar to the above implementation for constant floating point shifts, except here we use an interpolated shift value rather than the values stored in a single shift vector S_i. Additionally, we can no longer assume one pixel from the original image will get split into exactly two pixels in the corrected image. This is because the varied shift values mean pixels can be stretched or compressed as they are mapped onto the final image.

Now say we have two shift vectors, $S(x_1)$ and $S(x_2)$ where x_1 and x_2 are the columns that each vector is optimal for. For any given raw data pixel $I_{i,j}$, we need to use the two shift vectors to calculate how many columns the data pixel must be shifted before being added to the final

image, and how many pixels it will contribute to due to floating point shift values and possible stretching/compressing. Our final algorithm for correcting a raw image is then as given on the following page.

The algorithm operates on each pixel of the raw data, breaking it up and adding the fractional intensities from it to pixels in the corrected image which are calculated according to interpolated floating point shift values. We can then sum the rows of the corrected image to obtain a final 2D RIXS spectrum which has the least artificial blurring possible. After this correction, one could also take advantage of the maximum entropy deconvolution to try to actually remove instrumental broadening if desired [178]. A nice program for performing such a deconvolution has been written by fellow research group member Brett Leedahl at the University of Saskatchewan.

Algorithm for varying floating point shift correction of RIXS images

---

· For each row i do

· Calculate the width of stretched pixels for this row:

$$w = \frac{S\left(x_1\right)_i - S\left(x_2\right)_i}{x_1 - x_2} \tag{A.8}$$

· For each column j do

· Calculate a linearly-interpolated shift value for this pixel $I_{i,j}$:

$$\delta = \frac{S\left(x_1\right)_i - S\left(x_2\right)_i}{x_1 - x_2}\left(j - x_1\right) + S\left(x_1\right)_i \tag{A.9}$$

· Calculate the fractional index for the lower edge of this shifted pixel:

$$L = j - \delta - w/2 \tag{A.10}$$

· Calculate the fractional index for the upper edge of this shifted pixel:

$$U = j - \delta + w/2 \tag{A.11}$$

· Set counter $k = L$

· while $k \leq \lceil U \rceil$

· if $k < U$ AND $\lfloor k \rfloor$ is a valid column index then

· if $k < \lceil L \rceil$ then

$$C_{i,\lfloor k \rfloor} \stackrel{+}{=} \frac{|k - \lceil k \rceil|}{U - L} \times I_{i,j} \tag{A.12}$$

· else

$$C_{i,\lfloor k \rfloor} \stackrel{+}{=} \frac{1}{U - L} \times I_{i,j} \tag{A.13}$$

· else

$$C_{i,\lfloor k \rfloor} \stackrel{+}{=} \frac{|U - \lfloor k \rfloor|}{U - L} \times I_{i,j} \tag{A.14}$$

· $k = k + 1$

· end while loop

· end for loop over columns j

· end for loop over rows i

Appendix B

Polarization Vectors and Dipole Transitions

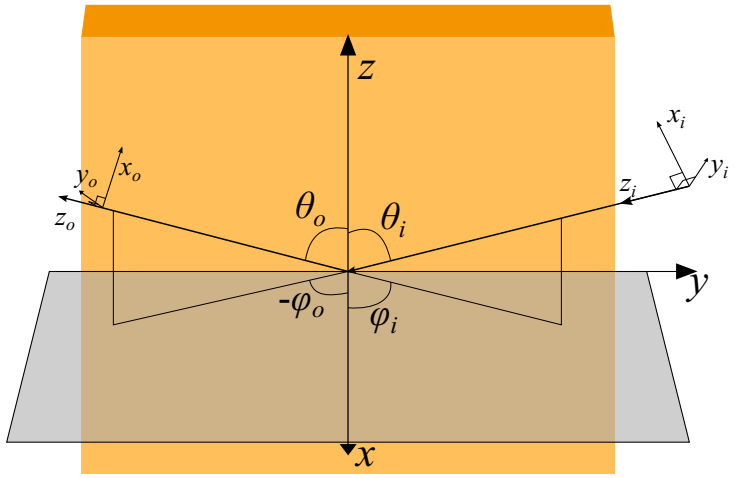

Figure B.1: Geometry definitions for XAS and RIXS. The photon coordinate systems are defined such that the $x_i z$ and $x_o z$ planes are perpendicular to the xy plane.

Here we describe the necessary expressions for the polarization vectors to use in the XAS and RIXS equations of Chapter 4. We consider the general scattering geometry shown in Figure B.1. The coordinates (x, y, z) are for the sample under study, usually coincident with the atomic coordinates for the transition metal atom being probed. The coordinates with index i are for the incident photons (for XAS and RIXS) while the coordinates with index o are for the outgoing photons (for PFY and RIXS).

For synchrotron experiments, we typically have linear or circular polarized light, with nearly 100% polarization. Thus, with respect to the coordinates shown in the Figure, we can define polarization vectors for x linear, y linear, left circular, and right circular polarization in Cartesian (x, y, z) coordinates (in the photon coordinate systems):

$$\boldsymbol{\epsilon}_x = \begin{pmatrix} 1 \\ 0 \\ 0 \end{pmatrix} \qquad \boldsymbol{\epsilon}_y = \begin{pmatrix} 0 \\ 1 \\ 0 \end{pmatrix} \qquad \boldsymbol{\epsilon}_L = \frac{1}{\sqrt{2}} \begin{pmatrix} 1 \\ -i \\ 0 \end{pmatrix} \qquad \boldsymbol{\epsilon}_R = \frac{1}{\sqrt{2}} \begin{pmatrix} -1 \\ -i \\ 0 \end{pmatrix} \tag{B.1}$$

where we have used the handedness convention of Stöhr [15]. Alternatively, in an $\alpha = +1, 0, -1$ spherical basis more compatible with the usual spherical components of the dipole operator, we have

$$\boldsymbol{\epsilon}_x = \frac{1}{\sqrt{2}} \begin{pmatrix} -1 \\ 0 \\ 1 \end{pmatrix} \qquad \boldsymbol{\epsilon}_y = \frac{1}{\sqrt{2}} \begin{pmatrix} i \\ 0 \\ i \end{pmatrix} \qquad \boldsymbol{\epsilon}_L = \begin{pmatrix} 0 \\ 0 \\ -1 \end{pmatrix} \qquad \boldsymbol{\epsilon}_R = \begin{pmatrix} 1 \\ 0 \\ 0 \end{pmatrix} \tag{B.2}$$

where we have given the contravariant components of the vectors [179], since we are interested in calculating $\boldsymbol{\epsilon} \cdot \mathbf{r} = \sum_\alpha \epsilon^\alpha r_\alpha$.

To evaluate the XAS and RIXS expressions, we need to transform these vectors into the atomic coordinate system that the dipole operator is defined in. Our general transformation matrix is

$$\begin{pmatrix} x \\ y \\ z \end{pmatrix} = \begin{pmatrix} -\cos\theta\cos\phi & \sin\phi & \sin\theta\cos\phi \\ -\cos\theta\sin\phi & -\cos\phi & \sin\theta\sin\phi \\ \sin\theta & 0 & \cos\theta \end{pmatrix} \begin{pmatrix} x' \\ y' \\ z' \end{pmatrix} \tag{B.3}$$

where the primed coordinates are those of the photons (i.e. x_i, x_o, etc.). For the emitted photons, we can use $\theta = \theta_o$ and $\phi = \phi_o$ directly in this matrix, whereas for the incident photons, we use $\theta = \pi - \theta_i$ and $\phi = \pi + \phi_i$ (because our geometry has the incident photons travelling toward the origin).

By applying the transformation to the polarization vectors given above, we acquire the proper polarization vectors to use in the XAS and RIXS expressions. Below we provide these vectors, defined in Cartesian and spherical coordinates. The reason that we provide both is that the point group symmetry code that we use (created by Butler and Thole) provides us spherical dipole operator matrix elements for some symmetries (SO_3, O_h, D_{4h}, etc.) and Cartesian dipole operator matrix elements for others (D_{2h}, C_1, etc.). Thus we need to have the proper expressions for polarization vectors in each basis to accommodate these different cases. For reference, we provide the dipole operator expressions as well (though these are handled by the Butler-Thole code).

B.1 Spherical Coordinates

In the spherical basis, the polarization-dependent dipole operator is given by

$$\boldsymbol{\epsilon} \cdot \mathbf{r} = \sum_{\alpha=0,\pm1} \epsilon^\alpha r_\alpha = \epsilon^{+1} r C^{(1)}_{+1}(\hat{\mathbf{r}}) + \epsilon^0 r C^{(1)}_0(\hat{\mathbf{r}}) + \epsilon^{-1} r C^{(1)}_{-1}(\hat{\mathbf{r}}) \tag{B.4}$$

where the $C^{(1)}_\alpha$ are normalized spherical harmonics [15].

Using the transformation matrix as given above, the polarization vectors become

$$\begin{aligned} \boldsymbol{\epsilon}_x &= \begin{pmatrix} \frac{1}{\sqrt{2}}\cos\theta e^{i\phi} \\ \sin\theta \\ -\frac{1}{\sqrt{2}}\cos\theta e^{-i\phi} \end{pmatrix} & \boldsymbol{\epsilon}_L &= \begin{pmatrix} \frac{1}{2}(1+\cos\theta)e^{i\phi} \\ \frac{1}{\sqrt{2}}\sin\theta \\ \frac{1}{2}(1-\cos\theta)e^{-i\phi} \end{pmatrix} \\ \boldsymbol{\epsilon}_y &= \begin{pmatrix} \frac{i}{\sqrt{2}}e^{i\phi} \\ 0 \\ \frac{i}{\sqrt{2}}e^{-i\phi} \end{pmatrix} & \boldsymbol{\epsilon}_R &= \begin{pmatrix} \frac{1}{2}(1-\cos\theta)e^{i\phi} \\ -\frac{1}{\sqrt{2}}\sin\theta \\ \frac{1}{2}(1+\cos\theta)e^{-i\phi} \end{pmatrix} \end{aligned} \tag{B.5}$$

where again $\theta = \theta_o$ or $\pi - \theta_i$ and $\phi = \phi_o$ or $\pi + \phi_i$.

B.2 Cartesian Coordinates

In Cartesian coordinates, the polarization-dependent dipole operator is given by

$$\boldsymbol{\epsilon} \cdot \mathbf{r} = \sum_{\alpha=x,y,z} \epsilon^\alpha r_\alpha = \epsilon^x r_x + \epsilon^y r_y + \epsilon^z r_z \tag{B.6}$$

Again, after applying the transformation matrix, our polarization vectors are

$$\boldsymbol{\epsilon}_x = \begin{pmatrix} -\cos\theta\cos\phi \\ -\cos\theta\sin\phi \\ \sin\theta \end{pmatrix} \qquad \boldsymbol{\epsilon}_L = \frac{1}{\sqrt{2}} \begin{pmatrix} -\cos\theta\cos\phi - i\sin\phi \\ -\cos\theta\sin\phi + i\cos\phi \\ \sin\theta \end{pmatrix}$$

$$\boldsymbol{\epsilon}_y = \begin{pmatrix} \sin\phi \\ -\cos\phi \\ 0 \end{pmatrix} \qquad \boldsymbol{\epsilon}_R = \frac{1}{\sqrt{2}} \begin{pmatrix} \cos\theta\cos\phi - i\sin\phi \\ \cos\theta\sin\phi + i\cos\phi \\ -\sin\theta \end{pmatrix} \tag{B.7}$$

and again we would input $\theta = \theta_o$ or $\pi - \theta_i$ and $\phi = \phi_o$ or $\pi + \phi_i$.

Appendix C

Crystal Field Splitting Energies

Section 4.3.2 provided a diagrammatic description of the effects of various crystal field symmetries on the $3d$ orbitals. The mathematical relations between the commonly used parameters and the single particle energy shifts of the orbitals for each case can be found in the literature [24,54,74], but for convenience we provide them below.

C.1 O_h and T_d Symmetry

The common cases of six-fold octahedral, four-fold tetrahedral, and eight-fold cubic coordination lead to the splitting of the $3d$ orbitals into two groups: the e_g and t_{2g} orbitals.[1] The energy splitting between these groups of orbitals is given by the parameter $10Dq$. For octahedral coordination, $10Dq$ is positive, while for tetrahedral and cubic, it is negative. The specific energies of the orbital groups with respect to the spherically symmetric case are

$$E_{e_g} = 6Dq \tag{C.1}$$
$$E_{t_{2g}} = -4Dq \tag{C.2}$$

C.2 D_{4h} Symmetry

The D_{4h} symmetry case can be viewed as a distortion of the O_h case. Accordingly, the e_g orbital group splits into the b_{1g} and a_{1g} orbitals, while the t_{2g} group splits into the b_{2g} and e_g. The energies are given by

$$E_{b_{1g}} = 6Dq + 2Ds - Dt \tag{C.3}$$
$$E_{a_{1g}} = 6Dq - 2Ds - 6Dt \tag{C.4}$$
$$E_{b_{2g}} = -4Dq + 2Ds - Dt \tag{C.5}$$
$$E_{e_g} = -4Dq - Ds + 4Dt \tag{C.6}$$

C.3 D_{2h} Symmetry

The D_{2h} symmetry case can be viewed as a further distortion from the D_{4h} case. Additionally, the distortion is such that some of the $3d$ orbitals mix and are no longer the pure atomic orbitals. In particular, b_{1g} and a_{1g} orbitals from D_{4h} mix together to form the two a_g groups (see Figure 4.2 for clarity). The b_{2g} orbital from D_{4h} stays at the same energy and is now labelled the b_{1g} orbital, while the e_g orbitals from D_{4h} split in energy to become the b_{2g} and b_{3g} orbitals in D_{2h}. The energies of

[1] Note that for tetrahedral, the g subscript is dropped because we no longer have inversion symmetry.

the orbitals now become

$$E_{a_g} = 6Dq - \frac{7}{2}Ds \pm \sqrt{\Gamma_{a_g}} \tag{C.7}$$

$$E_{b_{1g}} = -4Dq + 2Ds - Dt \tag{C.8}$$

$$E_{b_{2g}} = -4Dq - Ds + 4Dt + Du \tag{C.9}$$

$$E_{b_{3g}} = -4Dq - Ds + 4Dt + Du \tag{C.10}$$

where

$$\Gamma_{a_g} = (4Ds + 5Dt)^2 + 4Dv^2 \tag{C.11}$$

C.4 D_{3d} and C_{3v} Symmetry

The trigonal symmetries can be viewed as distortions from the O_h case. One of the t_{2g} orbitals from the O_h case splits off to become the a_{1g} orbital. The rest mix together to form two e_g groups. The energies are given by

$$E_{e_g} = Dq + \frac{1}{2}D\sigma + \frac{3}{2}D\tau \pm \sqrt{\Gamma_{e_g}} \tag{C.12}$$

$$E_{a_{1g}} = -4Dq - 2D\sigma - 6D\tau \tag{C.13}$$

where

$$\Gamma_{e_g} = 25Dq^2 + \frac{9}{4}D\sigma^2 + \frac{25}{4}D\tau^2 - 5DqD\sigma + \frac{25}{3}DqD\tau - \frac{15}{2}D\sigma D\tau \tag{C.14}$$

Vita

Education

2009 – 2013 **Ph. D. Physics & Engineering Physics**
University of Saskatchewan

2004 – 2009 **B. E. Engineering Physics**
University of Saskatchewan
Great Distinction

2004 – 2009 **B. Sc. Computer Science**
University of Saskatchewan
Great Distinction

Publications

Published

1. T. D. Boyko, **R. J. Green**, R. Dronskowski, and A. Moewes. Electronic band gap reduction in manganese carbodiimide: MnNCN. *J. Phys. Chem. C*, **117**(24):12754-12761, 2013.

2. S. C. Das, **R. J. Green**, J. Podder, T. Z. Regier, G. S. Chang, and A. Moewes. Band gap tuning in ZnO through Ni doping via spray pyrolysis. *J. Phys. Chem. C*, **117**(24):12745–12753, 2013.

3. **R. J. Green**, D. A. Zatsepin, A. Hunt, E. Z. Kurmaev, N. V. Gavrilov, and A. Moewes. The formation of Ti–O tetrahedra and band gap reduction in SiO_2 via pulsed ion implantation. *J. Appl. Phys.*, **113**(10):103704, 2013.

4. **R. J. Green**, D. W. Boukhvalov, E. Z. Kurmaev, L. D. Finkelstein, H. W. Ho, K. B. Ruan, L. Wang, and A. Moewes. Room temperature ferromagnetism via unpaired dopant electrons and $p-p$ coupling in carbon-doped In_2O_3: Experiment and theory, *Phys. Rev. B*, **86**, 115212, 2012.

5. **R. J. Green**, A. Hunt, D. A. Zatsepin, D. W. Boukhvalov, J. A. McLeod, E. Z. Kurmaev, N. A. Skorikov, N. V. Gavrilov, and A. Moewes. Interplay of ballistic and chemical effects in the formation of structural defects for Sn and Pb implanted silica, *J. Non-Cryst. Solids*, **358**, 3187-3192, 2012.

6. J. A. McLeod, **R. J. Green**, E. Z. Kurmaev, N. Kumada, A. A. Belik, and A. Moewes. Band gap engineering in TiO_2–based ternary oxides. *Phys. Rev. B*, **85**, 195201, 2012.

7. J. A. McLeod, A. Buling, **R. J. Green**, T. D. Boyko, N. A. Skorikov, E. Z. Kurmaev, M. Neumann, L. D. Finkelstein, N. Ni, A. Thaler, S. L. Bud'ko, P. C. Canfield, and A. Moewes. Effect of $3d$ doping on the electronic structure of $BaFe_2As_2$. *J. Phys.: Condens. Matter*, **24**, 215501, 2012.

8. D. A. Zatsepin, **R. J. Green**, A. Hunt, E. Z. Kurmaev, N. V. Gavrilov, and A. Moewes. Structural ordering in a silica glass matrix under Mn ion implantation. *J. Phys.: Condens. Matter*, **24**, 185402, 2012.

9. E. J. McDermott, E. Z. Kurmaev, T. D. Boyko, L. D. Finkelstein, **R. J. Green**, K. Maeda, K. Domen, and A. Moewes. Structural and band gap investigation of GaN:ZnO heterojunction solid solution photocatalyst probed by soft x-ray spectroscopy. *J. Phys. Chem. C*, **116** (14), 76947700, 2012.

10. J. A. McLeod, **R. J. Green**, N. A. Skorikov, L. D. Finkelstein, M. Abu-Samak, E. Z. Kurmaev, and A. Moewes. Valence structure of alkaline and post-transition metal oxides. *Proc. SPIE* **7940** 79400R, 2011.

11. **R. J. Green**, G. S. Chang, X. Y. Zhang, A. Dinia, E. Z. Kurmaev, and A. Moewes. Identifying local dopant structures and their impact on the magnetic properties of spintronic materials. *Phys. Rev. B*, **83**:115207, 2011.

12. A. Bouaine, **R. J. Green**, S. Colis, P. Bazylewski, G. S. Chang, A. Moewes, E. Z. Kurmaev, and A. Dinia. Appearance of ferromagnetism in Co-doped CeO_2 diluted magnetic semiconductors prepared by solid state reaction. *J. Phys. Chem. C*, **115**(5):1556-1560, 2011.

Submitted for Publication

1. J. A. McLeod, D. W. Boukhvalov, D. A. Zatsepin, **R. J. Green**, B. Leedahl, L. Cui, E. Z. Kurmaev, I. S. Zhidkov, L. D. Finkelstein, N. V. Gavrilov, S. O. Cholakh, A. Moewes. Local structure of Fe impurity atoms in ZnO: Bulk versus thin films. *Phys. Rev. B*, submitted, 2013.

Under Preparation

1. B. Leedahl, D. A. Zatsepin, D. W. Boukhvalov, **R. J. Green**, J. A. McLeod, S. S. Kim, E. Z. Kurmaev, I. S. Zhidkov, N. V. Gavrilov, S. O. Cholakh, A. Moewes. Structural defects induced by Fe-ion implantation in TiO_2 bulk and thin films probed by XPS, XAS, and RXES. To be submitted, 2013.

2. T. Z. Regier, **R. J. Green**, D. Peak, A. J. Achkar, J. S. Tse, A. Moewes, and D. G. Hawthorn. Excited state spin sensitivity through the comparison of fluorescence and absorption intensities at the Fe *L*-edge of ferric and ferrous solutions. To be submitted, 2013.

3. **R. J. Green**, T. Z. Regier, X. H. Xu, G. S. Chang, E. Z. Kurmaev, and A. Moewes. Room temperature ferromagnetism driven by adjacent Fe-vacancy interactions in dilute magnetic oxide $(In_{1-x}Fe_x)_2O_3$. To be submitted, 2013.

4. **R. J. Green**, D. M. Korotin, A. Hunt, E. Z. Kurmaev, E. B. Yakushina, R. Z. Valiev, S. O. Cholakh, and A. Moewes. Interaction of nanostructured titanium implants with hydrofluoric acid probed by x-ray spectroscopy. To be submitted, 2013.

5. **R. J. Green**, D. A. Zatsepin, D. J. St. Onge, E. Z. Kurmaev, N. V. Gavrilov, and A. Moewes. Electronic band gap reduction, covalent interactions of interstitials, and intense luminescence in Co and Mn ion-implanted SiO_2. To be submitted, 2013.

Invited Talks

1. **SLAC National Accelerator Laboratory, Stanford University, California**, 8^{th} International Conference on Inelastic X-ray Scattering. *2p3d RIXS studies of band gap engineering in transition metal compounds* (Aug. 2013).

2. **Utrecht University, Netherlands**, Workshop on Fundamental X-Ray Spectroscopies. *Impurity model interpretation of 2p3d Resonant Inelastic X-ray Scattering* (Feb. 2013).

3. **Canadian Light Source**, Annual Users' Meeting. *Analysis of transition-metal materials using Resonant Inelastic X-ray Scattering and short-range theoretical models* (May 2012).

4. **University of British Columbia**, Resonant X-ray Scattering Workshop. *Analysis of transition-metal materials using Resonant Inelastic X-ray Scattering and short-range theoretical models* (Jun. 2012).

5. **Advanced Light Source, Berkeley, California**, Annual Users' Meeting. *Configuration of dopant sites in spintronic materials* (invited talk for student poster competition winner, Oct. 2010).

Relevant Awards

1. **Postgraduate Scholarship (PGS D3)**, *NSERC*. Three year national Doctoral scholarship (2010 – 2013).

2. **Best Student Poster**, *College of Engineering Research Days at the University of Saskatchewan.* Award for second best graduate level poster (2012).

3. **Best Student Poster**, *Canadian Light Source Annual Users' Meeting.* Award for best poster in the Materials Science category (2011).

4. **Canada Graduate Scholarship (CGS M)**, *NSERC*. Top tier national Master's level scholarship (2009 – 2010).

5. **Best Student Poster**, *Advanced Light Source Annual Users' Meeting.* Award for best student poster at the conference (2010).

6. **Undergraduate Student Research Award**, *NSERC*. National scholarship for summer research with Prof. Moewes (2009).

7. **E. L. Harrington Prize**, *University of Saskatchewan.* Award for most distinguished Bachelor's graduate in Physics or Engineering Physics (2009).

8. **Undergraduate Student Research Award**, *NSERC*. National scholarship for summer research with Prof. Moewes (2007).